KAUNAS UNIVERSITY OF TECHNOLOGY

RŪTA SIDARAVIČIŪTĖ

NOVEL SURFACE MORPHOLOGY PHOTOCATALYSTS FOR THE DECOMPOSITION OF ORGANIC CONTAMINANTS

Doctoral Dissertation
Technological Sciences, Environmental Engineering (T 004)

2019, Kaunas

This doctoral dissertation was prepared at Kaunas University of Technology, Faculty of Chemical Technology, Department of Environmental Technology, during the period of 2014–2018. The studies were supported by the Research Council of Lithuania.

Scientific Supervisor:

Prof. Dr. Dainius MARTUZEVIČIUS (Kaunas University of Technology, Technological Sciences, Environmental Engineering, T 004).

Doctoral dissertation has been published in:
http://ktu.edu

Editor:

Birutė Jurkšaitė (Publishing Office "Technologija")

ISBN 978-609-02-1618-7

The bibliographic information about the publication is available in the National Bibliographic Data Bank (NBDB) of the Martynas Mažvydas National Library of Lithuania.

KAUNO TECHNOLOGIJOS UNIVERSITETAS

RŪTA SIDARAVIČIŪTĖ

NAUJOS PAVIRŠIAUS MORFOLOGIJOS FOTOKATALIZATORIAI SKIRTI ORGANINIŲ TERŠALŲ SKAIDYMUI

Daktaro disertacija
Technologijos mokslai, Aplinkos inžinerija (T 004)

2019, Kaunas

Disertacija rengta 2014-2018 metais Kauno technologijos universitete, Cheminės technologijos fakultete, Aplinkosaugos technologijos katedroje. Mokslinius tyrimus rėmė Lietuvos mokslo taryba.

Mokslinis vadovas:

Prof. dr. Dainius MARTUZEVIČIUS (Kauno technologijos universitetas, technologijos mokslai, aplinkos inžinerija, T 004).

Interneto svetainės, kurioje skelbiama disertacija, adresas:
http://ktu.edu

Redagavo:

Birutė Jurkšaitė (Leidykla „Technologija“)

ISBN 978-609-02-1618-7

Leidinio bibliografinė informacija pateikiama Lietuvos nacionalinės Martyno Mažvydo bibliotekos Nacionalinės bibliografijos duomenų banke (NBDB)

ACKNOWLEDGEMENTS

To Kaunas University of Technology, to Faculty of Chemical Technology, To Department of Environmental Engineering and to my supervisor.

I am grateful for the people I have met on the way.

Table of Contents

List of Tables

List of Figures

List of Appendices

List of Abbreviations

AFM – Atomic Force Microscopy

AOP – Advanced Oxidation Process

BTEX – Benzene, Toluene, Etilbenzene, Xylenes

CB – Conduction Band

CVD – Chemical Vapor Deposition

CNT – Carbon Nanotubes

EDS – Energy Dispersive Spectroscopy

$(e^{-}\text{–}h^{+})$ – Electron and Hole Pair, Charge Carriers

FTIR – Fourier Transform Infrared

G – Glass Support

HVAC System – Heating, Ventilation and Air Conditioning System

IR – Infrared Light

MB – Methylene Blue

MOs – Metal Oxides

NF – Nanofibres

NHE – Normal Hydrogen Electrode Scale

OA – Axalic Acid

$OH^{\bullet}$ – Hydroxyl Radical

PA12 – Polyamide

PAN – Polyacrylonitrile

PCO – Photocatalytic Oxidation

PVD – Physical Vapor Deposition

PVP – Polyvinylpyrrolidone

PZC – Point of Zero Charge

RH – Relative Humidity

SC – Semiconductor

SEM – Scanning Electron Microscopy

SS – Stainless Steel

TEM – Transmission Electron Microscopy

TGA – Thermogravimetric Analysis

TiO_2, Titania – Titanium Dioxide

TiO_2-NF – Titanium Dioxide Nanofibres

TTCD – Tip o Collector Distance

UV – Ultraviolet Light

VB – Valence Band

VOC – Volatile Organic Compounds

XRD – X-ray Diffraction

Introduction

Today’s industrialized society must deal with very serious environmental issues every day. Environmental contaminants are continuously discharged from residential and industrial sources and not much is known regarding their fate in the environment. Traditional organic pollutants treatment methods, such as adsorption, proved to be insufficient. Moreover, they tend to create concentrated phases of pollutants. The development of technological systems for the removal of organic pollutants is one of the main focuses of environmental engineering science. Advanced oxidation processes (AOPs) are being widely researched for the ability to destroy variety of pollutants present in various environmental media. Among them, photo-Fenton and TiO_2 photocatalysis are the two most popular photochemical AOPs. and the latter is recognized as a promising and relatively clean process for destruction of various organic pollutants that harm water resources as well as both ambient and indoor air (1). The term of photocatalysis has been introduced at the beginning of the 20th century, but the interest in the application of this process in the cleantech sector continues to grow. However, there are several reasons that prevent the large-scale implementation of photocatalysis for the treatment of environmental media. The foremost challenge lies in finding the improved photocatalytic materials with either a novel composition and/or morphology to obtain higher activity in the process of photocatalysis with the lower amount of the spent catalyst.

It is well known that photocatalytic activity occurs at the surface of photocatalysts. Thus, a greater specific surface area available for catalysis is an important factor for the efficiency of the photocatalysis. Hence, TiO_2 catalysts have been prepared in various nano forms, such as nanoparticles, nanotubes, and nanofibres most often as free forms, and as thin films as immobilized forms. The main drawback of having a catalyst in a free form is potential agglomeration in suspension, resulting in reduced activity as well as complicated separation for further use and recyclability. Therefore, immobilized photocatalysts are advantageous in any practical system. The new tendency of photocatalysts incorporation on the support materials to achieve recyclability and more sustainability is observed. It was found out that more research could be done in order to develop novel supporting agents that overcome inherent mass transfer limitations of immobilized catalysis (2). Even though TiO_2 has its drawbacks, it is still the most widely investigated and used semiconductor in photocatalytic research. TiO_2 is environmentally benign, abundantly available, highly stable and low-cost metal oxide with the ability to efficiently degrade a variety of organic compounds.

This work presents the formation of different structures of a TiO_2 photocatalyst, characterization of their structural and photocatalytic properties. Novel attempts to increase a photocatalytic surface area, namely fibre-on-fibre structure and interference lithography, are presented.

Aim of the doctoral thesis

To develop novel nano- and micro- scaled dimensional morphologies of supported heterogeneous photocatalysts and research their application for the decomposition of organic pollutants in environmental medium.

Objectives

To synthesize nano-scaled fibrous photocatalysts and apply them in the decomposition of simulated pollution in an aqueous medium.

To research several technological options of the surface mounting of nanofibrous photocatalysts for the application to the decomposition of pollutants in both aqueous and gaseous media.

To enhance the surface of a thin film-scaled supported photocatalyst and research its applications to the decomposition of simulated pollution in an aqueous medium.

Scientific novelty

Novel morphologies of a semiconductor surface mounted photocatalyst have been developed and they have not been reported before for environmental applications. These morphologies include short fibres, fibre-on-fibre combination, and patterned thin films. The efficacy of these novel morphologies has been tested against simulated pollutants in several environmental media, thus providing new knowledge on the decomposition kinetics of such photocatalytic reactions.

Structure of the dissertation

This doctoral thesis consists of the following chapters: introduction, literature review, materials and methods, results and discussion, general discussion and recommendations, conclusions, reference list, publication list, and appendices. The thesis comprises 96 pages, including 30 figures, 15 tables, and 7 appendices.

Publication of the research results

Two original research articles based on the research presented in this thesis have been published in international journals registered in the CA Web of Science database. One manuscript is submitted. Experimental results were presented at five international conferences.

Practical value of the work

The novel morphology of a composite micro- and nano- structured photocatalyst provides technologically and environmentally favorable opportunity to increase the efficiency of the use of catalyst material achieving similar or superior performance. The presented work is aimed at the demonstration of technological feasibility of the presented surface mounted catalysts. The presented research corresponds to the level 3 of Technology Readiness Level. Nevertheless, scaling up of the production of such catalysts still poses a major research challenge, the small-scale fabrication methods can be already applied in personalized, low-capacity treatment plants for air/water remediation. Such applications are being discussed with air cleaner manufacturers.

Author's contribution

The results presented and discussed in the third part of this doctoral thesis are originally collected and analyzed by the author.

Part 1 of the thesis can be divided in two sections that describe the synthesis of fibrous TiO_2 of different sets of materials (the first set and the second set; more details in **Subsection 2.1.2.**) and its immobilization on different supports. In the first set of experiments (synthesis and analysis of fibrous TiO_2 photocatalysts and their testing in an aqueous medium) the author planned and conducted all experiments of the synthesis and efficiency testing, performed data analysis and prepared the manuscript for publication of the results. In the second set of experiments (mounting of the catalyst and preparation of the hybrid photocatalyst) the author planned and conducted the experiments of the synthesis of a nano-scaled photocatalyst, performed mounting on different supports and efficiency testing, performed data analysis and prepared a manuscript for the results publication.

In Part 2 (analysis of enhancement of the surface area of a thin-film TO_2 and its effect to the photoefficiency of the photocatalyst) the author planned and conducted experiments of the efficiency testing, performed data analysis on the efficiency results and participated in the manuscript preparation for the results publication.

The published articles were prepared by the author under professional guidance of supervisor and co-authors at Kaunas University of Technology.

1. LITERATURE REVIEW

1.1. Introduction to Advanced Oxidation Processes and Heterogeneous Photocatalysis

1.1.1. Basic Principle

Advanced oxidation processes (AOPs) can be described as in-situ generation of highly reactive radical species, principally hydroxyl radicals ($OH^\bullet$). These radicals are powerful and non-selective chemical oxidants (Table 1) that are able to destroy a variety of organic compounds with reactions rate constants in the following order: 10^8–10^{11} M^{-1} s^{-1} (3, 4).

Table 1. Relative oxidation power of some oxidizing species (5)

Oxidizing species	***Relative oxidation power***
Chlorine (Cl)	1.00
Hypochlorous acid (HClO)	1.10
Permanganate (MnO_4^-)	1.24
Hydrogen peroxide (H_2O_2)	1.30
Ozone (O_3)	1.52
Atomic oxygen (O)	1.78
Hydroxyl radical ($OH^\bullet$)	2.05
Positively charged hole on titanium dioxide, TiO_2^+	2.35

Two types of initiating the decomposition of organic molecules during AOPs are possible: $OH^\bullet$ can detach a hydrogen atom from water, as with alkanes or alcohols (e.g. Eq. (1)), or it can attach itself to the contaminant molecule, as in the case of olefins or aromatic compounds (e.g. Eq. (2), (4)).

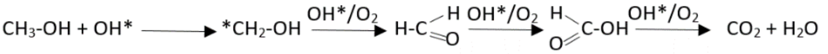

Eq.1

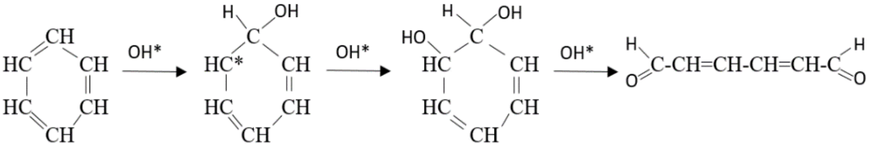

Eq.1

Reaction (2) continues as with hydrogen abstraction (Eq. (1)).

Although until now the best developed and main application of AOPs is water decontamination, these processes may have a wider application, e.g. odor elimination, air purification, soil remediation. AOPs can be conducted with or without the usage of ultraviolet (UV) radiation. Table 2 represents common AOPs and the main reactive species that were produced during them.

Table 2. Most common advanced oxidation processes and emerging reactive species (6)

AOP	***Comments***	***Reactive species***
Ozone (O_3) treatment	Can operate in dark with addition of chemicals, such as hydrogen peroxide (H_2O_2). Combination with light is also possible.	$OH^{\bullet}$, $HO_3^{\bullet}$, $HO_2^{\bullet}$, O_2^-, O_3^-
Ultrasonic treatment		$OH^{\bullet}$, $H^{\bullet}$
Fenton processes (H_2O_2/Fe^{2+})		$OH^{\bullet}$, $HO_2^{\bullet}$
Photolysis	Light driven processes.	$OH^{\bullet}$, H^+
Photocatalytic treatment		$OH^{\bullet}$, O_2^-, h^+, e^-, HO_2, $HOO^{\bullet}$

Among the existing AOPs, the heterogeneous photocatalytic treatment has proved to be of interest to the cleantech sector, where partial or total mineralization of organic pollutants in a liquid or gas phase is being addressed.

By definition, catalysis is understood as a chemical process which modifies a chemical reaction rate by adding a catalyst, i.e. a substance not consumed during the process and able to act repeatedly (7). Catalysis can be homogenous or heterogeneous. The latter refers to catalytic processes in which a catalyst and reactants are in different phases, namely solid-liquid, liquid-gas, and gas-solid. By the same token, heterogeneous photocatalysis is the acceleration of a chemical reaction that involves or requires light in the presence of a photocatalyst, usually a semiconductor (SC). Heterogeneous photocatalysis includes a large variety of reactions, such as organic synthesis, water splitting, photoreduction, hydrogen transfer, disinfection, water detoxification, gaseous pollutant removal, etc. (8) This type of catalysis is considered as a relatively clean process due to its advantages, such as low inputs of materials and energy as well as a minimum waste output (Table 3).

Despite many areas of application and a variety of reactions, the basic photophysical principle of photocatalysis is generally the same. Photocatalytic reactions are initiated when an electron (e^-) is getting promoted from the valence band (VB) to the conduction band (CB) leaving a hole in the VB (h_{vb}^+) (Eq. (3)). In this way, the so-called electron and hole pair (e^-–h^+) is being formed. irradiation of the SC photocatalyst with light should be at least the energy of the semiconductor band gap (discussed in more detail in **Subchapter 1.2.**). Subsequently, the resulting e^- and its resulting hole promptly migrate to the trap sites within the particle of the semiconductor (Eq. (4), (5)). However, these generated charges can also recombine releasing heat on the timescale of nanoseconds (Eq. (6)). The e^-–h^+ pair recombination is the major reason in the case of low quantum yields that is being reported for the photocatalytic degradation.

$SC + h\nu\ (\geq E_g) \rightarrow e_{cb}^- + h_{vb}^+$ photoexcitation **Eq.2**

$e_{cb}^- \rightarrow e^-_{trap}$ charge carrier trapping (reduction) **Eq.3**

$h_{vb}^+ \rightarrow h^+_{trap}$ charge carrier trapping (oxidation) **Eq.4**

$e_{cb}^{-} + h_{vb}^{+} \rightarrow N+E$	recombination, where N is neutral center and E is energy in a form of light ($h\nu' \leq h\nu$) or heat	**Eq.5**
$e^{-}_{trap} + O_{2,ads} \rightarrow O_2^{\bullet -}{}_{ads}$	oxygen ionosorption	**Eq.6**
$h^{+}_{trap} + OH^{-}_{surf} \rightarrow OH^{\bullet}$		**Eq.7**
$h^{+}_{trap} + H_2O_{ads} \rightarrow OH^{\bullet} + H^{+}$		**Eq.8**
$(H_2O)\ OH^{-} + h^{+} \rightarrow (H^{+}) + OH^{\bullet}$	proposed mechanism of indirect oxidation	**Eq.9**

In most cases, the photocatalytic degradation reactions are carried out in the presence of water, air, the target contaminant, and the photocatalyst (9). The presence of water is important for photocatalytic processes because water molecules tend to dissociate on the surface of metallic oxides (10). This process is important for the $OH^{\bullet}$ origination (Eq. (9)), which is responsible for so-called indirect oxidation processes (Eq. 10). However, there are some aspects that must be considered. The surface charge of a SC is an important factor in aqueous solutions and it depends on the pH of the solution. Here an important parameter is the point of zero charge (PZC) which represents the pH value at which concentrations of negative and positive surface centers are the same. In the case of photocatalytic reactions with ionic species, PZC defines the pH interval at which the adsorption of target molecules is either promoted or hindered by electrostatic interactions (11). In the case of air environment, water molecules may compete for the adsorption sites on the surface of the SC, especially at low concentration levels of (discussed in more detail in the following **Subchapter 1.1.2.**). Among other oxidants, the oxygen molecule is the most common electron acceptor due to the fact that it is readily available, has a high electron affinity (-0.13 eV) and is easily adsorbed on the surface of the SC (10). The adsorbed molecules scavenge electrons to form superoxides (Eq. (8)). Consequently, the hole is available for further reactivity during the direct oxidation processes. Other oxidant species, such as ozone (O_3), hydrogen peroxide (H_2O_2), and peroxodisulphate ($S_2O_8^{2-}$) have seldom been used as electron acceptors, whereas the benefit for the efficiency rarely pays off higher cost of chemicals (12).

As for classical heterogeneous catalysis, the overall process can be decomposed into five independent steps (Figure 1) (13):

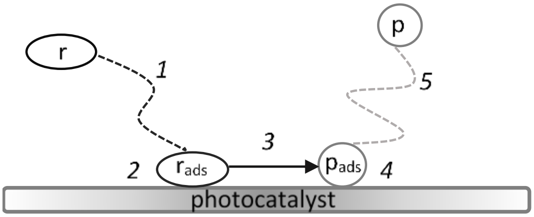

Figure 1. Schematic diagram of principal steps in heterogeneous catalysis

Step 1. Transfer of reactants (r) in the fluid phase to the surface;
Step 2. Adsorption of at least one of the reactants on the surface of the photocatalyst (r_{ads});
Step 3. Reaction in the adsorbed phase;
Step 4. Desorption of products from the surface of the photocatalyst (p_{ads});
Step 5. Removal of products (p) from the interface region.

Only the molecules that are in direct contact with the surface of the photocatalyst would participate in the photocatalytic degradation. The photocatalytic reaction occurs in the adsorbed phase (Step 3). The limiting step of the photocatalytic process depends on conditions. The reaction rate limiting step at low temperatures becomes desorption of the final product (Step 4). Meanwhile, the desorption of reactants is enhanced at higher temperature making Step 2 the reaction rate limiting step. Step 3 is limited by the mass transfer and availability of the active center for absorption of target molecules with regard to high concentrations of pollutants as well as their affinity to the surface of a photocatalyst. Since all participating compounds compete for adsorption on the surface of the photocatalyst, the higher the number of species in the reaction medium, the lower the sorbed phase of each target compound. During photocatalytic reactions, multiple intermediate products and target compounds will consume $OH^{\bullet}$ radicals and other reactive species, which then may turn into the rate limiting phenomenon of the degradation process under some conditions (13).

As already mentioned above, one of the main applications of heterogeneous photocatalysis is the mineralization of gas or liquid phase contaminants to non-harmful substances. Even though degradation begins with partial degradation, the term “photocatalytic degradation” usually refers to the complete photocatalytic oxidation to carbon dioxide (CO_2), water (H_2O), nitrate (NO_3^-), phosphate (PO_4^{3-}), and halide ions (9). PCO of organic compounds usually provide only a few mineralization products, but each of the primary products generate a number of compounds at intermediate stages. Usually, it is more known about pathways than about mechanisms. Any starting substance may have several reactive pathways. Only when the participating compound becomes oxidized considerably and the number of remaining carbons in each product becomes smaller, the number of possible intermediates decreases.

1.1.2. Influencing Parameters

➢ *Light intensity*. As mentioned above, photocatalysis requires light to sensitize the surface of a photocatalyst. Thus, light sources emitting UV-A (320–400 nm), UV-B (280–320 nm) and UV-C (100–280 nm) rays are widely used in photocatalytic experiments since the energy of these spectrum are equal or greater than the energy required to stimulate most of the photocatalysts (13). The ability of the photocatalyst to absorb light radiation greatly influences rates of photocatalytic reactions, although the nature or form of light does not affect the reaction pathway or, in other words, the photocatalyst sensitization mechanism does not matter in photocatalytic degradation (9). Generally, the higher light intensity and its absorption by the photocatalyst, the faster the reaction rate of the photoreactions, as proposed by Silva and Faria (14):

$$k = \alpha \cdot I^{\beta} \qquad \textbf{Eq.10}$$

where k is a reaction rate constant, α is a proportionality constant, β is a coefficient for low and high absorbed light intensities, and I is light intensity. It is clear that the reaction rate increases with the increased light intensity since more $OH^{\bullet}$ is being generated.

It was found out that the effect of light intensity to the photocatalytic reaction rate can be divided into two regimes, namely the first-order regime, where the e^{-}–h^{+} pairs are consumed faster by photoreactions than by their recombination process; and half-order regime, where the recombination rate of e^{-}–h^{+} pairs dominates. Obee (15) summarized the empirical correlation between the reaction rate and light intensity as follows:

$$r = KI^{n};\ n=1 \text{ if } I < \text{one-sun};\ n=0.5 \text{ if } I > \text{one-sun} \qquad \textbf{Eq.11}$$

where r is a reaction rate, K is a constant, I is UV irradiance, and one-sun is equivalent to about 1–2 mW/cm^2 for wavelengths below 350 and 400 nm, respectively.

- ➢ *Concentration and nature of pollutants*. Molecules of pollutants with higher affinity for the photocatalyst may adhere more effectively to its surface and this way could be exposed faster to direct PCO. It has been reported that the relationship between pollutant concentrations and photoreaction rate traditionally follows the Langmuir-Hinshelwood (L-H) kinetic model, when the reaction rate is proportional to the surface fraction covered by adsorbed species:

$$r = -\frac{dC}{dt} = \frac{k \cdot K \cdot C}{1 + K \cdot C} \qquad \textbf{Eq.12}$$

where r is reaction rate, k is a reaction rate constant, K is the reactant adsorption equilibrium constant, C is concentration of reagent (including reactive species). For low concentrations ($K \cdot C \ll 1$), the reaction follows the first-order behavior, whereas for high concentrations ($K \cdot C \gg 1$), the reaction follows zero-order behavior (16). This model applies to many pollutants, such as dyes (17–20), volatile organic compounds (acetone, formaldehyde, toluene, trichloroethylene, acetaldehyde, benzene (21–24).

Photocatalytic oxidation (PCO) is more appropriate for the destruction of organic contaminants in low concentration because the constant number of active sites on the surface of the photocatalyst has limited adsorption capacity. In fact, when the contaminant is highly concentrated, the surface of the photocatalyst becomes saturated and quantum yield diminishes due to the shielding effect of the contaminant on the catalyst surface (9). There is usually an optimal pollutants concentration when maximum PCO efficiency may be reached, while other conditions and parameters are stable.

- *Water content*. Molecular water is important for AOPs as the adsorbed water on the surface of the photocatalyst will react with the electron hole and initiate the generation of some hydroxyl groups, such as $OH^{\bullet}$ (Eq. (9)), which are able to destabilize and decompose pollutants molecules due to their high reactivity and non-selectivity.

In the case of the air medium, the presence of water vapor may be both beneficial and disturbing. As the absence of water vapor can seriously reduce the degradation of some gaseous compounds (21, 25), the excess of water vapor will inhibit the photocatalytic reaction rate once again because of the competition with pollutants for active sites on the surface of the photocatalyst. This is called a "competitive adsorption". Both positive and negative effects depend on the relative concentrations of water vapor and organic pollutants as well as relative binding of water vapor versus pollutants to the surface and the mechanism, by which the latter are photochemically activated (e.g. $OH^{\bullet}$ versus direct e^{-}–h^{+} oxidation). Organic molecules with weak interaction with the surface of the photocatalyst and preferentially oxidized by e^{-}–h^{+} oxidation should show a decrease of the photooxidation rate with increasing relative humidity (RH) in air. In contrast, strongly adsorbed molecules activated by $OH^{\bullet}$ are eliminated more efficiently at higher RH levels (26).

Some studies have reported a drastic decrease in gaseous organic pollutants decomposition efficiencies at high RH levels (more than 60%) (27–30). The presence of water vapor may also affect the generation of intermediates (25, 31). Overall, the influence of water vapor in the gas phase depends on the nature of pollutants as well as on concentrations of both organic pollutants and water molecules.

It is worth to emphasize that photoreactions in aqueous environment are already dominated by water as a solvent. The aqueous condition can, to some extent, be used as a benchmark for understanding the effects of high RH (26).

- *Residence time* is a time period spent by a molecule in a system. Higher residence time means longer staying time that increases the probability of a contact between the target pollutant and the surface of the photocatalyst. Photocatalytic efficiency can be extremely limited by a short residence time since the lower value of residence time provides a short time period of adsorption and photoreaction as well. The short space interval as a result of a high linear velocity reduces the chance that photogenerated reactive species will fully decompose the organic contaminants to non-toxic compounds (32).

In the case of the air medium, the residence time can be controlled by air flow rates. It has been reported that the effect of the air flow rate on the removal of gaseous pollutants falls under three regimes. Firstly, at low airflow rates (0–0.6 L/min), the increasing airflow rate enhances the decomposition process, indicating that the mass transfer to the catalyst surface (Step 2) is the dominating step. Secondly, at intermediate air flow rates (up to 1 L/min), the flow rate variation has no considerable effect on the decomposition process, demonstrating that surface reaction kinetics

(Step 3) is the dominating step. Finally, at high airflow rates, the exposure time to the PCO is so short that pollutants cannot fully participate in the PCO reaction resulting in decreased elimination rates (13). Hodgson et al. (33) have concluded that the relationship between the reaction efficiency and the residence time is approximated reasonably well by an exponential function. The results of other researchers have confirmed these findings (27, 29, 34) including this research, which results will be discussed later on.

➢ *Temperature*. Generally, photocatalytic systems do not require heat input (Eq. (3)). Most photoreactions are not sensitive to small variations in temperature. However, temperature still can have an impact on the photoreaction rate by influencing adsorption (Step 2), reaction (Step 3), and desorption (Step 4) steps as briefly mentioned in the previous **Subchapter 1.1.1**. According to the Arrhenius equation, the reaction rate constant (k) depends on the temperature (T) and activation energy (E_a) as follows:

$$k \propto f\left(\exp\left(-\frac{E_a}{R\cdot T}\right)\right)\ k = A \cdot e^{\frac{-E_a}{R\cdot T}} \qquad \textbf{Eq.13}$$

where, R is the universal gas constant, A is a constant for each chemical reaction.

Adsorption is an exothermic process, thus the attachment of pollutants to the catalyst surface (Step 2) is hindered at a higher temperature. Moreover, the recombination of e^-–h^+ pairs is also intensified at higher temperatures. On the contrary, a decrease in the temperature promotes adsorption of the target compounds. Furthermore, since desorption is an endothermic process, a higher temperature makes the removal of reaction products easier, this way providing more available active sites for further photoreactions. Thus, one of the three steps is rather dominant and it will strongly affect the overall photoreaction rate. Once again, the increased temperature will enhance the reaction rate when either photoreaction (Step 3) or desorption (Step 4) is a rate limiting step, while the decreased temperature enhances the reaction rate when adsorption (Step 2) is a rate limiting step. This may be the reason why some researchers came to different conclusions when they carried out experiments with different contaminants (13, 31). Nevertheless, it has been found out that the optimum temperature for PCO is between 20 and 80°C (12, 16).

➢ *Catalyst loading*. The efficiency of photocatalytic degradation is also influenced by the amount of a photocatalyst. Heterogeneous photocatalysis is known to show a proportional increase in degradation of organic pollutants with catalyst loading. Generally, with the quantity of the catalyst, the number of active sites on the surface of SC increases, which leads to the production of reactive radicals and promotion of photoreactions. Nevertheless, as the loading of the catalyst is beyond an optimum amount, the degradation rate is negatively affected because there will be the decrease in the penetration depth of the light into the fluid and consequently diminishing of light scattering occurs (9, 12, 16). For example, Giolli et al. (35) have found out that the increase in thickness of photocatalytic films above about 700 nm does not lead to improvement of the photocatalytic action.

1.1.3. Advantages and Disadvantages of Photocatalysis

The term of photocatalysis has been introduced at the beginning of the 20th century. Besides some drawbacks of the process, the interest of the application of this process in the cleantech sector continues to grow. Some major reasons are listed in Table 3.

Table 3. Major advantages and limitations of heterogeneous photocatalysis (36, 37)

Major advantages	**Limitations**
No energy input, effective under ambient temperature and pressure, reaction conditions are mild, reaction time is modest, and reduced chemical input is required.	Only 5% of the natural light activates most of existing semiconductor photocatalysts.
Nonselective. Process can be used in the destruction of a variety of hazardous compounds.	Fast charge carrier recombination.
System applicable at low concentrations of pollutants.	Demanding charge separation
Leads to the formation of harmless products, instead of transferring pollutants from one phase to another.	Interfacial charge transfer
It can be applied to hydrogen generation, gaseous and aqueous and solid (to some extent) phase treatments.	
Possible combination with other decontamination methods.	
Offers a good replacement for the energy-intensive conventional treatment methods with the capacity for using renewable and pollution-free solar energy.	

1.2. Semiconductors and Titanium Dioxide

Semiconductors are a class of crystalline structured materials with a conductivity value that lies between the conductors, such as metals and insulators, such as ceramics. Each atom in the crystal is surrounded by the nearest neighbors and shares its electrons from the outer orbital. Each shared electron pair constitutes a covalent bond. The interaction between the atoms in the crystal causes discrete energy levels to expand to energy bands with a large number of atoms. Within normal conditions, electrons in the crystal will fill up energy bands in order to minimize the energy of the system. The highest filled band is the VB and the next one is the CB. The latter is separated from the VB by an energy gap, a so called bandgap. A bandgap is an energetic region that describes energies that electrons cannot acquire. When the condition changes, for example, thermal impact, photoirradiation, etc., changes, the crystal becomes conductive and depends on the main charge carriers (e^- or h^+); it can be assigned to *n*- or *p*- type semiconductor. Consequently, in *n*-type semiconductors, the increment of electrons density makes them the majority of carriers, while holes are the minority ones, as the opposite happens in *p*-type semiconductors (10).

As the first law of photochemistry (or Grotthuss-Draper law) states, only the light absorbed by a substance can produce a photochemical change (10, 38). The SC can be excited by photons with energy equal to or greater than its corresponding bandgap energy, which leads to the generation of photoinduced e^{-}–h^{+} pairs. These charge carriers can migrate to the surface of SC and initiate series of chemical reactions with the adsorbed species resulting in the degradation of molecules of target pollutants (39). Illumination with less energy than the bandgap is inefficient because it does not increase the density of charge carriers and a part of the energy is lost as heat (10).

Once charge carriers are at the surface of SC, they must be trapped by donor and acceptor molecules, such as organic molecules and water or O_2, respectively, to avoid recombination (Eq. (6)). These events are the core of the photocatalytic process, as they trigger the formation and/or the breaking of molecular bonds required for chemical transformations as described above (Eq. (1), (2)). The surface reduction and oxidation reactions can be driven by photogenerated charge carriers only when their reduction and oxidation potentials lie between the VB and the CB potentials. Thus, thermodynamic driving forces in the photocatalytic processes depend on the relative relationships between the CB/VB potentials of the used photocatalysts and the redox potentials of reversible target reactions. More negative CB positions of SC are beneficial for reduction reactions, while more positive VB positions of SC are favorable for oxidation reactions (10, 39). However, it is important to mention that SCs with a narrower bandgap are susceptible to weaker chemical bonding leaving it sensitive to photocorrosion, while those SCs with a wider bandgap require photons with higher energy to excite charge carrier pairs. Potentials of typical reactions are given in Figure 2.

Various semiconductors oxides, including ZnO, SnO_2, TiO_2, WO_3 etc., may be used as photocatalysts due to their ability to absorb light hereby producing e^{-}–h^{+} pairs that enable chemical transformations of target compounds. These SCs have sufficient positive VB potentials to produce $OH^{\bullet}$ radicals and enhance O_2 reduction reactions (Figure 2). In contrast, photocatalysts with more negative CB positions (such as CdS, Si, Cu_2O, CuO) could produce photogenerated e^{-} with strong reduction ability for efficient enhancement of H_2 evolution and CO_2 reduction. Some of the mentioned SCs (e.g. CdS, ZnO, TiO_2) have suitable VB and CB positions for H_2 and O_2 evolution, which is favorable for water splitting (40).

The typical feature of a catalyst is its capability to regenerate its chemical composition after each cycle of interactions. As can be seen in Figure 2, TiO_2, being an *n*-type semiconductor, should ensure the formation of all the most important species for the photocatalytic oxidative degradation, namely h^{+}, O_2^{-}, and $OH^{\bullet}$ at neutral pH. Broadly speaking, TiO_2 starts absorbing light at wavelengths of about 400 nm and shorter, although the precise onset depends on the phase and degree of crystallinity of the TiO_2 material. This is one of the reason why TiO_2 is one of the most popular photocatalysts in environmental purification technologies. Moreover,

TiO_2 is chemically stabile, relatively inexpensive, and available as well as has stability against photocorrosion (16, 41, 42). Heterogeneous TiO_2-based photocatalysis has been demonstrated as a promising advanced oxidation technique for the treatment of air and water pollution due to the features named in Table 3.

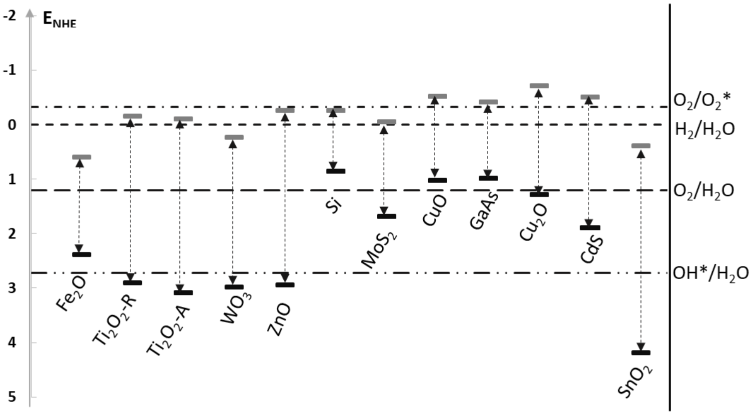

Figure 2. Band-edge positions of some typical photocatalysts (at pH=7 in aqueous solutions) in absolute and NHE scale

1.2.1. Characteristics of Titanium Dioxide

TiO_2 exhibits three crystal forms, i.e. anatase, rutile, and brookite. All TiO_2 polymorphs can be described as an arrangement of slightly deformed TiO_6 octahedral connected by vertices or edges, while oxygen shows a threefold coordination. Rutile is the most stable form, since it has the least dangling bonds, whereas anatase and brookite phases are metastable and can be transformed to the rutile phase when heated under elevated temperatures (typically 300–500°C). Rutile becomes the predominant phase after high temperature (>600°C) treatments (43, 44). Among the three TiO_2 crystal phases, anatase is the most widely studied and usually shows higher photocatalytic activity compared to others. The bandgap energy of the anatase is 3.2 eV (Figure 2). Several reasons have been proposed to explain differences in the photoactivity between anatase and rutile, including variations in electronic (e.g. Fermi-level position, electron mobility) or surface (e.g. concentration of hydroxyl (OH-) group) structure as well as the fact that rutile generally presents a lower surface area than anatase due to the larger crystallite size imposed by thermodynamic constrains (10).

The size of crystallites is an important factor affecting photoactivity. The smaller the crystallite size of a catalyst is, the larger the surface area available for adsorption and photocatalytic reaction is. However, the spatial confinement of small nanoparticles can also increase the e^-–h^+ recombination rate. It is important to mention that some studies have revealed that photocatalytic activity depends on the type of crystal surfaces exposed. The origin of this behavior lies in small energetic differences between crystal faces that can be sufficient to facilitate the preferential separation of electrons and electron holes in different crystal surfaces (10, 45).

Water molecules tend to dissociate on the surface of metal semiconductors. This process yields hydroxyls groups that saturate the coordination sphere of Ti^{4+} centers and protons, which bind to the bridging oxygens. Hydration of the TiO_2 surface is thermodynamically favored and it occurs rapidly even with air moisture (10, 45). Adsorption of target molecules is determined by the density of hydroxyl groups because many organic substances are attached to the surface of TiO_2 by hydrogen bonding, which is relatively weak, and molecules preserve the molecular structure of the adsorbate (46). This fact is important because photocatalysis shows structure sensitivity with regard to adsorption, and the surface complexes significantly affect the reactivity (10). As mentioned in the previous **Subchapter 1.1.2.**, the presence of water can act both as a competitor for active surface sites and as the source of $OH^{\bullet}$. Due to high affinity for water of TiO_2 surfaces, these molecules play a very relevant role on photoactivity. The effect of humidity in an air medium has been discussed previously. In the case of aqueous environment, it is necessary to consider the amphoteric character of the Ti-OH species because the surface charge depends on the solution pH and its PZC value. This is due to the equilibrium between acidic bridging hydroxyls (Eq. (15)) and more basic finite hydroxyls (Eq. (16)):

$$\text{Ti-OH-Ti} + OH^- \leftrightarrow \text{Ti-O}^-\text{-Ti} + H_2O \qquad \textbf{Eq.14}$$

$$\text{Ti-OH} + H^+ \leftrightarrow \text{Ti-OH}_2^+ \qquad \textbf{Eq.15}$$

At low pH values, the surface of TiO_2 is positively charged, while at high pH values it turns negative. In the case of photocatalytic reactions with ionic species, this pH interval (and PZC value) is important because it determines aqueous conditions at which adsorption is either facilitated or hindered by electrostatic interactions (10). In general, more efficient generation of $OH^{\bullet}$ is achieved in a weak alkaline medium owing to the presence of the optimal concentration of hydroxyl ions (Eq. (8), (10)), which is beneficial for the photocatalytic degradation of organic compounds in aqueous solution (9, 47).

Even though the majority of studies on photocatalysis with TiO_2 have focused on crystalline phases of the material, recently more studies recognize that amorphous TiO_2 has some advantages compared with purely crystalline phases, such as a much higher specific surface area, better adsorption, simpler preparation methods, and ability to dope with more elements this way improving photocatalytic properties of TiO_2 (48–51). Moreover, some authors have suggested that the electronic structure of amorphous TiO_2 is similar to that of the crystalline electronic structure (48). Thus, amorphous TiO_2 may be proved as a cheaper and more abundant alternative to its crystalline forms.

1.2.2. Structural Dimensionalities of Titanium Dioxide

As the photocatalytic mechanism with driving species and limiting steps were already discussed, other important factors of efficient photocatalysts performance include characteristics of a semiconductor itself. The size and crystalline phase of a catalyst, its specific surface area with pore structure, and volume have a significant influence on the photocatalysis process. Therefore, this research is focused on developments and improvements of these factors. Another important feature of a catalyst in photocatalysis, namely structural dimensionality, is no less important for the photocatalytic performance as well as for other applications.

Technically *nano* is referred to physical quantities within the scale of a billionth of the reference unit. The academic community has agreed to the <100 nm criterion as the benchmark for the nanotechnology classification, while the commercial sector has accepted broader flexibility up to 500 nm (52). At the end, a nanostructure can be viewed as an object whereby at least one of its dimensions is within the nanoscale.

TiO_2 based photocatalysis can benefit from its morphological design in many ways. TiO_2 materials could be classified according to their dimensionality. A nanoparticle can be considered as a zero-dimensional nano-element, which is the simplest form of nanostructures. A nanotube, nanorod, and nanofibre are considered as one-dimensional nano-elements. Then, nanoplates or nanosheets are two-dimensional nano-elements. Finally, more complex, porous, interconnected architectures can be referred as three-dimensional nano-elements (36, 52).

The synthesis of TiO_2 structures, both nano- and micro- sizes with modified morphologies, recently has attracted notable attention for usage not only in photocatalysis, but also in many other applications. Those structures include spheres (34, 53), nanorods (17, 54–56), fibres (19, 57–63), tubes (64–66), sheets and thin films (18, 67–69), and interconnected architectures (70–72). Each of those structures have their own characteristics and related advantages in one or another application area, as briefly presented in Table 4.

Therefore, the particle size strongly influences the characteristics of photocatalysts. Nanostructured materials have properties that differ from those of the bulk, conferred by the crystallite size and high specific surface areas, considering that surface-to-volume ratio increases as the crystal size decreases. The primary particle size of a photocatalyst defines the size of crystals and determines the available surface area for adsorption and consequently for PCO. However, it has to be taken into account that aggregation of particles is difficult to avoid, and aggregation can influence the adsorption of molecules, light scattering and light absorptivity, charge carrier dynamics, etc., (73). Choosing TiO_2 materials with appropriate dimensionalities enables full advantage of their unique properties.

Table 4. Morphological classification, major features and application of photocatalyst materials based on their dimensionality (36, 74, 75)

Dim.*	***Forms***	***Features***	***Application***
0D	Nanoparticles, nanospeheres	High surface area, high surface-to-volume ratio	Photocatalysis (76, 77), dye-sensitized solar cells (DSSCs) (78, 79), storage technology (80–82)
1D	Nanotubes, nanowires, nanofibres	Light scattering, higher surface-to-volume ratio, nonwoven mats	Photocatalysis (54, 55, 59–63, 65), gas sensing (83, 84), DSSCs (58, 85), batteries (86)
2D	Nanosheets, thin films	High adhesion, high smoothness	photocatalytic properties (17, 18, 67, 87–89), self-cleaning coatings (90–92)
3D	Porous, interconnected architecture	Porosity, high carrier mobility	purification and separation (70), and storage (71), biomaterials (72)

* *Dimensionality*

Commercially available TiO_2 nanospheres and powder have been well documented and established as a benchmark for TiO_2 based catalysts (26, 36, 93). Even though these spheres have a relatively high specific surface area, the separation of these nanoparticles from the solution can be very difficult. Moreover, the tendency of particles to agglomerate into larger particles reduces the photocatalytic activity during the cycled use (94–97). In fact, the powder involved in photocatalytic applications has been found to be expensive. Therefore, research attempts directed towards the development of other low-dimensional nanostructured materials, such as fibres, due to the higher surface-to-volume ratio, enabling a reduction in the e^-–h^+ pairs recombination rate and a high interfacial charge carrier transfer rate, with both of these effects being favorable for photocatalytic reactions (36, 42). As a consequence, improved catalytic properties of nanofibres compared to commercial TiO_2 nanopowder have been reported (62, 98, 99). The improved photoactivity was associated with a high specific surface area of 1D structure of TiO_2 nanofibres.

The large surface-to-volume ratio in nanoforms leads to a number of atoms with unsaturated arrangements and surface defects which may act as recombination centers (100). As the shape also influences the properties of photocatalysts, the bandgap of SC may be tuned by confining the exciton through modification, not only of the size, but also of the dimensionality of the nanocrystal. While spherical particles are thermodynamically the most stable, they have the smallest number of total surface atoms, one-dimensional nanostructures have a large fraction of atoms on their surface making them useful for photocatalytic applications (101).

TiO_2 particles are often immobilized on a solid support in order to prevent the transfer of the catalyst material to the treated medium. The main drawback of having a catalyst in a free form is potentially agglomeration in a suspension form resulting in reduced activity as well as complicated separation for further recyclability. Therefore, immobilized photocatalysts are advantageous to any practical system. 2D thin films exhibit high stability, no photocorrosion under bandgap illumination, moreover, superior surface properties. As a result, many studies have examined immobilized TiO_2 nanocatalysts as thin films and membranes, because they improve cost-effectiveness due to reduced material loss during the environmental medium treatment (102).

1.3. Fabrication Techniques of Photocatalysts

1.3.1. Structural Dimensionality 1D – Nanofibres

Several techniques have been reported for fabrication of 1D nanomaterials with well-controlled morphology and structures, such as drawing from a solution, self-assembly, phase separation template synthesis, electrospinning. Table 5 presents brief descriptions of those methods.

Among all described methods of fibres production, the fabrication by electrospinning stands out as a simple and effective method that allows the fabrication of continuous fibres with diameters down to a few nanometers (103, 104). Primarily, electrospinning was mainly used to produce polymeric nanofibres, while Kim and coworkers (105) firstly fabricated inorganic silica nanofibres by using the electrospinning technique in the beginning of this century. Thus far, many different 1D nanostructures have been prepared by the electrospinning technique, such as nanobelts, solid nanofibres, core-sheath fibres, nanotubes, hierarchical fibres, porous nanofibers, and etc. Consequently, inorganic nanofibres of semiconductors, such as ZnO, WO_3, SnO_2, CeO_2, TiO_2, Fe_2O_3, etc., have been successfully applied in the field of photocatalysis. Nevertheless, polymeric nanofibres have also been used for the photocatalysis with semiconductors as supports (106).

A typical electrospinning setup consists of three major components, namely a high voltage power supply, a spinneret (commonly a syringe with a needle), and a grounded collector (Figure 3).

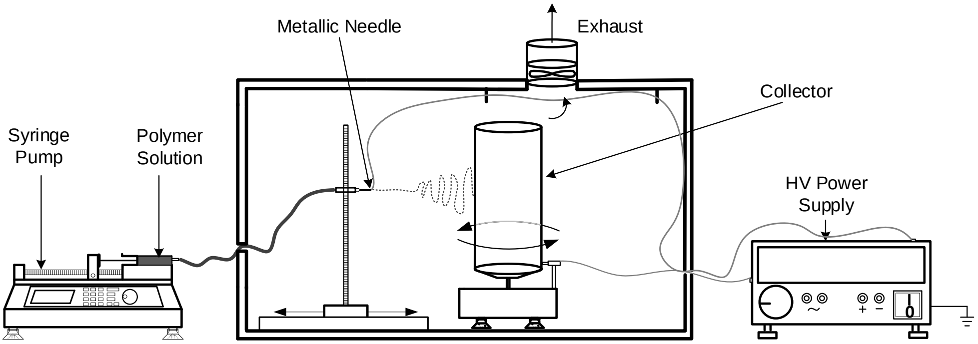

Figure 3. Schematic presentation of custom-made solvent electrospinning setup. The setup was made at the Department of Environmental Engineering (KTU) as a part of PhD thesis of J. Matulevicius (107)

Table 5. Description of various techniques for nanofibres production and references of employment (52, 108)

Technique	***Description***	***Advantages/ Disadvantages***	***References***
Drawing	This method makes long nanofibres one at a time. The pulling process is accompanied by solidification. Fibre diameter varies 2–100 nm; length varies from µm to mms.	Minimum equipment required/A discontinuous process.	(109, 110)
Template synthesis	The template is used to obtain a desired structure. It gives rise to nanofibres whose diameters and length are determined by the template pores.	Different diameters are easily achieved by different templates/The template removal may lead to structure defects.	(63, 70)
Phase separation	The main mechanism is the separation of phases due to physical incompatibility. The solvent is extracted, leaving behind the remaining phase. Fibre diameter varies 50–500 nm; length depends on a porous structure.	Minimum equipment required; mechanical properties of the matrix can be tailored by adjusting polymer concentration/Limited to specific polymers.	(71, 72)
Self-assembly	Nanofibres are formed by using smaller molecules as building blocks. The main mechanism is intermolecular forces between smaller units, the shape of these units will determine the final shape of the macromolecular nanofibre. Fibre diameter varies 10–100 nm; length varies 1–20 µm.	Good for obtaining smaller nanofibres; building blocks can be naturally occurring or designed for the intended application/A complex and challenging process; limited to a few polymers; can only create short fibres.	(111, 112)
Electro-spinning	Uses electric field to create nanofibres from charged droplet of polymer solution/melt. The process starts when the voltage overcomes the surface tension of the polymer to form a jet from the needle. Fibre diameter varies 3–1000 nm; length varies from several cm to several m.	Cost effective; efficient; easy to industrialize; the ability to control many factors of the process; long, continuous nanofibres can be produced/Jet instability; use of organic solvents.	(19, 42–44, 57–62, 84–86, 95–99)
Hydro-thermal synthesis	Process relies on the forced hydrolysis of the reactants (metal hydroxide as a mineralizer and metal alkoxides or salts as the source of metal ions), at moderate temperatures (<300°C) and high pressures in a sealed container.	Relatively mild operating conditions; one-step synthesis procedure; good dispersion in solution/Expensive equipment; inability to observe the process.	(54–56, 66)

The syringe is filled with polymer solution or melt, and high voltage (typically 10–50 kV) is applied between the needle tip and the collector. The solution is fed through the syringe needle at a controllable rate with the use of a syringe pump. The extrusion force is generated by the interaction between the charged polymer fluid and generated electric field. When the voltage is applied, the solution becomes highly charged, and the polymer droplet at the tip of the needle will experience the forces of electrostatic repulsion and surface tension. Under these electrostatic interactions, a conical fluid structure, the so called Taylor Cone, is being formed at the tip of the needle. At critical voltage, the repulsive force overcomes the surface tension of the polymer droplet and a charged jet erupts from the tip of the Taylor Cone and moves toward the collector. On the way to the collector, the solvent evaporates (or the melt solidifies) and solid fibres are deposited as a randomly oriented nonwoven mat (52, 113).

The electrospinning technique is a simple, versatile, and environmentally friendly approach to fabricate various synthetic and natural polymers as well as metallic and ceramics. Furthermore, electrospun inorganic semiconductor nanofibres show a great advantage as photocatalysts because of a large surface area and high aspect ratio (length to width) can provide the maximum available region for the catalysis process. The acclaim of the electrospinning technique confirms the fact that over 500 universities and research institutes worldwide are studying various aspects of the electrospinning process and electrospun nanofibres. Moreover, the number of patents for applications based on electrospinning has grown in recent years. Some companies, such as eSpin Technologies (USA), Bioinicia (Spain), Technical Fine Co., Ltd (Japan), IME Technologies (The Netherlands) and others are actively engaged in the benefits of electrospinning, while companies, such as Donaldson Company (USA) and Freudenberg (Germany) have been using this process for the last two decades in their air filtration products (106, 114).

➢ *Main parameters of electrospinning.* Although the electrospinning setup is not complicated, the physics process is complex and includes the understanding of the fluid rheology and electrostatic. Therefore, only the main parameters of the electrospinning process and the influence to the morphology of fibres are discussed here. More information on deeper understanding of electrospinning can be found elsewhere (52, 115). The parameters for controlling the electrospinning process can be classified in three parts: solution parameters, process parameters, and ambient parameters. All of them are summarized in Table 6.

Table 6. The main parameters of electrospinning process for controlling the morphology of fibres (52, 106)

Electrospinning parameters		***Effect of process and outcome***
Parameters of solution	Polymer chemical parameters	The fibre diameter increases with higher concentration of the polymer solution, while low concentrations lead to beads formation. Solutions of a polymer with high M_w provide the desired viscosity for the process.
	Polymer physical parameter	Too high viscosity prevents the jet formation, while too low viscosity hinders the continuous electrospinning process. High surface tension of a solution induces instability of jets and spray process instead of spinning, resulting in formation of beads. Lower surface tension helps electrospinning to occur at lower electric field. Higher electrical conductivity of the polymer solution results in a reduced diameter of fibres, while low conductivity results in insufficient elongation of a jet.
Processing parameters	Voltage	Higher voltage causes greater stretching of the solution due to stronger columbic forces in the jet. This leads to a smaller fibre diameter and rapid solvent evaporation
	TTCD	The TTCD influences the flight time and electric field strength. Minimum distance is required to give fibres enough time to dry before reaching the collector. The effect on fibre morphology is not as significant as other parameters.
	Feed rate	In order to keep the Taylor's Cone stable, the corresponding feed rate for given voltage should be used. A higher feed rate results in an increase in the fibre diameter. A lower feed rate is more desirable as the solvent will get enough time for evaporation.
Ambient parameters	Temperature and RH	At high RH levels, there is a possibility for water condensation on the surface of the fibre. As a result, this may have an influence on the fibre morphology especially a polymer dissolved in volatile solvents. At very low humidity, a volatile solvent may dry too rapidly, as a result, the needle tip is clogged. Higher temperature of the solution may increase its evaporation rate and reduce its viscosity, consequently, there is a yield of fibres with a decreased fibre diameter.

Each of these parameters affects the morphology of obtained electrospun fibres, and the desired morphology can be obtained while manipulating them.

The most attention is given to solution electrospinning so far. However, there are also arising investigations on electrospinning using polymer melts. Generally, most parameters discussed in Table 6 are also applicable to melt-electrospinning. However, there are still some differences between solution and melt-electrospinning. These include the need of constant heat for the container with the polymer so that it would remain in the molten state; also, TTCD in melt-electrospinning is much smaller than that in solution electrospinning. Moreover, depending on the melting temperature of a polymer, the melt usually is more viscous than solution, thus a greater voltage is required for the jet initiation (52).

1.3.2. Structural Dimensionality 2D – Thin films

The most common methods to synthesize semiconductors thin films can be divided into several groups, namely chemical methods, reactive evaporation, and reactive sputtering. Table 7 presents and briefly discusses the most common techniques for the production of thin films of semiconductors.

Chemical vapor deposition (CVD), physical vapor deposition (PVD), and sol-gel dip coating are the most common methods found in articles and can be used for photocatalyst production. The sol-gel dip coating technique is less expensive compared to CVD and PVD and its ability to tailor the microstructure of the deposited films is an advantage that latter do not have. Despite that, this technique has one common issue, i.e. purity of thin films. In this case, PVD is a more acceptable technique because deposition is carried out in high vacuum. Quality of thin films is much higher compared with sol-gel dip coating (116). Nevertheless, it is easy to control the process, dopant concentration, thickness, etc. One of the PVD methods, namely sputtering, has received a considerable importance for making TiO_2 thin films for various applications (Table 7). By understanding the physics of thin film growth or analyzing the Thornton zone model, it is not hard to control the microstructure as well. Furthermore, the reactive magnetron sputtering seems the most promising because of its versatility, capacity of homogenous surface coverage even at low temperatures and possibility to deposit coatings on the surface with an area of several square meters, and synthesized coatings exhibit high adhesion to a substrate and high resistance to external actions (2, 117).

What is more, composition manipulations of a photocatalyst, in other ways, such as an increase in the photoactive surface, can be applied to enhance the photocatalysis efficiency. Lithography is a commonly employed process in the micro fabrication of thin parts or even bulk supports made of any substance. Lithography is the process that uses light (possible with wavelength from UV to X-ray) to imprint a pattern into the photosensitive material or, in other words, a photoresist. These materials are used as a template for specific pattern transferring to a substrate of interest. A bit simpler type of this process is interference lithography, which is based on the interference of small numbers of coherent laser beams that produce periodic patterns. Interference lithography is emerging as one of the most powerful yet relatively inexpensive methodologies for creating large-area patterns with micron-to-sub-micron periodicities of thin parts or bulk supports (118).

Table 7. Description of various techniques for thin films production and references of employment (119)

Method	***Description***	***Advantages/Disadvantages***	***References***
Hydro-thermal synthesis	Synthesis involves either single or heterogeneous phase reactions in an aqueous medium at elevated temperatures and pressures to crystallize materials directly from solution.	Provides a simple mode of operation; has an ability to grow large high-quality crystals/expensive equipment; inability to observe the process.	(53, 120, 121)
CVD	Gas-phase volatile precursor molecules are exposed to react and/or decompose to form a desired material on the surface of a substrate.	High-purity, uniform, reproducible solid materials; flexible with regards to the shape of substrate; good adhesion/high cost of high purity compounds; high reaction temperature; presence of corrosive gases; low deposition rates.	(17, 30)
Liquid phase deposition	Immersion of a substrate in an aqueous solution containing precursor species (which eventually undergo hydrolysis) that precipitates preferentially on the substrate surface producing a conformal coating.	Simple method, can produce large surface areas and complex morphologies; does not require any special equipment/slow process; limited thickness of depositions; wastage of solutions after every deposition.	(122–124)
PVD (including sputtering)	Vaporization coating technique that transfers materials on an atomic level onto a solid substrate. It involves purely physical processes, i.e. high temperature vacuum evaporation followed by condensation rather than a chemical reaction among precursors.	Is suitable for any kind of inorganic material coating as well as some of organic; high quality, uniform films; good adhesion; possible to keep substrate at low temperature which allows low melting point materials to be used as substrates/possible grainy and porous films; risk of substrate damage.	(35, 67, 88, 89, 125)
Electro-phoretic deposition	Two-step process by which particles in a colloid solution are collected onto a substrate. First step: (electrophoresis) particles acquire electric charge and move towards one of the electrodes. Second step: (deposition) particles are collected on the other electrode and form a coherent deposit.	Relatively simple; homogenous, high quality thin films on large substrates; size and shape of nanoparticles can be well controlled; uniform coating thickness without porosity; thick films produced, low conductivity, good chemical stability/volatile, toxic solvents; flammability; expensive; high electric fields strengths are required.	(68, 69)
Sol-gel dip-coating	Technique comprises the transformation from a colloidal suspension containing the desired precursors into a solid network. The colloidal suspension of precursor is formed due to the involvement of hydrolysis and polymerization reactions.	Simple procedure and equipment; homogeneity, low cost, reproducibility, controllability; easy to anchor on a variety of substrates bearing complicated shapes and a large surface area/long period of deposition; high cost of reagents; thermal treatment is required; extreme volume shrinkage during gelation; residuals.	(18, 21, 46, 92)

1.3.3. Morphology Examination of Photocatalysts

Since the photocatalyst performance depends on its structural and morphological properties, the characterization is an important step in the preparation of the photocatalyst and optimization of the photocatalytic process. The importance of the properties of the heterogeneous photocatalyst can be acknowledged if one looks at it through the fundamental steps involved in the heterogeneous photocatalytic process (**Subchapter 1.1.**):

Step 1. Transfer of the reactants to the surface of the photocatalyst is influenced by its geometrics, surface area, pore size and shape, and thickness;

Step 2. Adsorption of the reactants depends on the nature of the active sites on the surface of the photocatalyst;

Step 3. Reactions in the adsorbed phase depend on the nature and number of complexes that were formed by the chemisorbed molecules;

Step 4. Desorption of the products depends on the amount of adsorbed species and the strength of their bonds to the surface of the photocatalyst;

Step 5. Removal of the products depends on the shape and size of the diffusing molecules, the pore and thickness of the photocatalyst and by the turbulence of the flow (126).

It is possible to analyze the features of the photocatalyst by means of various characterization techniques. The most important properties of environmental photocatalysts and characterization techniques are presented in Figure 4. More detailed descriptions are given in **Appendix A. 1.**

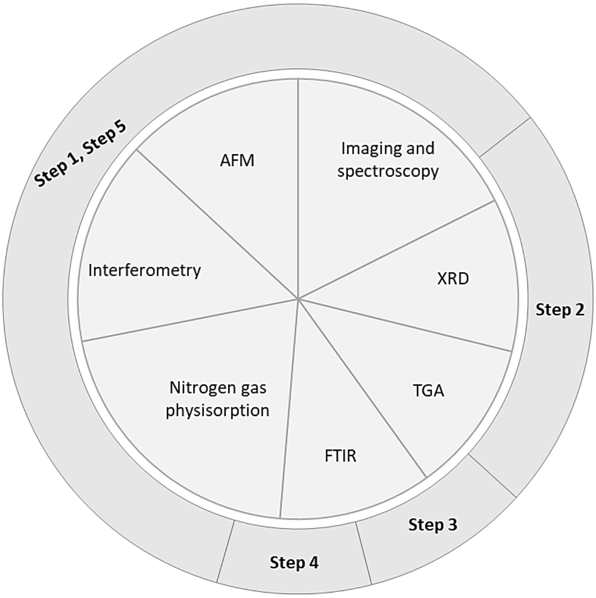

Figure 4. Presentation of morphology examination methods in relation with fundamental steps of heterogeneous photocatalysis

1.4. Heterogeneous Photocatalysis for Environmental Application

Technological advancements in processes and products have triggered new products together with new pollutants in an abundant level. Environmental pollution and energy security are one of the world's critical challenges which have received appropriate attention from governments across the world and resulted in the alteration of policies, strategies, and regulations. With respect to the recognized threats, the focus of global research has been redirected toward the development of technologies for clean energy and clean environment. Hence, these demands led for increased attention to new functional nanomaterials and related technologies. Among the existing nanostructures, 1D nanostructures are of particular interest (Figure 5) because of their chemical and physical properties that have already been discussed.

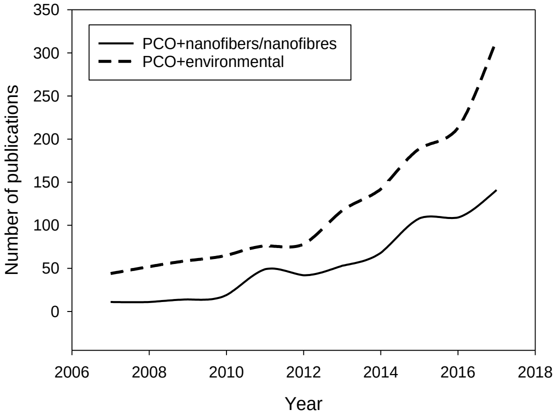

Figure 5. Number of articles published from 2007 to 2017 on the application of photocatalytic oxidation in environmental field and nanofibres usage in photocatalytic oxidation (source is from ISI web of science, used key words: photocatalytic oxidation, environmental, nanofibres, nanofibers)

In order to control the environmental pollution, monitoring is a very important step. Thus, nanofibres receive an important attention in the field of sensors development for detection of various analytes in the air and water medium. Attractiveness of nanofibres in sensing technologies relies on their small size, large surface area, high porosity and reactivity, controlled morphology, structure and in some cases electrocatalytic properties as well as flexibility of the surface functionalization. These features could further enhance sensitivity, stability, and response speed of the sensors. Open pore structures of nanofibrous membranes potentially allow analytes to diffuse to the surface of sensing materials and lead to a fast response accordingly (127, 128). Semiconducting materials, such as TiO_2, are known for their ability to detect trace concentrations in parts per million (ppm) levels and above (129). Nanofibres may be applied as sensing interfaces (130) and they also have demonstrated to be good substrates to support other sensing materials, such as nanoparticles of noble metals (131).

The environmental pollution control also involves treatment of the polluted environmental medium. Functional nanofibres could be used in the processes of filtration, adsorption, decomposition, etc. Nanofibrous materials have superior capabilities for applications in filtration because of their structural properties, such as high porosity, interconnected pore structures, and so forth. (106, 132). Moreover, nanofibre-based filter media are expected to have high filtration efficiency for fine particle and relatively low pressure drop due to the unique structure of nanofibrous mats (133). There were successful attempts to remove particulate molecules and small particles from both air (134, 135) and aqueous media (136, 137) while using electrospun TiO_2 nanofibres. What is more, polymeric nanofibres with addition of TiO_2 display good antimicrobial properties.

It was concluded that PCO is a promising technology for the destruction of environmental pollutants instead of accumulating them, and 1D nanomaterials have provided their intriguing application in this area. Semiconducting metal oxides, with TiO_2 being the most popular one, based on photocatalytic treatments have received attention due to their low-cost, recyclability, reusability, and environmental friendliness. The electrospinning technique combined with calcination process is a simple and versatile method to produce inorganic nanostructures with well-defined compositions and structures. The interest of utilizing TiO_2 nanofibres (TiO_2-NF) in PCO applications covers mostly research in aqueous and air media. The most common model pollutants include Methylene Blue, Methylene Orange, Rhodamine B for an aqueous medium, and BTEX for an air medium (Table 8).

The photocatalytic performance of TiO_2 nanofibres relies on the shape, size, crystallinity, and composition of the photocatalyst. The crystalline structure of the TiO_2-NF is significantly related to their photocatalytic properties. As mentioned above, the anatase crystalline phase is the most active in photocatalytic reactions. Researches have reported the decrease in PCO efficiency with the presence of rutile phase in synthesized TiO_2 photocatalysts (35, 67, 138). The production of metal oxides (MOs) nanofibres with electrospinning usually includes a polymer solution as a matrix for the precursors of MOs. Very often organic precursors of TiO_2, such as titanium isopropoxide or butoxide, are used. In order to eliminate organics and to initiate the formation of crystals, the heating step is included in the synthesis of nanofibres after the electrospinning. Temperatures required to form an anatase phase of TiO_2 (**Subchapter 1.2.1.**) are not high enough to remove all the carbon from the final product, so the content of carbon usually varies up to 10% (61). Besides, calcination at high temperature not only activates the rutile phase, but also strongly reduces the specific surface area, both of them are unfavorable for the photocatalysis.

Electrospun nanofibre-based TiO_2 photocatalysts take advantage of the optional design of the nanostructures. Consequently, many different 1D dimensional nanostructures have been synthesized, including long fibres, hollow fibres, thorny fibres, porous fibres, hierarchical fibres, etc. All these attempts intend to increase the surface area available for photoreaction and sorption abilities to prolong the contact time and achieve higher PCO efficiency. Researches have reported that morphologies with higher sorption capacity, such as porous or hollow structure, demonstrate better photocatalytic efficiencies (42, 61, 62, 139). Carbon materials, such as carbon nanotubes (CNT), carbon spheres, graphite oxide (GO) (19, 57, 66, 140, 141) have also been used for the modification of titania nanofibers not only to increase the surface area, but also to improve scorpion capacity for organic pollutants in order to achieve higher mineralization degree. Moreover, additivities are advantageous for improving the visible-light photocatalytic activity of TiO_2 nanomaterials. Coupling and doping TiO_2 with additivities, such as nitrogen (N) (142), iron ions (Fe^{3+}) (68), zirconium ions ($Zr^{2+/4+}$) (46, 60) promote the separation of photoexcited e^-–h^+ pairs by mutual transfer of carriers within the heterojunction, thus extending the light response range (125).

As titania could be obtained from organic precursors forming almost pure inorganic nanofibres, the nanostructures of TiO_2 could also be directly incorporated into electrospun polymeric nanofibres. Many kinds of polymers, such as polyacrylonitrile (PAN), polyvinyl alcohol (PVA), nylon, polyaniline (PANI), cellulose acetate (CA), polyvinylpyrrolidone (PVP) etc., have been used to support TiO_2 nanoparticles for photocatalysis (Table 8). TiO_2 nanoparticles are either incorporated during electrospinning (42, 143–146) or dispersed on the surface by hydrothermal methods (43, 147). Nevertheless, the most reported results show that agglomeration of TiO_2 nanoparticles leads to a lower specific surface area which may lead to the decrease in the TiO_2 activity (143, 146). Furthermore, electrospinning of solutions containing TiO_2 nanoparticles faces challenges, such as nozzle blockage during the electrospinning process and bead formation.

Electrospun photocatalysts have also shown excellent recyclability for a number of times as photocatalysts without any deterioration in the photocatalytic effect (43, 61, 97, 147).

As the surface area available for photoreaction is one of the most important factors for high PCO efficiency, many newly synthesized TiO_2 nanomaterials are being spread in the tested medium. Most research attempt to thoroughly disperse TiO_2 nanofibres or freely immerse fibrous mats into aqueous solutions of tested pollutants (Table 8). Even this method could be considered as advantageous for the high contact of pollutant molecules and the surface of the photocatalyst, the separation of the photocatalyst from the tested medium becomes a serious difficulty for reusability of the photocatalytic material. Any attempts to further apply such processes are related to supporting the catalyst fibres for their continuous use. Although there were attempts to synthesize magnetic TiO_2 nanofibres, it leads to facilitated separation of catalytic materials form the treated medium (148–150).

In order to prevent the transfer of the photocatalyst material to the treated medium, TiO_2 could be immobilized on a solid support. Various solid supports, such as silica and zeolites, quartz and glass fibres, stainless steel, alumina, non-woven fabric, etc., have been reported aiming to immobilize TiO_2 nanostructures on substrates (Table 8). Sol-gel and dip-coating techniques are used for this purpose. Nevertheless, some researchers have suggested more creative methods, for example, Choi and colleagues (97) used hot-pressing process to fix TiO_2 nanofibres on quartz plates. However, the reaction efficiency is strongly limited by mass transfer from the treated medium to the TiO_2 surface because reaction could occur only at the gas- or liquid-solid interface (151). Non-woven fabrics could be useful supports for fabrication of flexible, light weight, and cost-effective photocatalytic filters. The synthesis and design of organic-inorganic hybrid materials have been under recent investigation (42, 143, 144, 146, 147).

The removal of organic pollutants by PCO is a surface reaction process, consisting of five steps (**Subchapter 1.1.**). The transfer of the pollutant to the reaction surface is an important step for decomposition by the photocatalyst. Therefore, the mass transfer and kinetic reaction rates as well as the surface area for the reactions are the most important parameters for the design of a PCO reactor. The study of PCO reactors should focus on all three parameters and consider the combined optimal effect for the removal of organic compounds, including their reactions among each other in the PCO purification process. Generally, the structure of a PCO reactor consists of two main parts, i.e. the reaction structure and the UV source. Many PCO configurations for air and water treatment have been proposed in the scientific literature. It could be classified according to the radiation characteristics (solar or artificial, concentrated or not), to the distribution of the catalyst (suspended or immobilized), to the reactor geometry (tubular, annular, multi-annular, flat plate, parallel plate, U shaped, fountain, etc.), to the operation mode (batch or continuous), etc. (10).

Mo and co-authors (31) sorted PCO reactors according to the configuration of UV lamps with respect to the reaction area. Different configurations lead to different characteristics of the reaction area, mass transfer and photocatalytic reaction rates. The main configurations include plate, annular, fluidized bed, honeycomb, packed-bed, and mop fan reactors. Mo and Boyjoo (31, 152) have emphasized the main advantages drawback of most common types of photoreactors. It is possible to obtain large convective mass transfer and reaction rates with the plate type reactor. Moreover, the illumination zone is high to the surface per unit volume of the reactor. In the case of an aqueous medium, the thin film of liquid absorbs very little UV, therefore, photoactivation of TiO_2 is higher, but the reaction surface area is much smaller than of other type reactors. In the honeycomb type reactor, the UV source is parallel to the reaction surface area, which results in a low reaction rate even if the reaction surface area and mass transfer rate are large. For the annular type reactor, both the convective mass transfer rate and the reaction surface area are small, even when the UV source irradiates on the reaction area directly. Therefore, they concluded that the reactor should have a high specific surface for a large reaction surface area, support small pass-through channels and low air velocity for high mass transfer, and have the UV source irradiate directly on the reaction surface. Packed bed reactors are of a simple construction and can have high conversion per unit mass of a catalyst. However high radial radiation gradients can occur and the maintenance of the unit can be difficult. Fluidized bed reactors allow high throughput and low pressure drop but are difficult to control and tend to suffer from catalyst losses, which means that either catalyst replacement or additional equipment is needed.

Plate type or fluidized bed reactors were used the most for testing the TiO_2-NF photocatalyst in the aqueous medium, while annular type reactors were very common for experiments in the air medium (Table 8). Even though, it was concluded that these type reactors are not designed for high throughput, especially in the case of the air medium and are therefore not commercialisable. However, they are important in studies to determine kinetic parameters (152).

Table 8. Examples of applications of TiO_2 nanofibres and thin films for environmental photocatalysis

Form	***Pollutant***	***Support***[a]	***Reactor type***	***Morphology***	***Fabrication***[b]	***Ref.***	***Key findings***
1D	Naphthalene (25 ppm) Aqueous medium	F Free-standing mats	Petri dish, V=50 mL; UV source (power=12 W, I=2.05 mW/cm^2, and λ=254 nm); d=5 cm	FE-SEM, TEM, EDX, XRD, Raman and UV-vis spectroscopy	E-spinning matrix PVP prec. TTIP	(61)	Carbon residuals was 6 wt%; BET 29.39 m^2/g. PCO was assessed for three loadings of TiO_2-NF mats. The sorption of fibres was ~10%; UV-light efficiency ~20%. Degradation of pollutant increased with TiO_2-NF mass; times for different loadings were 43, 22, and 13 min. Good reusability.
1D	Para-nitrophenol (10^{-4} M) Aqueous medium	F Dispersed	Petri dish, V=50 mL; UV source: λ=365 nm, I=1.07 mW/cm^2)	FESEM, TEM, HRTEM, XRD, BET, EDX, TGA, UV-vis and Raman spectroscopy	E-spinning matrix PVP prec. TTIP	(59)	Quantum dot sensitized hollow TiO_2-NF. No carbon residuals; BET of solid and hollow TiO_2-NF were 17.42 and 34.89 m^2/g. Different amounts of catalyst were used. Experiment duration was 90 min. Sorption was 9–19%. Degradation of pollutant increased with increasing catalyst loading. Solid NF demonstrated efficiency of 81.2%; hollow NF of 90.1% and quantum dot sensitized hollow NF of 90.2%.
1D	Rhodamine B (10 mg/L) Aqueous medium	F Dispersed	Pyrex glass beaker, V=50 mL; light source: Xe lamp, power=500 W, λ<420 nm, d=15 cm	SEM, TEM, XRD, BET, XPS, UV-vis spectroscopy	E-spinning matrix PVP prec. TBT	(58)	Solid TiO_2-NF and thorny TiO_2-NF have been synthesized. BET of solid and thorny TiO_2-NF was 25.56 and 329.69 m^2/g. 0.05 g catalysts was added to solution. Experiment duration: 60 min. Solid TiO_2-NF had efficiency of 61.5% and thorny TiO_2-NF of 89.3%.
2D	Phenol (1×10^{-4} M)	S	Quartz spectrofluorometric cell (1 cm path length),	XPS, Secondary ion mass spectrometry	PVD	(35)	Sample size was 6×30 mm^2. Duration of experiments: 48 h. The coatings deposited on glass exhibited a relative change of conc. ~70%,

	Aqueous medium	Copper, stainless steel, glass	V=2.5 mL; light source: mercury lamp, power=125 W, λ=334 and 365 nm; I=3.8 mW/cm^2	(SIMS), Raman spectra, XRD			whereas those on SS showed a low photoactivity (relative change of conc. ~20%). The efficiencies were concluded to be mostly depended on the catalyst crystal phase.
2D	MB (5x10^{-5} M) Aqueous medium	S Soda lime glass	Open-top quartz cell, with the irradiation perpendicular to the surface; light source: xenon lamp, power=150 W, I=2 mW/cm^2	XRD, SEM, Rutherford backscattering spectroscopy (RBS), XPS	PVD	(125)	N-doped TiO_2 thin films. Absorbance was less than 2% after 6 h. It has been found that for a certain critical limit of 1.19 at% of N-doping in the titania anatase crystalline lattice enhanced the photocatalytic behavior. By doping the titania lattice with nitrogen, the photocatalytic activity was enhanced under both UV and visible light.
2D	MB (12 mg/L) Aqueous medium	S High purity silica	Photoreactor – n.a. V=40 mL; light source: mercury lamp (power=250 W, λ=365 nm).	XRD, SEM, TEM,	PVD	(67)	Annealing temperatures ranged 300–600°C. Experiment duration was 2 h. With increasing annealing temperature, the photocatalytic activity of thin films increased and reached the maximum value at 500°C with almost total decolorization.
2D	Methyl Orange (0.6 mmol) Aqueous medium	S Slide substrates	Quartz cell (h=20 mm, Ø150 mm); light source: mercury lamp, power=5 W, λ=365 nm; average I=6.8 µW/cm^2	XRD, AFM, XPS, FTIR	PVD	(88)	Sample's dimension was 100×100 mm^2 (eight slides were put together). The solution of pollutant was almost transparent after 9.5 h, but the solutions without TiO_2 film sample displayed a little orange color.
1D/ 0D	Rhodamine B (10 ppm) Aqueous medium	F Free-standing mats	A glass beaker (h=9 cm, Ø8 cm), V=250 mL; UV light source: power=15 W, λ=365 nm); d for:	SEM, EDX, XRD	E-spinning matrix PAN powder TiO_2 (Anatase, Acros)	(145)	Reactions were conducted with two different positions of mats (0.039 g, 4.5×4.5×0.3 cm^3): floating and immersed. Experiment duration was 50 h. A negligible effect of UV light alone was recorded. The results showed that the floating

			floating position 4 cm; bottom position 10 cm				PAN-TiO_2 mat had higher dye color removal (60%) compared with the immersed one (20%).
1D/ 0D	MB (10 ppm) Aqueous medium	F Free-standing mats	A glass beaker, V=100 mL in closed chamber (0.4x0.4x0.4 m) equipped with 8 UV-A lamps (power=8 W, λ=315–380 nm.)	SEM, EDS	E-spinning matrix PAN powder TiO_2 (anatase, Aldrich Inc.)	(42)	Different H_2O contents (3–5 w/w%) were used to create porous structure of PAN-TiO_2-NF (TiO_2 load 0–3 wt%). The web of size was 3x3 cm. Experiment duration was 24 h. ~80% of pollutant was degraded. Higher TiO_2 loading resulted in higher PCO activity. H_2O addition exhibited slightly higher photocatalytic activities.
1D	MB (20 ppm) Aqueous medium	F Dispersed	The reactor comprised two half-cylinders (h=28.7 cm) each one contained 6 lamps of UV-A light source (power=8 W, λ=355–360 nm), V=125 mL	SEM, TGA/DTA, BET, XRD	E-spinning matrix PVP prec. TTIP	(138)	As-spun fibres were calcined at 500 and 1000°C. BET of TiO_2-NF (500°C and 1000°C) was 53.42 and 2.04 m^2/g. 50 mg of the photocatalytic material was used in 45 min experiments. PCO efficiency of TiO_2-NF (500°C) was 80.2%. Samples heated in higher temperatures showed poorer results.
1D	Ranitidine (1 mM) Aqueous medium	S Quartz substrates	Quartz cylindrical reactor, in acrylic box (20x20x20 cm), V=60 mL; light source: two sets of 3 black light lamps (power=4 W, λ=350–400 nm, I =160 $\mu W/cm^2$).	FESEM, XRD	E-spinning matrix PVP prec. TTIP	(97)	Duration of experiments was 120 min. PCO degradation rate on the TiO_2-NF film and Degussa P25 nanoparticles was determined to be 0.0080 and 0.011 min^{-1}, respectively. TiO_2-NF film showed good recyclability.
1D	Methyl Orange (50 mg/L) Aqueous medium	F Dispersed	Self-made reactor with irradiance from top and cooling system; UV light source: mercury lamp, power=300 W, λ=360 nm; d=30 cm	XRD, AFM	E-spinning matrix PVP prec. TBT	(99)	Duration of experiments was 20 min. Concentration of TiO_2-NF was 2 g/L. Methyl orange was decomposed completely.

1D	MB (20 mg/L) Aqueous medium	F Dispersed	Photoreactor – n.a. V=20 mL with catalyst (20 mg)	XRD, SEM, BET	E-spinning matrix PVP prec. TTIP	(62)	Solid and porous TiO_2-NF. BET of samples were 9 and 33 m^2/g. 2 h experiments. Slight sorption of pollutant has been measured. Solid TiO_2-NF decomposed 50% of pollutant in the first hour, while porous TiO_2-NF decomposed 90% in the same period of time. The reaction rate constant of porous TiO_2-NF (0.035 min^{-1}) is three times higher than of solid TiO_2-NF (0.011 min^{-1}).
1D	MB (50 mg/L) Aqueous medium	F Dispersed	A glass beaker, V=150 mL; light source: xenon lamp, power=150 W	SEM, TEM, XRD, BET	E-spinning matrix PVP prec. TTIP	(139)	Solid TiO_2-NF and hierarchical TiO_2 nanostructures. BET were 52.43 and 94.01 m^2/g. Duration of experiments was 150 min. 50 mg of dried catalyst was dispersed in solution. PCO efficiency for TiO_2-NF and hierarchical TiO_2 were 92.5% and 94.6%.
1D	MB (10 mg/L) Aqueous medium	F Dispersed	Photoreactor – n.a. V=100 mL; UV light source: power=24 W, λ=254 nm	TGA, HRTEM, XRD, BET, FTIR	E-spinning matrix PVP prec. TTIP	(60)	Solid and Zr-doped TiO_2-NF has been synthesized with different amount of Zr (5–20mol%). BET were 7 and 38.8 m^2/g. Duration of experiments: 30 min. 20 mg of photocatalysts was used in experiments. PCO efficiencies for solid and Zr-doper (5, 10, 20 mol%) TiO_2-NF were 61.4, 73.5, 95.4, and 69.3%, respectively.
1D/ 0D	MB (10 mg/L) Aqueous medium	F Dispersed	n.a.	XRD, SEM, XPS	E-spinning matrix PVP powder TiO_2 (P25, Degussa)	(143)	Polymer NF with different loading of TiO_2 (0–10 wt%). Duration of experiments was 90 min. 0.01 g of catalyst was dispersed in 50 mL of solution. PCO efficiencies ranged 75–94% with increasing loading of TiO_2 powder (1–7 wt%) loading. Afterwards a slight decrease was recorded.

2D	Ethanol (273 ppm) Aqueous medium	S Microscope glass, sodium-free glass	SS batch reactor with a volume of 8.75 L; light source: mercury lamp, power=100 W; d=15 cm	XRD, FEG-SEM, Electron spectroscopy for chemical analysis	PVD	(89)	The thin films samples area was 31x25 mm^2. For thicker films the photocatalytic activity showed only a very small increase. The photocatalytic activity of the thin films decreased with the increasing sputtering power.
1D/ 0D	MB (10^{-2} mM) Aqueous medium	F Free-standing mats	Quartz cell (40x40x10 mm), V=13 mL; light source: high power LED, 700 mA, λ=365 nm	SEM, FTIR, DSC	E-spinning Matrix PA12 powder TiO_2	(146)	NF with different loading of TiO_2 (0–20 wt%) and size of 3.5x3.5 cm^2 electrospun samples (thickness ~70 mm). Duration of experiments was 100 min. PA12 fibres did not show a significant sorption of pollutant. PCO efficiencies ranged 41–98% with increasing loading of TiO_2 powder.
1D	Rhodamine B Aqueous medium	F Free-standing mats	n.a.	TG-DTA, SEM, XRD	E-spinning matrix PVP prec. TiBu	(153)	As-spun TiO_2-NF were annealed in different temperatures for different periods of time, 350–550°C for 1–3 h. TiO_2-NF membranes (10×10 mm^2, m=20 mg) were used for 2 h experiments. PCO efficiency for TiO_2-NF was 72%.
1D/ 0D	MB (10 ppm) Aqueous medium	F Free-standing mats	Petri dishes (h=1.5 cm, Ø5.5 cm), V=35 ml; UV light source: λ=365 nm	SEM, TEM, FTIR, XRD	E-spinning matrix PA6 hydrothermal TiO_2 powder	(147)	Polymeric nanofibres with different content of graphite oxide (GO 1.36–9.1 wt%) and TiO_2 powders. Matrices (5x5 cm) for 3 h experiments were used. PA6-NF with GO and TiO_2 had efficiency of 60%, while PA6-NF just with TiO_2 showed 45% efficiency. Composites demonstrated good recyclability.
1D	basic blue 26, (10 mg/L)	S Glass substrate	Quartz cell (45×45×100 mm); UV	XRD, FESEM, BET	E-spinning matrix PVAc prec. TTIP	(43)	TiO_2-NF and additionally decorated TiO_2-NF with TiO_2 powder. BET of TiO_2-NF were 39 and 26 m^2/g. Sorptions were 1.9% and 3.2%. Samples

	Aqueous medium		light source: power=60 W				of 35×75 mm^2 were used in 3 h experiments. PCO efficacies for TiO_2-NF and decorated TiO_2-NF were 25.3% and 78.7%. Samples demonstrated good recyclability.
1D	MB (10^{-5} M), benzene (100 ppm) Aqueous and air medium	F dispersed for MB S Filter mesh for benzene	Aqueous experiment: wood chamber (40x5x32 cm), V=50 mL; light source: fluorescent lamp (power=15 W, λ=435 nm, I=1100 lx); experiment in air: acrylic tube (0.5 cm thick) with outer illumination; light source: 4 fluorescent lamps (power=18 W, λ=435 nm, I=5400 lx), d=5 cm	XRD, TGA, BET, UV-vis spectroscopy, FE-SEM	E-spinning matrix PVP prec. TiBu	(57)	TiO_2-NF and CNT/TiO_2-NF were tested. BET of TiO_2-NF and CNT/TiO_2-NF were 44 and 116 m^2/g. Experiment duration for both media was 180 min. 0.05 g of catalyst was dispersed in aqueous solution. The sorption of TiO_2-NF was 8%, while CNT/TiO_2-NF demonstrated up to 18–32% with increasing content of CNTs. PCO efficiencies were 14% for TiO_2-NF, 35–58% for CNT/TiO_2-NF with increasing content of CNTs. For benzene decomposition only CNT/TiO_2-NF were investigated. Different number of filters with NF were used: 6–18 (active area=0.0126 m^2/filter). Sorption as well as efficiency, increased with filters number: 15–35% and 45–52%, respectively.
1D	BTEX (0.1 ppm for each compound) Air medium	S Aluminum foil	Continuous-flow Pyrex reactor (h=25 cm, Ø3.8 cm); light sources: UV light (fluorescent black light lamp, power=8 W, λ=352 nm), visible light (fluorescent daylight lamp, power=8 W, λ= 400–720 nm)	SEM, EDX, XRD, diffuse reflectance UV-VIS-NIR spectra	E-spinning matrix PVAc prec. TTIP	(140)	PVAc-supported CNT-TiO_2 composite NF with different CNT to TiO_2 weight ratios. Flow rate 1 L/min, RH=45%. Duration of experiments was 3 h. Addition of CNT increased PCO efficiencies. The highest PCO activity was achieved with optimal amount of CNT for both light sources. BTEX obtained for CNT-TiO_2-NF (ratio of 0.056) were 78, 94, 96 and 97%, whereas those obtained for TiO_2-NF were 60, 88, 93 and 94% with UV light. Results followed the same pattern

							with vis. light, but efficiencies were few times lower.
1D	Toluene and isopropyl alcohol (0.1 ppm for each compound) <u>Air medium</u>	S Aluminum foil	Continuous-flow Pyrex reactor (h=25 cm, Ø4.5 cm); light sources: UV light (fluorescent black light lamp, power=8 W), visible light (fluorescent daylight lamp, power=8 W)	FE-SEM, EDX, XRD, UV-vis absorption spectra	E-spinning matrix PVP prec. TBT	(141)	PVP-based CNT-TiO_2 NF with different mixing ratios of polymer to CNT. Flow rate 2 L/min, RH at 90%. Duration of experiments was 3 h. The average PCO efficiencies increased with the mixing ratios of polymer to CNT. Decomposition of pollutants obtained for samples with the lowest polymer ratio were 73 and 94%, while for samples with the highest ratio were 96 and 100% with UV light. Results followed the same pattern with visible light, but efficiencies were few times lower.
1D/ 0D	NOx (1 ppm) <u>Air medium</u>	S Glass plate support	A small glass tube with outer illumination; light source: black light fluorescence lamp, power=15 W, λ=365 nm, in a planar arrangement; the d was adjusted to maintain I of 1 mW/cm^2.	XRD, SEM, EDS	E-spinning matrixes PA6, PS, PUR hydrothermal prec. $TiOSO_4{\cdot}H_2O$	(154)	TiO_2 coatings were grown on different polymeric nanofibres via heterogeneous nucleation. All samples contained ~5 mg of deposited TiO_2 onto an area of 50 cm^2. RH=50%. The conversions of NOx (photonic efficiency) at the beginning of irradiation were 16.2 (0.23%), 14.0 (0.2%), and 8.3% (0.12%) for the PS, PA6, and PUR nanofibre materials, respectively.
1D/ 0D	BTEX (0.1–2 ppm of each) <u>Air medium</u>	S n.a.	Annular-type Pyrex reactor (h=26.5 cm, Ø4 cm); inner light source: UV lamp (fluorescent black light, power=8 W, λ=352 nm) or UV LEDs (power=3.1 W,	FESEM, SEM, XRD, EDX	E-spinning matrix PAN powder TiO_2 (anatase, Aldrich Inc.)	(144)	PCO efficiencies were tested under a variety of experimental conditions: different TiO_2 loadings (0.05−1), initial conc. (IC, 0.1−2 ppm), inlet flow rates (FR, 1−4 L/min), RH (20−90%). Experiment duration was 3 h. For the highest TiO_2 ratio, PCO efficiencies were close to 100% for the target compounds, for the lowest TiO_2

			λ=365 nm and λ=380 nm) supported by a hexahedral tube; the inlet gas stream was composed of four flow lines				ratio: <30%. PCO efficiencies revealed a decreasing trend with increasing IC. At the lowest IC PCO efficiencies were 85−94%, whereas at the highest IC they were 9−53%. The adsorption on the surface of the catalyst was a major parameter influencing the PCO. PCO efficiencies decreased 1.5 times and ~10% as the FR and RH increased, respectively. The average efficiencies of BTEX obtained from the UV lamp were substantially higher than those of the UV LEDs. Moreover, UV LED with lower light energy exhibited higher PCO efficiencies than those of UV LED with higher light energy.
1D/0D	Trichloro-ethylene (0.1–2.0 ppm) Air medium	S n.a.	Pyrex tube (h=26.5 cm, Ø4.5 cm); inner light source: UV lamp (fluorescent black light, power=8 W, λ=352 nm)	TG/DTA, FTIR, XRD, SEM, BET	E-spinning matrix PVP prec. TTIP	(155)	TiO_2-NF with different polymeric matrix and TiO_2 precursor. PCO efficiencies were tested under a variety of experimental conditions: initial pollutants conc. (IC, 0.1−2 ppm), inlet flow rates (FR 1−4 L/min), RH (20−90%). Experiment duration was 3h. BET increased with increasing TiO_2 precursor ratios 92−145m^2/g. PCO efficiency increased with increasing TiO_2 precursor ratios 84−94%. PCO efficiency decreased 1.5 times with increasing FR and IC. Increased RH also had a negative effect on efficiency.

a – *S* stands for supported catalysts, *F* stands for non-supported catalysts; b – presents polymeric matrix and TiO_2 precursors, where *TTIP* stands for titanium isorpopoxide; *TBT* – tertabutyl titanate; *TiBu* – titanium butoxide

In the table *V* means the volume of solutions with a model pollutant, *d* – distance between the catalyst sample and light source, *I* – light intensity to the surface of the catalyst.

1.5. Chapter Summary

Even though TiO_2 as a photocatalyst has some limitations, the interest in TiO_2 as the most popular photocatalyst is continuously expanding because of its numerous advantages. Heterogeneous TiO_2-based photocatalysis has been demonstrated as a promising AOPs technique for the treatment of air and water pollution due to the ability to oxidize a variety of environmental pollutants into less or no harmful products instead of accumulating them. Of all the existing forms of TiO_2 photocatalysts, the dimensional anisotropy of TiO_2 nanofibres are advantageous due to the higher surface-to-volume ratio, enabling reduction in the e^-–h^+ pairs recombination rate and a high interfacial charge carrier transfer rate, with both of these effects being favorable for photocatalytic reactions. From all possible synthesis techniques, electrospinning stands out as a simple, versatile, and environmentally friendly method for fabrication of both polymeric and inorganic fibrous materials. Consequently, electropsun TiO_2 fibres act as active photocatalysts themselves and could serve as a support for nanoparticles of noble metals and could be coupled with other semiconductors or non-metals. Therefore, electrospun inorganic TiO_2 nanofibres show a great advantage as photocatalysts, as was described in this chapter.

The possibilities to immobilize TiO_2 nanostructures on various supports are of great importance because of wider possible applications in the cleantech sector and environmental friendliness. Nevertheless, most of the research in photocatalysis using fibrous TiO_2 is still based on a free-standing form of a synthesised photocatalyst. From the existing information, the selection of supports include glass, aluminium foil, and stainless steel (Table 8). Moreover, electrospun polymeric fibres containing semiconductors for the photocatalysis application have also been discussed because this kind of composites afford an excellent recycling property and high surface area for photocatalytic reactions. Nevertheless, the usage of semiconductor nano-powder in the process of electrospinning most often results in agglomeration of the particles in this way reducing the available surface area for photoreactions.

Photocatalytic degradation reactions of organic pollutants as any other kind of chemical reaction must take place in an enclosed volume. The five fundamental steps describe the removal of organic pollutants by heterogeneous photocatalysis, whereas the first one could be controlled by the design and conditions of the PCO reactor (**Subchapter 1.1.**). The most popular PCO reactors for the treatment of organic pollutants in various environmental media have been mentioned and the literature review showed that the plate type reactor (most often in a form of a petri dish) is the most common for wastewater research, while the annular types reactor dominates in the research for the treatment of an air medium (Table 8). Moreover, in the case of the air medium, very small flow rates (1–4 L/min, Table 8) are used, which is not the case in real cases for practical applications.

It is expected that research on the electrospun nanofibres, TiO_2 as well as other SCs as photocatalysts will become more extensive in future and a larger number of new and efficient photocatalysts together with related technologies will emerge, which could be applicable in the photocatalytic treatments of wastewater, photocatalytic reduction of VOCs and other gaseous pollutants, hydrogen production from water splitting, and so on.

The research focuses on the applications of the most established photocatalysts, namely TiO_2 which make the results applicable to the practical uses with respect to the material availability and price. Since the most research of fibrous TiO_2 focuses on a free-stand form, the immobilization issue is one of the focus in this work. Moreover, this study extends the range of most popular supports used to immobilize zero dimensional TiO_2 as well as normally used air flow rates in an air medium as may be seen in **Subchapter 2.3.2.** Furthermore, the morphology examination includes another important parameter, the surface roughness, which will demonstrate a significant influence on the efficiency of the photocatalysis process.

2. METHODS AND MEASUREMENTS

2.1. Synthesis of Different TiO_2 Photocatalysts

2.1.1. Materials Used

As polymeric matrices polyacrylonitrile (PAN) with $Mw \approx 1.5 \cdot 10^5$ (CAS No. 25014-41-9, Sigma Aldrich, UK) in *N*,*N*-dimethylformamide (DMF, 99.8%, CAS No. 68-12-2, POCH S. A., Poland) and polyvinylpyrrolidone (PVP) with $Mw \approx 1.3 \cdot 10^6$ (CAS No. 9003-39-8, Fisher Scientific L.L.C., USA) in ethanol (EtOH, 99.8%, CAS No. 64-17-5, Honeywell International Inc., USA) were used.

Titanium isopropoxide (TTIP, 97%, CAS No. 546-68-9, Sigma Aldrich, UK) and titanium butoxide (TiBu, 97%, CAS No. 5593-70-4, Sigma Aldrich, UK) served as TiO_2 precursors.

Glacial acetic acid (HAc, 100%, CAS No. 64-19-7, POCH S. A., Polanad) was used to control the hydrolysis of organic titania precursors.

Commercial titanium dioxide powder (99.5 %, Aeroxide P25, CAS No. 13463-67-7, Evonik GmbH, Germany) was utilized as a comparative catalyst material.

Commercially available polyamide base resin (PA12 Vestamid L, CAS No. 24937-16-4, Evonik GmbH, Germany) was used to produce a polymeric support.

Poly(ethylene glycol) (PEG, with $M_w \approx 400$, CAS No. 25322-68-3, Sigma Aldrich, UK) was used as a binding agent to make thin layers of the nanofibrous catalyst. Methanol (CAS No. 67-56-1, 99.8%, Chempur, Poland) was used in the coating step of the preparation of catalytic layers.

Positive-tone diazo-naphthoquinone/Novolac resin-based photoresist (HENGLEI Hologram Co., Ltd, China) was used to pattern the support of the thin film TiO_2.

The photocatalytic activity of TiO_2 nanofibres were investigated using Methylene Blue (IUPAC 3,7-bis(dimethylamino)-phenothiazin-5-ium chloride, CAS No. 61-73-4, Sigma Aldrich), Oxalic Acid (IUPAC ethanedioic acid, CAS No. 144-62-7, Sigma Aldrich, UK), and Toluene (IUPAC Methylbenzene, CAS No. 108-88-3, 99.8% Sigma Aldrich, UK) as model pollutants.

2.1.2. Synthesis of Fibrous TiO_2

A great amount of effort has been made to adjust electrospinning conditions that allowed forming fibres containing organic TiO_2 precursors, including adjustments of polymer concentration and composition as well as a needle diameter, voltage, TTCD and environmental conditions, especially relative humidity, which were crucial for the electrospinning process with this polymer. The main stages of the synthesis of fibrous TiO_2 are represented in Figure 6 below.

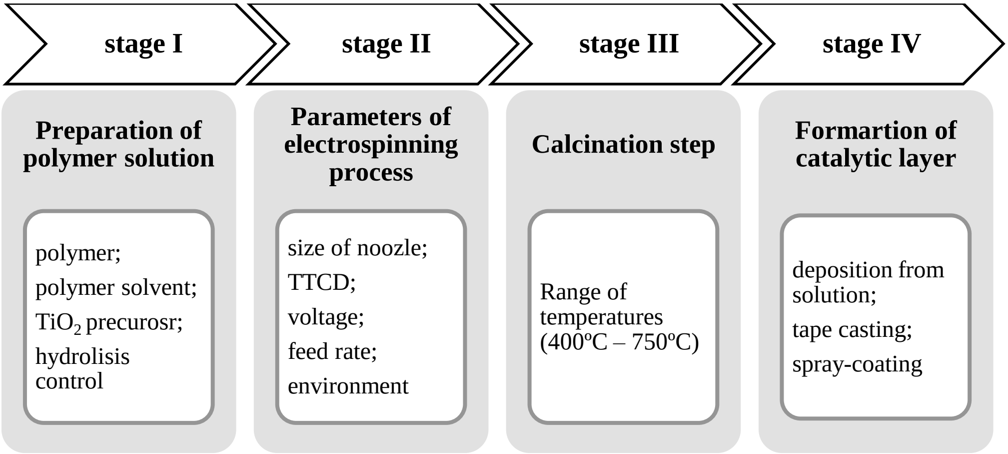

Figure 6. Schematic representation of the main stages of fibrous TiO_2 synthesis in this research work

There were two sets of synthesis of fibrous TiO_2 based on selection of materials for preparation of solution for electrospinning, namely PAN/TTIP and PVP/TiBu as key materials. The parameters of later stages varied accordingly. A detailed description of each stage in each set is given below.

➢ *The first set of materials were with PAN as a polymeric matrix and TTIP as an organic precursor of* TiO_2.

Stage I. The 10.4 wt% PAN solution in DMF was prepared under the continuous stirring for four hours. The TTIP solution was prepared in a separate vial with DMF and HAc. The ratio of components was DMF:TTIP:HAc as 1:0.25:0.4. After PAN dissolved completely in DMF, the TTIP solution has been dripped slowly into the polymer solution with continuous stirring. Subsequently, the incorporated solution was stirred further for at least 15 min before electrospinning. Then the final sol-gel solution was transferred into a custom-made electrospinning setup (Figure 3).

Stage II. The TTCD was fixed at 22 cm. The syringe needle (with 23 G which corresponds to 0.337 mm of the inner diameter) was electrified using 24–27 kV voltage and the polymer solution was ejected via a syringe pump (LSP01-1A, Baoding Longer Precision Pump Co., Ltd., PRC) at a feeding rate of 0.6–0.7 ml/h. The production was collected on a vertically positioned cylindrical collector coated with

SS plate and rotating at a linear speed of 0.025 m/s. The electrospinning was carried out in a closed chamber. As the stability of the electrospinning process of PAN was sensitive to higher RH values, the dry air supply was used so the value of RH would not exceed 40%. The temperature was not regulated and was 22–26°C.

Stage III. As-spun composite fibres were calcined in a muffle furnace (SNOL 8,2/1100, Lithuania) at different temperatures, namely 400–750°C (at rate 5°C per minute, for 2 h), in air with the aim to remove organics and to obtain crystalline structures of TiO_2 fibres. Different temperatures were used to imitate the formation of both crystalline phases of titania, namely anatase (A) and rutile (R). The samples used in the experiments with polyacrylonitrile as a polymer matrix had a note "PAN" (Table 9).

Stage IV. To get photocatalytic layers, synthesized nanofirbous and commercial TiO_2 were mounted on different supports. For that, glass microscope slides were used (size of 2.5x7.5 cm (±0.1). Then the first set of catalytic layers was prepared by the method of solution evaporation. The solution of fibres in methanol was prepared achieving concentration of 0.4 mg/mL. The fibres were thoroughly dispersed using an ultrasonic bath (EMMI 30HC, Emag GmbH, Germany). The glass substrate was placed in the obtained solution and the entire assembly was warmed up to 70°C in order to evaporate the solvent. The Aeroxide TiO_2 powder was also mounted on the same size glass substrate by the spray technique. Then the substrate was calcined at 400°C aiming to achieve better adhesion of fibres to the glass surface. The final catalyst layer used in subsequent experiments had a surface of 18.75 cm^2 (±0.21) and the average surface density was 0.12 mg/cm^2 (±0.04).

- *The second set of materials were with PVP as a polymeric matrix and TiBu as an organic precursor of TiO_2.*

Stage I. The fabrication of TiO_2 nanofibres with PVP was easier to handle since the environmental conditions, such as relative humidity, did not have such a strong effect as with PAN. The 10 wt% PVP solution in ethanol was prepared under the continuous stirring for two hours. After the polymer dissolved completely, separately prepared TiBu solution also in ethanol, containing HAc, has been dripped slowly into the PVP solution. The ratio of components were EtOH:TiBu:HAc as 1:0.5:1. Once again, the incorporated solution was stirred further for at least 15 min before electrospinning.

Stage II. For the electrospinning process the same setup as described above was used. In this case, the TTCD was fixed at 16 cm. The syringe needle (with 23 G) was electrified using 27–29 kV voltage and the polymer solution was ejected via a syringe pump at the feeding rate of 1.3 ml/h. The production was collected on a vertically positioned cylindrical collector coated with SS. Electrospinning was carried out in a closed chamber at ambient conditions (20–25°C and RH 40–45%).

Stage III. As-spun composite fibres were calcined in a muffle furnace (SNOL 8,2/1100, Lithuania) at 500°C (at rate 5°C per minute, for 2 h) in air with the aim to remove organics and to obtain the crystalline anatase structure of TiO_2 fibres. Samples used in the experiments with polyvinylpyrrolidone as a polymer matrix had a note "PVP" (Table 9).

Stage IV. To get photocatalytic layers, synthesized nanofirbous and commercial TiO_2 were mounted on different supports. For that in this part of research, stainless steel (grade 316L) plates and polyamide (PA12) microfibres on stainless steel (SS) 8 mesh (wire diameter 0.8 mm, nominal squared opening size 2.5 mm) were used (size of 2.5x7.5 cm (±0.1) and 10.0x51.0 cm (±0.3) for experiments in aqueous and air media, respectively). The description of production of PA12 microfibres is given at the end of this section. Two different supports required two different methods for immobilization of fibrous TiO_2, namely the tape casting and spray-coating. In case of casting, calcined TiO_2 fibres or Aeroxide P25 TiO_2 nanopowder were thoroughly grounded and mixed with few drops of 40% PEG solution in water. Then the viscous mass was uniformly distributed on the SS plate. In case of the spray-coating, the suspension of calcined TiO_2 fibres in methanol was prepared by means of an ultrasonic bath achieving concentration of fibres of 0.4 mg/mL. Then the solution was uniformly sprayed on the surfaces of PA12 microfibres with some breaks between sprays for the solvent to evaporate. The final catalyst layer had an average surface of 18.75 cm^2 (±0.57) for the experiment in an aqueous medium and 510.0 cm^2 (±5.1) for the experiment in an air medium. The surface densities of the loaded photocatalyst were of 1 mg/cm^2 (±0.03) and 0.06 mg/cm^2 (±0.01) in cases of SS and PA12 microfibrous supports, respectively.

The PA12 microfibres were fabricated using the melt electrospinning technique in a custom-made electrospinning setup. The filament of PA12 was fed at a rate of 1.6 g/h through a 4 mm diameter nozzle. Tip-to-collector distance (TTCD) was fixed at 40 mm. The voltage of 20–25 kV was applied. Polymer melt was obtained at a temperature of 300°C. The melt electrospinning was carried out in a closed chamber at ambient conditions (temperature of 20–25°C and RH of 40–50%). The final thickness of the formed microfibre layer was 3.0 mm (±0.1). The second set of catalytic layers, formed with PVP and TiBu, were prepared by the tape-casting and spray-coating methods, having SS and PA12 microfibres as supports for a TiO_2 nanofibrous catalyst.

2.1.3. Synthesis of Thin Film TiO_2

As opposite to the methods described above, the preparation of thin film TiO_2 has started from the support modification. Thin film TiO_2 was also synthesized by PVD on glass microscope slides (size of 2.3x4.4 cm (±0.4)). The size of supports depended on the available custom photocatalytic reactors, both for experiments in aqueous and air media as well as on the limitations of the coating techniques, such as lithography. Flat surface, line-patterned and grid-patterned samples were prepared. There were five samples accordingly to the distance of the lattice in total (Table 9). The simplified presentation of the main preparation stages is given in Figure 7 below.

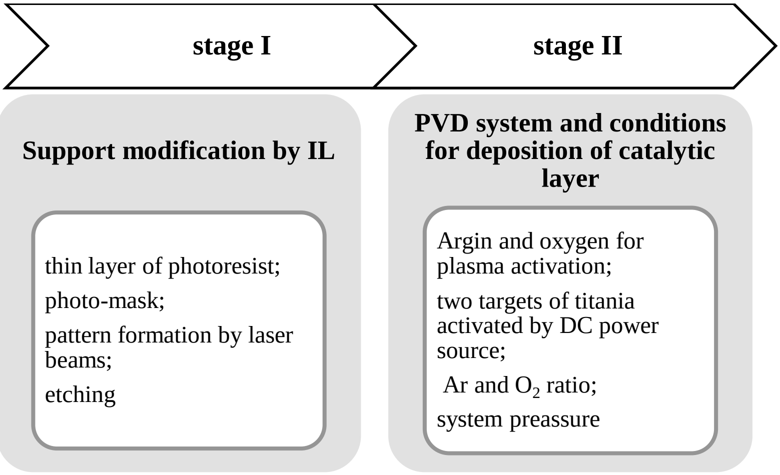

Figure 7. Schematic representation of synthesis of thin film TiO_2 in this research work

Stage I. The positive-tone diazo-naphthoquinone/Novolac resin-based photoresist (HENGLEI Hologram Co., Ltd, China) of approx. 5 µm thickness, spin-coated on glass substrate (size of 23x44x3 mm) was used for the surface structuration procedure. An optical table and a custom setup of mirrors, lenses, and a laser diode module IQµ1H50 405–6B G5T30 (405 nm, 60 mW, Power Technology Inc., USA) were used for the interference lithography (IL) process. The expanded laser beam was directed to a beam splitter and two beams were overlapped on the sample surface through the mask of 21x21 mm size. The ratio of intensity of the beams was approximately 1:1.

Line patterned samples were exposed through the mask two times; thus, two adjacent areas were produced on the same sample. To form the grid-patterned samples, each produced area was exposed once more. The second exposure was performed after rotating the sample by 90 degrees perpendicular to the laser beam. Consequently, two intersecting line pattern structures formed a grid like pattern. The exposed photoresist was developed in NaOH water solution (1% wt) for 20 seconds and dried with the compressed air. Later patterned surfaces were used as a substrate for the TiO_2 film deposition.

Stage II. TiO_2 layers were deposited using the physical vapor deposition (PVD) 75 vacuum system (Kurt J. Lesker Company Ltd, USA). Argon and oxygen gases (with 99,999% purity) were used in deposition during the plasma activation. Two titanium (Ti) targets (99,995% purity) with a diameter of 50.8 mm and thickness of 6.35 mm were used in the process. The direct current (DC) power source was used to activate Ti targets. TiO_2 layers were deposited on a glass substrate with a different structure type in the chamber with vacuum of $5 \cdot 10^{-5}$ Torr, which was produced before every deposition process. Then the chamber was filled with oxygen and argon gases with ratio 20% to 80%, respectively. The deposition process began with stable $5 \cdot 10^{-3}$ Torr pressure and was set at a room temperature without any additional heating. The substrate and targets were separated with a shutter of the magnetron between them while etching process were set to clean the target surface from additional oxygen. Deposition was set for 1 hour and a ~100 nm thickness layer of titania was achieved.

2.1.4. Summary of Synthesized TiO_2 Photocatalysts

The glass, stainless steel, polymer supports were marked as G, SS, PA12 respectively, in samples names. The table below summarizes information on different TiO_2 catalytic layers synthesis.

Table 9. Specifications of synthesis of photocatalytic layers of fibrous TiO_2, including support, coating method, materials, and sample names

Fibrous TiO_2				
Synthesis stages		***Synthesis parameters***		
		First set	*Second set*	
Polymer solution	*Matrix* *Solvent* *Precursor* *Hydrolysis control*	PAN; DMF; TTIP; Acetic acid	PVP; EtOH; TiBu; Acetic acid	
Electrospinning	*Nozzle* *TTCD* *Voltage* *Feed rate* *Environment*	23G, 22 cm, 26 kV, 0,7 ml/h RH ≈ 40%	23G, 6 cm, 29 kV, 1,3 ml/h -	
Calcination		600 – 750°C	500°C	
Catalytic layer	*Support* *Method*	G deposition	SS tape casting	PA12 spray coating
Sample names	*anatase TiO_2* *anatase/rutile TiO_2* *Aeroxide P25**	PAN-NFa-G PAN-NFmix-G PAN-P25-G	PVP-NF-SS - PVP-P25-SS	PVP-NF-PA12 - -
Thin film TiO_2				
Synthesis stages		***Synthesis parameters***		
		Non-patterned	*Line pattern*	*Grid pattern*
Interference lithography	*Photoresist thickness* *Photo-mask* *Exposing times* *Etching*	- - - -	5 µm 21x21 mm two 1% NaOH	5 µm 21x21 mm three 1% NaOH
Thin film deposition	*PVD*	Ar and O_2 of 99.999% purity, with Ar:O_2 as 20:80% at pressure of $5 \cdot 10^{-3}$ Torr.		
Sample names	*Period size of: 0 µm* *approx. 3 µm* *approx. 5 µm*	P-TiO_2	- D3-TiO_2 D5-TiO_2	- D3x3-TiO_2 D5x5-TiO_2

2.2. Characterization of Prepared Samples

I. X-ray diffraction spectra of nanofibres were recorded by the X-ray diffractometer (D8 ADVANCE, BRUKER-AXS, Germany, using Cu Kα radiation). Anatase and rutile mass fractions were calculated from the intensities of XRD diffraction peaks using the Spurr equation (Eq. (17)) which utilizes the ratio of the rutile peak to the anatase peak. The anatase and rutile content in the sample can be calculated as:

$$A = \frac{1}{1+1.26 \cdot \frac{I_R}{I_A}} \; ; \quad R = \frac{1}{1+0.8 \cdot \frac{I_A}{I_R}} \qquad \textbf{Eq.16}$$

where I_A and I_R are the peak intensities of anatase (at 25.176° 2θ) and rutile (at 27.355° 2θ), respectively in the sample.

Crystallite sizes were determined while applying the Scherrer's equation (Eq. (18)) to the width of individual peaks using the software for XRD measurement (DIFFRAC.EVA, BRUKER-AXS, Germany):

$$D = \frac{K \cdot \lambda}{\beta \cdot cos\theta} \qquad \textbf{Eq.17}$$

where K is a shape factor, λ is the wavelength of the incident radiation of the instrument, θ is a half of the diffraction angle and β is equal to the subtraction between the full width at half maximum of the measured diffraction peak and the instrumental broadening the so called the line broadening (156).

II. Material morphologies, geometry, and element composition were observed by a scanning electron microscopy (Carl Zeiss EVO MA10, Germany) with the energy-dispersive X-ray spectrometer (Bruker Quantax 200, Germany), transmission electron microscopy (FEI Tecnai T20 G2, USA) and atomic force microscopy (NanoWizard®3 NanoScience, JPK instruments AG, Germany). A thermogravimetric analysis (PT1600, Linseis Inc., USA) was applied to determine the residual carbon in the samples by gradually increasing temperature up to 1000°C. A white light surface sensor (MarSurf WS1, Mahr GmbH, Germany) was used to measure the roughness and waviness of produced catalytic layers. Brunauer–Emmett–Teller (BET) surface area and pore sizes were characterized by the Micromeritics TriStar II 3020 (USA) nitrogen adsorption-desorption isotherm. The average diameter of fibres was measured from 70–100 points in SEM images using ImageJ software (NIH, USA). The UV-vis spectrophotometer (LAMBDA 25, PerkinElmer Inc., USA) and fluorescent spectrometer (LS-55, Perkin Elmer Inc., USA) were used to measure optical properties of the samples. FTIR spectra at wave range 4000–400 cm^{-1} were recorded with the FTIR spectrometer (Frontier, Perkin Elmer Inc., USA).

III. Theefficacy and kinetics of Methylene Blue (MB) were observed by measuring light absorbance at 665 nm with the UV-visible spectrophotometer (Spectronic GENESYS8, Genesys JSC, USA), while the degradation efficacy and kinetics of Oxalic Acid (OA) were assessed by the total organic carbon analyzer (TOC-L-CSN, Shimadzu, Japan). The degradation efficacy of Toluene was analyzed using the gas chromatograph with the flame ionization detector (GC-2010 Plus, Shimadzu, Japan) according to NIOSH 1501 procedure (157).

IV. The data analysis was performed using the software OriginPro®9 (OriginLab Corporation, USA).

2.3. Determination of Photocatalytic Efficiency of Different Photocatalysts

2.3.1. Aqueous Medium

➢ *Fibrous* $\mathit{TiO_2}$*.* The photocatalytic activity of TiO_2 nanofibres in a water medium was investigated by using MB (230 mL, with concentration of 5 mg/L) and OA (250 mL, with concentration of 100 mg/L) as model pollutants. The photocatalytic decolorization of an organic dye, such as methylene blue, is widely known and used to test photocatalysts (Table 8). In case of the surface mounted catalyst (as opposed to the dispersed in the solution), the surface area may have not been sufficient to register significant decomposition of a very dark-colored MB solution by the UV-vis spectrophotometer. Thus, the MB concentration had to be kept sufficiently low. The analysis by the spectrophotometer led only to the observation of the degradation of the primary compound and did not reveal intermediate products of the decolorization reaction. Thus, the ability of mineralization was tested with oxalic acid with the measurements of total organic compounds (TOC). TOC analysis was used just for the samples prepared with the first set of materials, namely PAN and TTIP.

18W Hg lamp with peak intensity at 254 nm was applied as the UV-C source (Koninklijke Philips N.V., Netherlands). The photometric data of the lamp is provided in **Appendix A. 2.** The pollutants decomposition was tested with UV-C light alone and UV-C together with the catalyst. Another test of the catalyst without UV-C radiation was used to determine sorption capacity of the catalyst. The experiment was conducted at a room temperature with continuous stirring. The samples were taken at regular time intervals, every 30 min, for all sets of experiments. In the case of MB as a model pollutant, 3 mL of a solution were transferred to a cuvette (light path length 10 mm) to measure the decrease in color intensity. Then the solution was transferred back to the experimental photoreactor. In the case of OA, as a model pollutant and TOC measurement, 8 mL (required volume for TOC analyzer) of a solution were transferred to a separate vial and were not returned to the experimental photoreactor.

The prepared catalyst was kept in the dark for half an hour to reach the saturation of pollutants absorbance on the surface of the catalyst (the separate experiment was conducted in the dark for a three-hour test of how long it takes to reach the equilibrium; the results showed that after 30 min the equilibrium between sorption-desorption was reached). A schematic representation and main components of the employed experimental setup of the photocatalytic reactor is provided in Figure 8. Experiments were conducted inside the light-tight system and under room conditions. The characterization of experimental conditions is given in Table 10.

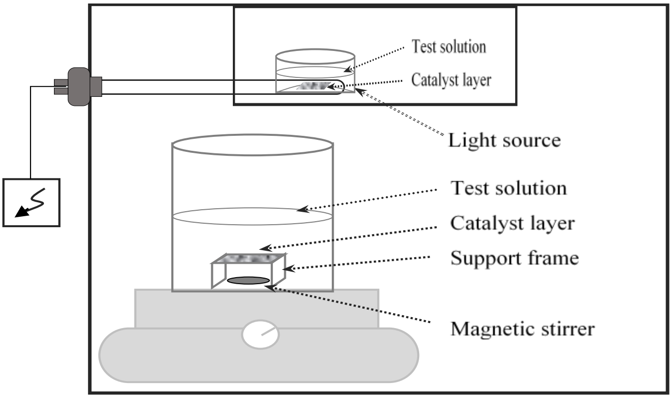

Figure 8. Schematic presentation of the experimental setup for photocatalytic tests in an aqueous medium with fibrous TiO_2 layers (with thin films of TiO_2 given as intercept)

➢ *Thin film TiO_2.* The photocatalytic activity of TiO_2 films were investigated with similar condition as with fibrous TiO_2 layers by using just MB with the same concentration as model pollutant. The volume of pollutant solution was chosen in an experimental way. This was because the thin layer has limited the ability to demonstrate the significant decomposition of model pollutant for bigger volume of the solution. The final experimental volume was 35 mL and experiments were conducted without stirring in a Petri dish (inset of Figure 8). The characterization of experimental conditions is given in Table 10.

Table 10. Description of experimental conditions in an aqueous medium for different dimensionality TiO_2 photocatalysts

Conditions	***Nanofibrous TiO_2***	***Thin film TiO_2***
MB solution volume, mL	230	35
MB solution initial concentration, mg/L	5	5
OA solution volume, mL	250	-
OA solution initial concentration, mg/L	100	-
Light source	UV-C	UV-C
Photocatalyst dimensions, (w x l, cm^2)	2.5 x 7.5	2.3 x 4.4
Photocatalyst surface area on support, cm^2	18.75	10.1
Surface loading of the photo-catalyst, mg/cm^2	on G 0.12 on SS 1.0 on PA12 0.06	100 nm *
Distance between the catalyst and light source, cm	7	7
Initial thickness of the solution layer above the surface of the photocatalyst layer, cm	2	0.7
Reactor dimensions, cm	h=10, Ø 10	h=1.1, Ø 9
Ambient conditions	temp. 19–24°C	

* film thickness

The entire sample surface (1012 mm^2) coated with TiO_2 film was used in photocatalytic experiments but only a part of the surface was patterned. Therefore, the ratio of patterned to whole sample area was calculated. This ratio and the time needed to decompose 50% of the model pollutant were used to calculate the relative time (t_r) needed to decompose 50% catalytic effectiveness as follows:

$$t_r = t_D - (t_P - t_D) \cdot \frac{(1-s)}{s} \qquad \textbf{Eq.19}$$

where: t_D – experimentally determined 50% catalytic effectiveness with a patterned TiO_2 sample; t_P – experimentally determined 50% catalytic effectiveness with a plain TiO_2 sample; s – ratio of a patterned area to the whole sample area.

2.3.2. Air Medium

➢ *Fibrous TiO₂*. The photocatalytic oxidation of toluene vapor (with initial concentration of 1 ppm) was performed in a cylindrical reactor with a length of 65 cm and an inside diameter of 4 cm (Figure 9) with walls covered by the TiO_2 nanofibrous layer (on different supports, namely SS and PA12) or Aeroxide P25 TiO_2 powder layer (on SS plates). The UV lamp was installed in the middle of the cylinder. The distance between the lamp and the wall was 0.8 cm.

The activated carbon filter and HEPA filter were used to clean up the laboratory air used as the main airstream for the experiments. The toluene-air mixture was prepared in the dilution chamber. The toluene vapor was introduced in the airstream by the whiff of pure N_2 gas through the impinger. A certain amount of liquid toluene was added to the impinger and left for at least 24 h before experiments so the equilibrium between the liquid and gas phase toluene would be reached. The photoionization detector (IQM 60, Aeroqual Ltd., New Zealand) was used to monitor the toluene concentration in the photoreactor until the desirable concentration was reached. The toluene-air mixture was introduced with different linear velocities of 0.1 m/s, 0.2 m/s and 0.3 m/s to simulate various residence times inside the photoreactor.

Photocatalysts were left in the dark for 2 h before each experiment to reach the absorption-desorption equilibrium with toluene vapor. UV radiation was provided by the 40W UVC lamp (LightTech Inc., Hungary). The experiment was conducted at room conditions, i.e. at temperature of 19–24°C and RH between 40 and 50%. Samples were collected at inlet and outlet of the reactor before the experiment and an hour after UV light was turned on. Blank samples introducing only the airstream were also collected.

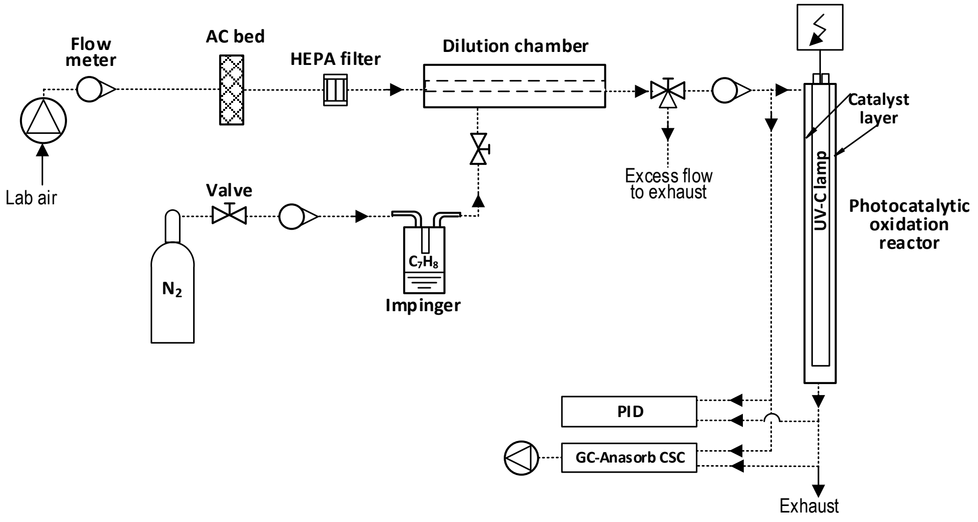

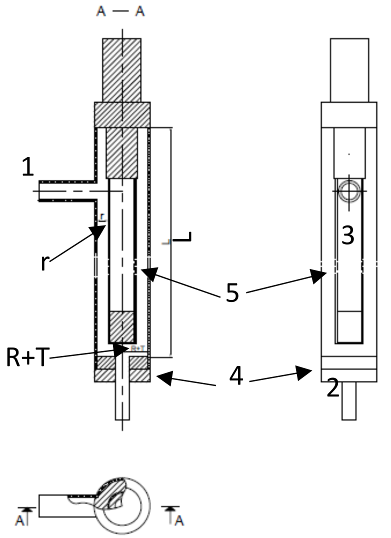

Main parts of the scheme	
r	0.8 mm
R+T	20+2 mm
L	650 mm
1	inlet
2	outlet
3	UV source
4	sealing
5	place for catalyst

Figure 9. Schematic presentation of the experimental setup (top) and a detailed scheme (bottom) of photocatalytic degradation of gaseous toluene with nanofibrous TiO_2 and Aeroxide P25

Air samples were collected using solid sorbent tubes with coconut shell charcoal (SKC Inc., USA) according to NIOSH 1501 recommendations (157). In brief, the sealed tips were cut of just before sampling and the air was drawn 180 mL/min for 7 min with the sampling pump (Universal PCXR4, SKC Inc., USA). After sampling, the tips of the tube were tightly closed with caps and kept in the fridge until the analysis. The experimental conditions are given in Table 11.

The laboratory analysis of the samples were performed in accordance with the recommendations of NIOSH 1501 (157).

Table 11. Description of experimental conditions for testing TiO_2 photocatalysts in an air medium

Conditions	***Cylindrical reactor***
Toluene initial concentration, ppm	1
Light source	UV-C
Photocatalyst dimensions, (w x l, cm^2)	10.0 x 51.0
Photocatalyst surface area on a support, cm^2	510.0
Surface density of the loaded photocatalyst, mg/cm^2	on SS 1.0 on PA12 0.06
Linear air flow rates, m/s	0.1–0.3
Distance between the catalyst and light source, cm	0.8
Reactor dimensions, cm	h=65, Ø 4
Ambient conditions	temp. 22–26°C and RH 40–50%

- *Thin film TiO_2*. Experiments with thin TiO_2 films were not conducted because of a limited area of the photocatalyst that could be synthesized with available instrumentation for lithography and PVD techniques.

3. RESULTS AND DISCUSSION

Before the presentation of the main results and findings, it is worth mentioning once more that from all the organic precursors of titania, the TIPP and TiBu are the most widely used as opposed to the electrospinning of solutions containing TiO_2 nanoparticles, which faces severe challenges. Furthermore, the design of photoreactors was selected according to the literature review and the fact the that plate and annular type of reactors are important in studies to determine kinetic parameters. Moreover, the initial concentrations of organic model pollutants that were used in the research were higher than concentrations that usually would be found in real case waste streams for the same purpose.

3.1. Results of Fibrous Photocatalysts

3.1.1. Structural Characterization of Fibrous TiO_2

I. Crystallinity. As already mentioned, the crystalline phase and crystallinity degree as well as the size of crystallites of SC are important factors affecting the efficiency of PCO.

➢ *The first set of synthesis experiments with PAN and TTIP*. The crystalline phases of the synthesized nanofibres of TiO_2 were researched with the aim to achieve the crystalline composition with the highest catalytic activity. The formation of the phases of TiO_2 depends significantly on conditions of the calcination step in the fibres synthesis process. In the nanofibres synthesis with PAN as a polymeric matrix and TTIP as the precursor of titania, as-spun fibres were calcined at different temperatures (450–750°C) in order to achieve different crystalline phases of titania. At the calcination temperatures lower that 500°C no crystalline phase was yet formed (Figure 10, left). The anatase crystal form was formed at the temperature higher than 600°C, while the phase transformation occurred at the temperature higher than 700°C when both crystal forms of TiO_2 have been activated. These temperature ranges agree well with the results of other research where the initiation of the transformation of anatase to rutile was determined at an interval of 500–900°C, which is higher than of a bulk material (43, 158). At the calcination temperature of 750°C, the allocation of anatase and rutile mass fractions within the crystalline phase was calculated at 28% and 72%, respectively. This is comparable to the commercial TiO_2 nanopowder (23% and 77%, data provided by the manufacturer). The above allocations obtained from the XRD analysis only refer to the distributions between fractions in the crystalline phase.

The size of TiO_2 anatase crystallites in calcined fibres lied in the range of 12.9–18.7 nm as determined by the XRD analysis (Table 12). This is higher than the observed size of 7.3–11.3 nm by Mehrpouya et al. (95) who also used PAN as a polymeric matrix.

The remains of elemental carbon formed during the calcination process, as the residual of PAN, may have influenced a relatively higher temperature range for the formation of crystals in TiO_2 fibres. During the calcination process, anatase crystals were developed simultaneously with the formation of elemental carbon structures. A high specific surface area of carbon brought a decrease in the surface energy of the nanoparticles which led to a higher stability of anatase crystals in high temperatures and hence higher anatase crystal content. Similar observations were reported by Mehrpouya et al., 2012 (95).

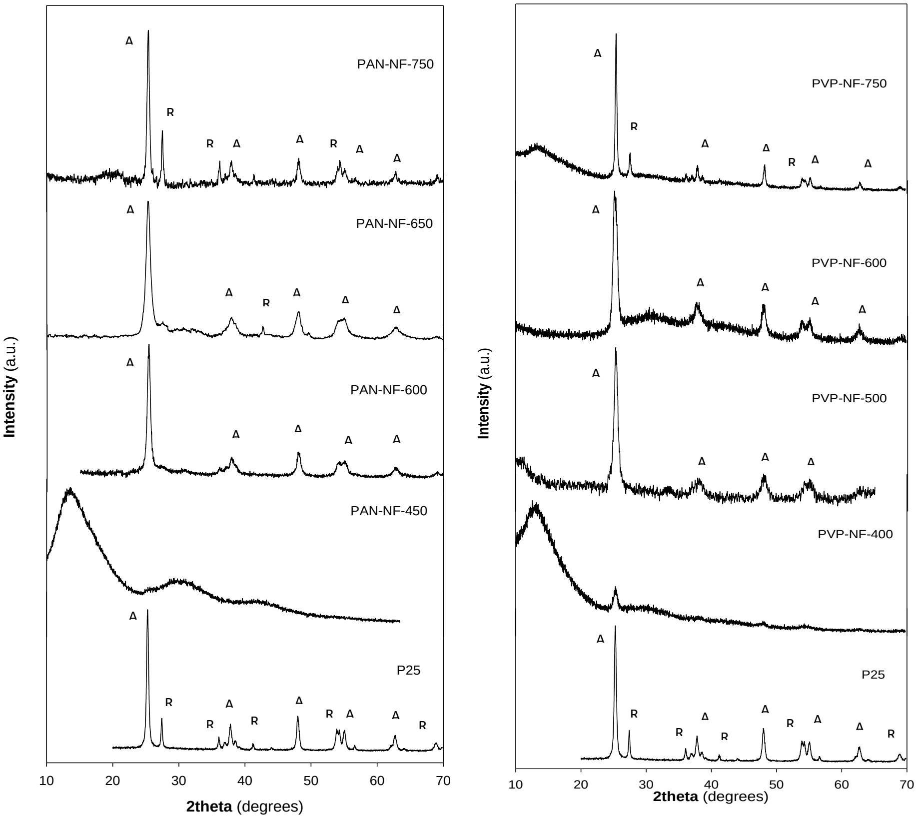

Figure 10. XRD spectra of Aeroxide P25 powder and synthesized TiO_2 fibres of different precursors and matrix (TTIP, PAN on the left and TiBu, PVP on the right), calcined at different temperatures. *A represents anatase phase, R represents rutile phase

➢ *The second set of synthesis experiments with PVP and TiBu.* Since the most applications of TiO_2 as a photocatalyst have been carried out with the anatase phase, it was sought to form nanofibres containing primarily anatase for the later experiments. This was achieved using moderate calcination temperatures (Figure 10, right). The anatase phase was formed at the temperature of 500°C, as confirmed by the XRD analysis and agreed with the best conditions found by many other research (59, 61, 62, 138, 139).

The average and well-defined crystallites of a size of 14.2 nm were identified and found to be similar to the average crystallite size of samples synthesized from PAN and TTIP (Table 12). While the known crystallites size of Aeroxide P25 is around 25 nm. The size of crystallites formed during the calcination process of as-spun PVP and TiBu fibres were somehow smaller than those found by other researchers, for example, Mondal et al. (61) found crystallites sizes between 23.6 and 53.3 nm, which increased with the increasing calcination temperature (300–700°C). This is because the rutile crystalline form appears at higher temperatures, and as it was discussed above (**Subchapter 1.2.1.**), rutile has a bigger crystallites size as compared to anatase.

II. Morphology and Elemental Composition. The EDS analysis and elemental composition map confirmed that an even distribution of TiO_2 over the length of a fibre has been achieved for both, PAN with TTIP and PVP with TiBu as starting materials (Figure 11).

The morphology of fibres was essentially achieved during the calcination process, both for PAN and PVP as a polymer matrix for the titania precursor. Before the calcination, fibres were smooth (Figure 12 (a), (g)) as a result of a polymer matrix hosting the TiO_2 precursor. After the calcination, the surface became rougher, which is a result of the removed polymer during the calcination and titania being the predominant matrix of the fibre (Figure 12 (b-c), (h)). The roughness can be related with the formation of crystallites which can be clearly identified from TEM images (Figure 12 (d-f)).

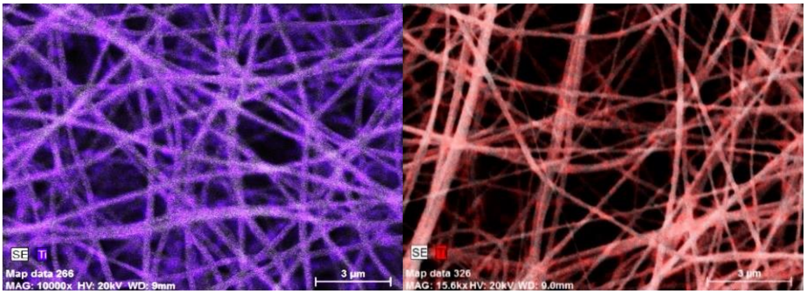

Figure 11. Elemental composition (determined by EDS) of TiO_2 nanofibres with PAN as a polymer matrix (left) and with PVP as a polymer matrix (right)

This is a major achievement over the earlier presented data using TiO_2 nanoparticles as precursors (as opposed to the organic precursors of TiO_2), which reported agglomeration or non-uniform distribution due to electrostatic repulsions formed by the positive charges of both TiO_2 particles and fibres in the final product (144). Moreover, the rising suppression and diffusion of organic molecules have been indicated as a major drawback of this approach (36). Therefore, the formation of titania fibres using organic precursors is advantageous for the formation of uniform distribution of TiO_2 crystals. The mass of Ti in fibres comprised 19.4% and 40.54% before and after the calcination process, respectively.

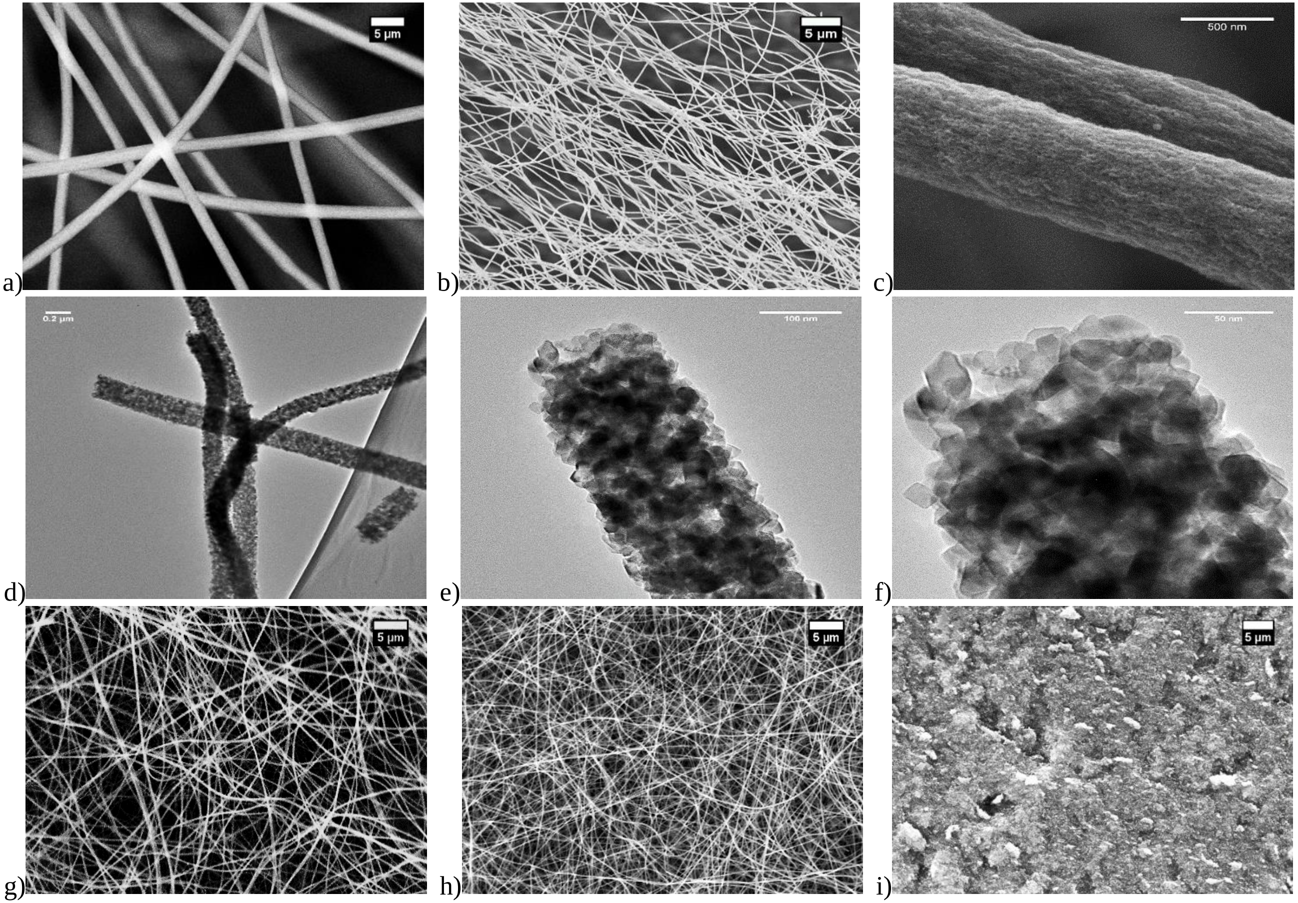

Figure 12. SEM images of TiO_2 nanofibres: (a) before and (b), (c) after calcination with PAN as a polymer matrix; (g) before and (h) after calcination with PVP as a polymer matrix; (i) layer of TiO_2 powder Aeroxide P25; (d), (e) and (f) TEM images of TiO_2 nanofibres after calcination

FTIR spectroscopy, used to explore the chemical groups of synthesized samples, equally confirmed the presence of TiO_2 crystalline form and removal of the most organics (**Appendix A. 3.**). As-spun fibres, both with PAN and PVP as polymer matrixes, clearly show broad peaks that are typical for C-H (2800–3000 cm^{-1}), C-O-C (1100–1600 cm^{-1}), C=C (1600–1650 cm^{-1}), C=N (1600–1850 cm^{-1}), C=O (1670–1800 cm^{-1}) vibrations, a notable peak at the range of 3000–3500 cm^{-1} is attributed to the –OH groups. FTIR spectra after the calcination indicate much fewer clear peaks. The main peak at low range (<1000 cm^{-1}) usually is considered as Ti-O-Ti and Ti-O-C vibrations with the one around 690 cm^{-1} being a match for the anatase phase of titania (61, 112). As peaks at a high range (>3000 cm^{-1}) show the presence of –OH groups, the peak at around 3440 cm^{-1} could be attributed to Ti-OH since TiO_2 is a hydrophilic material.

The influence of main parameters of electrospinning (Table 6) to the morphology of fibres were not assessed in this research because the polymer served only as a matrix or, in other words, a carrier of the organic precursor of TiO_2 and was removed in further steps.

➢ *The first set of synthesis experiments with PAN and TTIP*. The removal of the PAN and activation of titania in elevated temperatures resulted in the almost five-fold reduction of the fibre diameter (Figure 13, Figure 12 (a-c), Table 12). Fibres containing only the anatase phase titania were of a larger diameter compared to fibres containing both phases (327±56 nm vs 261±37 nm, Figure 13, Table 12), and this difference was statistically significant (Student's *t*-test, $p<0.05$). These findings agreed well with the previous studies that observed TiO_2 consisted fibres formation at different temperatures (61, 138). The shrinkage in diameters was caused not only by the removal of organics (solvent, matrix, precursor), but also by changing the crystal morphology and more compact arrangement of grains (138).

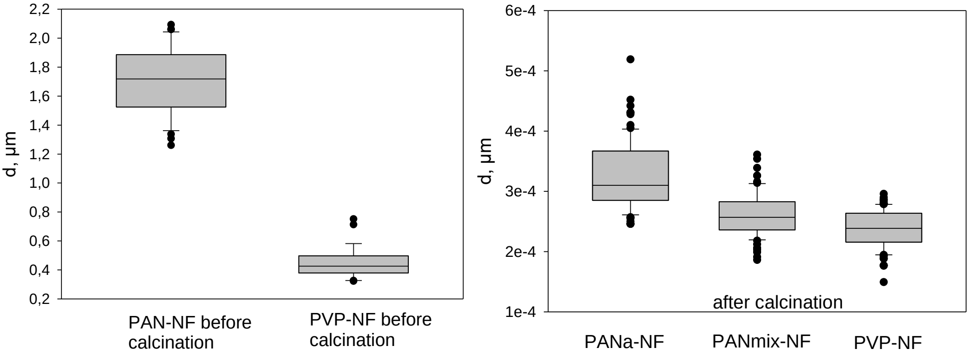

Figure 13. Fibers diameters before (left) and after (right) calcination with PAN/TTIP and PVP/TiBu as initial materials

➢ *The second set of synthesis experiments with PVP and TiBu*. The obtained fibres had homogeneous surfaces with a mean diameter of 230±30 nm (Figure 13). The removal of PVP resulted in ~1.5 times reduction of fibre diameters. Similarly, Mondal et al., and colleagues (61) observed 60−70% shrinkage in the fibre diameter.

The formed fibres had additions of carbon as a product of the calcination of PVP. The remaining percentage of carbon in the nanofibres is less than 4% of the total mass based on the TGA analysis (Figure 14). The effect of carbon could be both, positive and negative. Carbon could serve as an adsorbing agent since many studies combines TiO_2 and carbon forms, as was mentioned in **Subchapter 1.4.**, but the presence of carbon could work as recombination centers and reduce the efficiency of e^- - h^+. The elimination of the remaining carbon requires rather high temperatures (>900°C), hence leading to the appearance of the rutile phase, which is not favorable for photocatalysis.

Table 12. Structural characterization of synthesized TiO_2 nanofibres and Aeroxide P25 powders, including mass fractions, crystallite sizes, and particle size

Sample	Structure type	Composition*, %		Crystallite size, nm (mean ± SD)		Particle diameter, nm (mean (median) ± SD)**
		anatase	rutile	anatase	rutile	
Aeroxide P25	0D	77	23	25.2	43	~21
PAN-NFa-G	1D	100	n. a.	15.8±3.5	n. a.	327 (310)±56
PAN-NFar-G	1D	72	28	19.2±0.9	40.3±0.3	261 (257)±37
PVP-NF-SS	1D	100	n. a.	14.2±0.3	n. a.	230 (239)±30
PVP-NF-PA12	1D					
P-TiO_2	0D	amorphous		n. a.		non-structured
D3-TiO_2	2D	amorphous		n. a.		3.4, line pattern
D3x3-TiO_2	2D	amorphous		n. a.		3.6, grid pattern
D5-TiO_2	2D	amorphous		n. a.		5.3, line pattern
D5x5-TiO_2	2D	amorphous		n. a.		5.9, grid pattern

* within crystalline phase; ** size of a period reported for thin films TiO_2

For example, Mondal et al. (61) synthesized TiO_2 nanofibres with different content of carbon residuals (10.91, 6.45, 2.54 wt%) and concluded that higher content of carbon tend to reduce the photocatalytic activity, meanwhile small carbon residue (2.54%) containing TiO_2-NF is found to be as efficient as the pristine TiO_2-NF in photodegradation of the PAH dye.

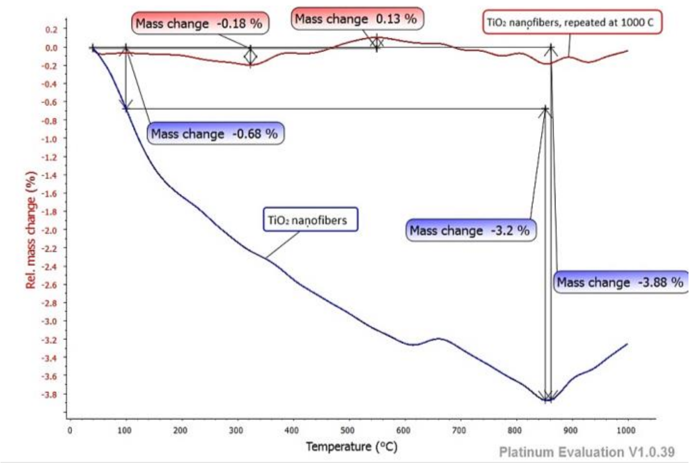

Figure 14. TGA curve of calcined at 500°C TiO_2 nanofibres (blue) and repeated TGA curve of the same TiO_2 nanofibers sample (red)

III. *Specific Surface Area*

➢ *The first set of synthesis experiments with PAN and TTIP*. Despite its larger diameter, nanofibres of pure anatase had a larger specific surface area (58.2 m^2/g, Figure 18) than nanofibres of anatase and rutile mixture (36.3 m^2/g) as well as Aeroxide P25 powder (~35−50 m^2/g). N_2 adsorption isotherm of nanofibres showed low amount of gas intake at the lower range of relative pressure (p/p_0). Thereafter increasing the pressure, gradual adsorption resulted in a hysteresis loop over a higher range of relative pressure (0.7−0.95), which is common for mesoporous materials (Figure 15, left). The hysteresis loop was associated with capillary condensation and indicated slit-shaped mesopores. Both compositions of nanofibres demonstrated existence of wide pores with distributions, which lied in the range of 3−55 nm, although pure anatase nanofibres had narrower pore size distribution and larger pore volume (average pore width 13.5 and 16.4 nm for anatase and mixed phases respectively, given as figure inset, obtained by BJH model). Pore sizes and shapes have been related to the temperature range of the calcination, when at higher temperatures small pores disband due the crystallization of TiO_2 (159).

➢ *The second set of synthesis experiments with PVP and TiBu*. TiO_2 nanofibres had a specific surface area of 83.9 m^2/g (Figure 18). This indicates almost twice bigger surface area of nanofibres as compared to the commercially available TiO_2 spheres. The N_2 adsorption-desorption isotherm is of a type IV (Figure 15, right), once again typical characteristics of mesoporous materials with a loop in the p/p_0 range of 0.4−0.9. The shape of the hysteresis loop indicates the presence of uniform slit-shaped pores in the fibres. The pore size distribution (given as figure inset, obtained by BJH model) shows existence of a sharp peak at 3.1 nm (with an average pore diameter of 4.4 nm) showing narrower pore size distribution compared with the results of fibres obtained from PAN and TTIP.

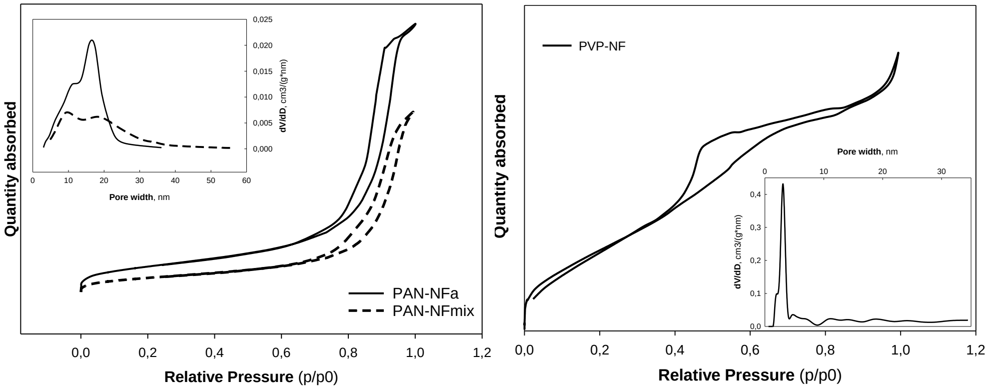

Figure 15. N_2 adsorption-desorption isotherms and pore size distribution of TiO_2 nanofibres consisting of: left – mixture of rutile and anatase phases (PAN-NFmix) and purely anatase (PAN-NFa); right – anatase phases TiO_2 nanofibres (PVP-NF)

Specific surface areas of TiO_2 fibres reported in scientific literature usually vary from few squared meters per gram (60, 62, 138), mostly as a result of high calcination temperatures, to hundreds meters per gram as a result of surface modification pathways, such as doping or usage of surfactants (57, 58, 139, 155). Nevertheless, the most often reported solid TiO_2 nanofibres possess BET specific surface area around 30 m^2/g (Table 8). It could be concluded that a relatively high specific surface area of synthesized TiO_2 fibres was obtained without any additional means.

IV. Surface Roughness. For the description of the surface roughness, the roughness average (Ra) was used. It is an arithmetic average of the absolute values of the profile heights over the evaluation length.

- *The first set of synthesis experiments with PAN and TTIP*. The final layer of the catalyst, using PAN and TTIP, was obtained via the deposition from a solvent. Here fibres shortened down to 30 µm in length and uniformly distributed on a glass substrate forming a compact but fenestrate layer (Figure 16, top right; Figure 17 (a), (b)). The nanofibrous catalyst layer form a rough and porous surface, characterized by a high average surface roughness (R_a) value of 1.31±0.15 µm (Figure 18). On the contrary, the layer of Aeroxide P25 powder demonstrates a relatively smooth surface (Figure 12 (i), Figure 16, top left) with few irregularities (R_a=0.27±0.14 µm, Figure 18). These differences are statistically significant ($p<<0.05$ based on the Student's *t*-test). High surface roughness is a result of the porous matrix formed by fibres potentially providing higher and more accessible macro pore surface area, which was later confirmed by the higher sorption capacity compared to the Aeroxide P25 particle layer.

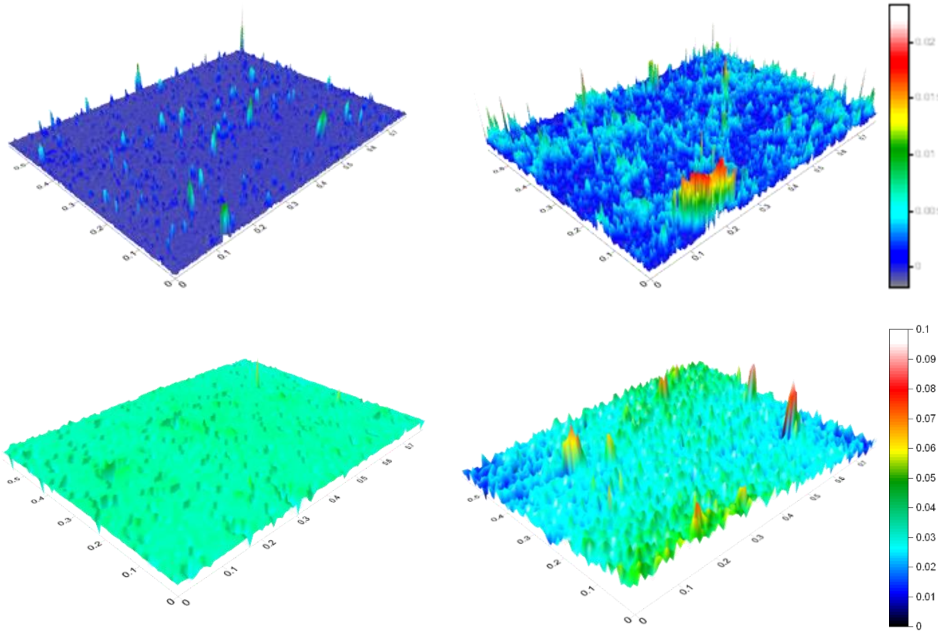

Figure 16. Surface roughness of surface deposited Aeroxide P25 powder (top left) and TiO_2 nanofibres (top right). Surface roughness of tape casted TiO_2 nanofibres layer (bottom right) and tape casted TiO_2 Aeroxide P25 layer (bottom left)

The calculated surface density of the layer for Aeroxide P25 powders, pure anatase nanofibres, and fibres containing a mixture of rutile and anatase were 0.123 mg/cm^2, 0.09 mg/cm^2, and 0.165 mg/cm^2, respectively (Figure 18). The catalyst layers were manufactured with the aim to minimize the amount of substance to form a uniform thin layer without empty or thin spots on a glass substrate. Such approach resulted in substantially different surface densities, which nanofibrous layer being more efficient with respect to material consumption.

➢ *The second set of synthesis experiments with PVP and TiBu.* The morphology of the TiO_2 nanofibre layer on a stainless steel plate is shown in Figure 17 (c), (d). TiO_2 fibres were shortened down to 3–5 µm in length during grinding. The layer can be characterized as uniformly distributed on a substrate forming a compact but a bit spongy layer. High surface roughness (Ra=0.88±0.07 µm, Figure 18) is once again the result of the porous matrix formed by short fibres. Meanwhile, the layer of Aeroxide P25 powder once again demonstrated a relatively smooth surface (R_a= 0.31±0.08 µm, Figure 16 bottom left). In case of the polymer microfibre support, a branchy structure of nanofibres on a microfibre was observed (Figure 17 (e), (g)). TiO_2 fibres shortened down to 5−20 µm in length during the sonication. The average diameter of polymeric microfibres was 5.45±0.59 µm, while the thickness of formed microfibre layer was approx. 3.0±0.1 mm.

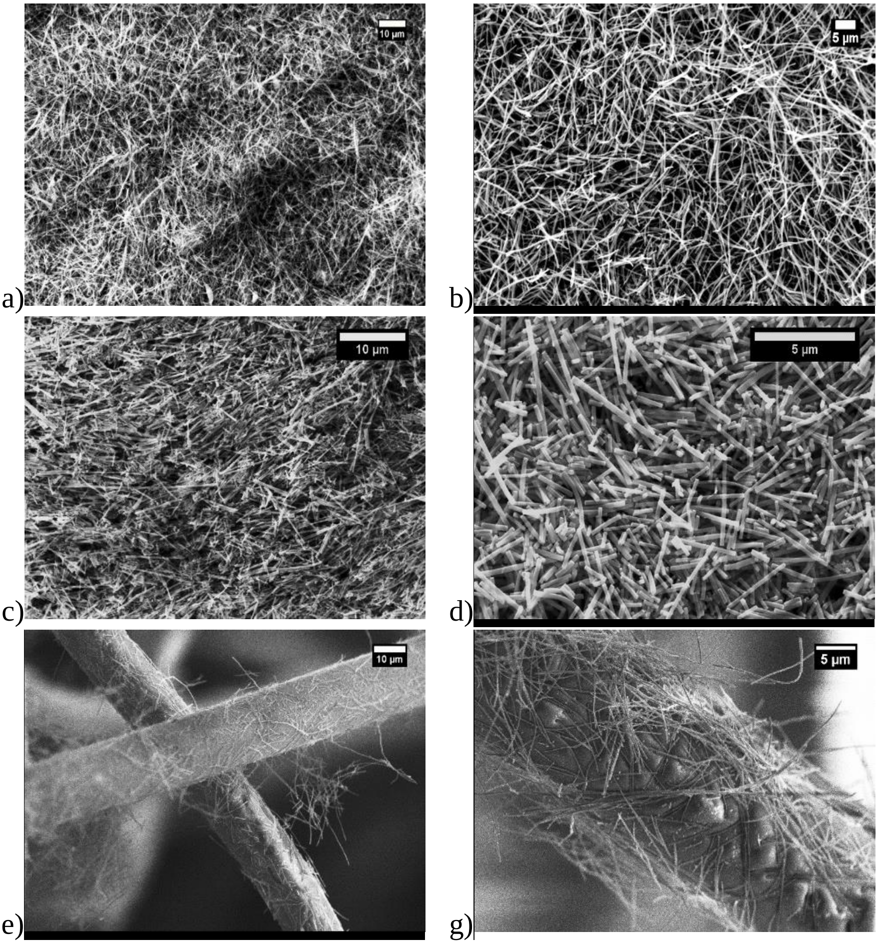

Figure 17. (a), (b) surface deposited TiO_2 nanofibres (PAN-NF-G); (c), (d) tape casted TiO_2 short nanofibres (PVP-NF-SS); (d), (f) spray coated TiO_2 nanofibres on polymeric microfibres (PVP-NF-PA12)

Short-nanofibres randomly covered a microfibre, meanwhile longer nanofibres tended to just partly cling to the surface of a microfibre, forming a ragged surface.

Relatively high porosity and low packing density of microfibres allowed shortened nanofibres to attach not only to upper microfibers, but to deeper layers as well. Generally, such spray coating provides a very high effective surface area of the catalyst whilst combining microfibres with short-nanofibres. No loss of TiO_2 nanofibres was observed after the spraying process. Moreover, the even amalgamation of nanofibres throughout the length of microfibre provided a good interaction (in terms of adhesion) between both materials.

The catalysts surface density in case of stainless steel and PA12 supports differed by an order of magnitude (1 mg/cm^2 and 0.06 mg/cm^2, respectively, Figure 18). **Appendix A. 6.** Shows a composite of short nanofibre on microfibrous PA12 catalyst with different densities (0.4–0.8 mg/cm^2). In the case of low density, nanofibres of TiO_2 are randomly distributed over the microfibre of PA12 and covers just a small part of the supporting polymer microfibres. Meanwhile, the increased amount of nanofibrous TiO_2 started to form overfull layers, which means that the increase in the surface area is also limited by the surface of microfibres. Moreover, the removal of nanofirbes was observed. Certainly, an increase in the amount of the photocatalyst improves the rate of the photoreaction because the number of active sites is increased on the photocatalyst surface. However, it is also known that the reaction rate increases until a certain limit amount of the catalyst corresponding to the total absorption of various species on the active sites of the catalyst is achieved. Above this limit amount, the rate of the photoreaction can even decrease (16). Therefore, the optimal density of the nanofirbous TiO_2 in the case of composite photocatalyst was determined to be up to 0.06 mg/cm^2 in this research.

Figure 18 summarizes the main morphological features of synthesized fibrous and Aeroxide P25 photocatalytic layers of TiO_2. The morphological parameters of Aeroxide P25 are mostly at a smaller level compared to nanofibrous layers of TiO_2. It was not possible, however, to measure the surface roughness of a composite fibre-on-fibre photocatalyst layer with the morphology analyzing techniques used in this work, because of specific architecture of the composite. Nevertheless, it could be concluded that the surface roughness strongly influenced the sorption capability of deposited layers. Meanwhile, higher density is not advantageous for this kind of research.

	BET, m^2/g	Density, mg/cm^2	R_a, µm	Pore size, nm (median)±SE[**]	Sorption capacity, mg/mg
P25	35-50[*]	0.12±0.02	0.29±0.19	n.a.	0.002±0.001
Nfa	58.2	0.09±0.02	1.31±0.15	14.5 (13.6)±2.8	0.03±0.001
Nfmix	36.3	0.16±0.01	1.31±0.15	20.9 (16.3)±4.6	0.01±0.001
PA12	83.9[***]	0.06±0.01	n.a.	8.4 (4.4)±1.3[***]	0.05±0.002
NF	83.9	1.00±0.03	0.88±0.07	8.4 (4.4)±1.3	0.002±0.001
[*]data from manufacturer, [**]data distribution presented as standard error (SE) because of large skewedness of the data, [***]nanofibres value					

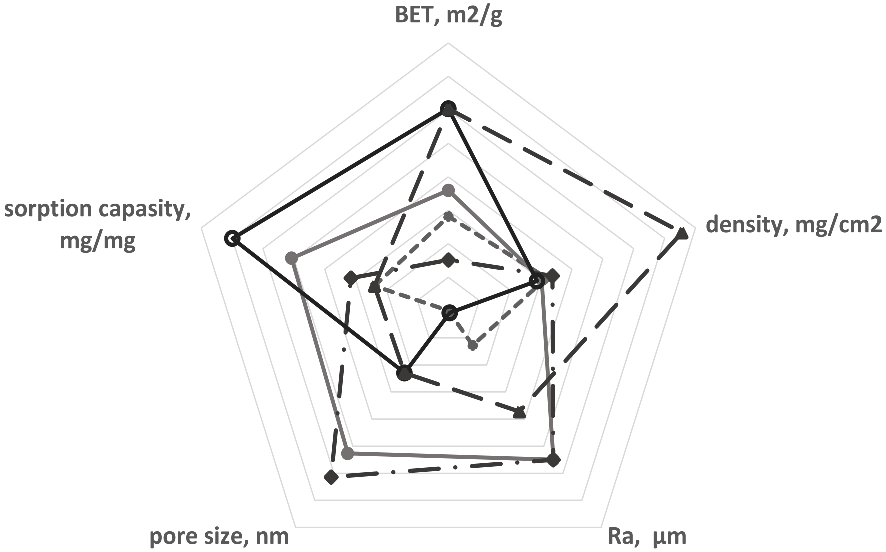

Figure 18. Summary of physical properties of synthesized TiO_2 nanofibres including BET surface area, average surface roughness, pore size, density and sorption capacity of photocatalysts on different supports. Data are given in mean values ±SD unless otherwise specified

V. Photochemical Properties

Measurement of UV-vis diffuse reflectance is a standard technique in the determination of the absorption properties of materials. This information can be used to estimate the band-gap energy of the SC as follows:

$$\alpha \cdot h\nu = (h\nu - E_g)^2 \qquad \textbf{Eq.20}$$

where α is the absorption coefficient, $h\nu$ is the discrete photon energy (where $\nu = \frac{c}{\lambda}$, c is the speed of light ($2.998 \cdot 10^8$ $m \cdot s^{-1}$), λ is the wavelength of light (nm)), and h is Planck’s constant ($6.626 \cdot 10^{-34}$ J·s).

UV visible diffuse reflectance spectra of the TiO_2 nanostructures are shown in Figure 19 (left). Over the range of 350–400 nm an abrupt increase in the reflectance is observed which indicates the onset of the fundamental absorption edge. This is typical of titania and provides a clear indication of successful synthesis of the TiO_2 nanofibres. Based on reflectance spectra, the absorption edge was determined. Using this absorption edge, the band gaps were estimated to be approx. 3.07 eV, 3.02 eV and 2.97 eV for Aeroxide P25, PVP-NF and PAN-NF respectively, which was very close to the reported value of anatase TiO_2. Slight differences in band-gap of nanofibres can be ascribed to the changes in their electronic structures during the formation of 1D dimension and the smallest 2.97 eV for PAN-NF could be due to the mixed-phase effects of semiconductors which was achieved with higher calcinations temperatures.

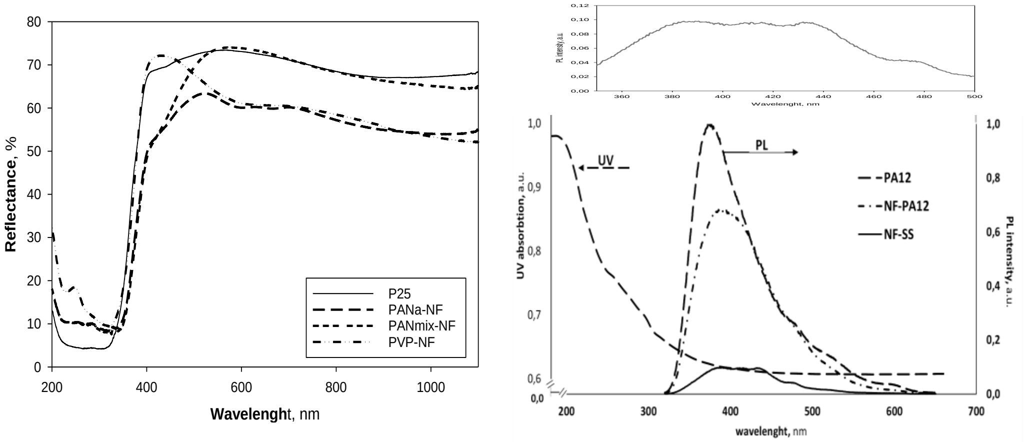

Figure 19. UV-vis diffuse reflectance spectra (left) and normalized PL spectra of various TiO_2 composite fibres and UV-vis absorption of PA12 (right)

Meanwhile, PA12 demonstrated one sharp UV absorption peak at ~180 nm (Figure 19, right), which in literature is attributed to the π–π^* orbital transition in C=O bond (160).

Figure 19 (right) presents photoluminescence (PL) spectra of TiO_2 nanofibres. The PL spectra of TiO_2 nanofibres showed emission peaks at 390 nm, one violet emission peak at 416 nm, two blue emission peaks at 435 nm and 476 nm, and one green emission peak at 523 nm (shown as inset of the figure). The violet emission peak can be ascribed to self-trapped excitons localized on the surface of the material, while PL bands at the longer wavelengths side can be attributed to the defect centers associated with oxygen vacancies (60). The PL spectra of PA12 and composite fibre-on-fibre demonstrated one intense peak each at 378 nm and 398 nm, respectively. However, the polyamide support revealed stronger fluorescence emission in comparison to the composite fibre-on-fibre structure that confirms the existence of TiO_2 structures. The analysis of PL emission has been used to investigate the fate of electron-hole pairs in catalysts. PL emission is known to result from the recombination process of excited electrons and holes, thus a lower PL intensity may indicate a lower recombination rate of electron-hole pairs under UV irradiation (60). The reduced intensity of PL spectra of the composite fibre-on-fibre structure may be interpreted as a delayed recombination of photogenerated charge carriers.

3.1.2. Photocatalytic Activity of Fibrous TiO_2

The photocatalytic performance of a synthesized catalyst was researched in three steps: sorption, photolysis, and photocatalysis. The latter was conducted after reaching equilibrium conditions with sorption and photolysis in order to ensure the evaluation of pollutant concentration decrease purely due to photocatalytic degradation of model compounds.

3.1.3.1. Aqueous Medium

Photocatalytic decolorization of an organic dye such as Methylene Blue is widely known and often used to test photocatalysts (Table 8). Therefore, it was selected for the purpose of this work as well.

I. Sorption Capacity

The sorptive capacity of the catalytic surface has been indicated to play an important role in photocatalytic reactions since the adsorption of contaminants on the surface of a catalyst has been shown as a major parameter influencing the photocatalytic decomposition of chemical species.

In order to determine sorptive capacities just for TiO_2 only materials, all used supports were also exanimated uncovered within the same experimental conditions. No changes have been monitored with a glass plate or stainless-steel support. Only polymer microfibre has shown very low adsorbing capabilities for MB (<2%). In fact, the polyamide is known to have hydrophobic nature. Overall, all catalytic layers demonstrated low sorption (<4%) of Methylene Blue in aqueous environment. Low adsorption of pollutants is common in aqueous photocatalytic systems due to saturation of pores with water. At a range of neutral pH, the surface charge of TiO_2 is also neutral, thus the interaction with polar compounds is minimal. On the other hand, the surface of titania becomes negatively charged at higher pH (Eq. (15)) and adsorption of MB would be induced because of cationic dye. However, in the case of oxalic acid, the sorption reaches from 0.7% for Aeroxide P25 to approx. 7% for fibrous TiO_2 samples.

Aeroxide P25 powder demonstrated a relatively low ability (Table 13) to sorb organic compounds from the water solution (it has been estimated that the adsorption equilibrium constant for adsorption of MB on P25-type TiO_2 is $6.65 \cdot 10^{-3}$ l/µmol (161)) and basically did not depend on the coating method. Meanwhile, surface-deposited nanofibres had some peculiarities which perceptibly depended on the coating technique and crystalline composition.

First of all, samples that were synthesized to contain both crystalline phases of TiO_2 demonstrated lower sorption capacity than fibres containing a purely anatase phase for both model pollutants in an aqueous medium (Table 13). These differences are statistically significant ($p \ll 0.05$ based on the Student's *t*-test). This is because the adsorptive affinity of the anatase phase is known to be higher for organic compounds (162).

Secondly, the surface-mounted TiO_2 nanofibres, unlike Aeroxide P25 powder, prepared by solvent evaporation, tape-casting and spray-coating methods also showed different sorbtive abilities. Table 13 and Figure 18 clearly show that sorption increases with decreasing density of the catalytic layer. This just proves that generally sorptive abilities depend on the surface porosity and roughness of the fibrous layer that provides a higher volume of macro pores between fibres. The morphologies and differences of the prepared photocatalytic layers are given in Figure 16, 17**,** and 18. The novel PA12 and TiO_2 composite layer demonstrated the highest sorption capacity for MB; lightly packed TiO_2 fibres, prepared by the solvent evaporation method, had the second best result, and tape casted nanofibrous TiO_2 showed a similar outcome as Aeroxide P25 powder by means of MB sorption in aqueous environment. The amorphous and structured thin film TiO_2 samples demonstrated also very small sorptive abilities (<2%) independently on the structure patterns.

Furthermore, some increase in sorption capacity may be associated with remaining elemental carbon as well. In the case of PAN, it has been shown to form carbon nanotube structures during the calcination of nanofibres in temperatures above 1000°C (163). However, the formation of these structures was not expected in the applied temperature ranges and further effects of the potentially remaining carbon to catalytic performance of the layer were not investigated.

Finally, the adsorption capabilities of catalytic layers were arranged in the following order: PVP-NF-PA12 > PAN-NFa-G > PAN-NFmix-G > PVP-NF-SS and Aeroxide P25 as well as thin films of TiO_2.

However, the catalytic activity of Aeroxide P25 powder appeared higher than of nanofibres (as presented in the next section), even at lower sorption capacity. This indicates that other factors (such as combination of an optimal crystallite size and phase distribution) are more important in determining final photocatalytic activity of a layer. Moreover, the process of photocatalysis relies on the photo activation of the catalysts by photon radiation, which is only available at the very surface of the layer. Thus, a high porosity and sorptive capacity may not be as beneficial as in other types of catalysis.

II. Photolysis

UV-C radiation without a catalyst was capable to decompose only one third of the tested substances (28% for MB and 35% for OA, Figure 20) during 180 min period due to direct photolysis. These results are in consist with many other research (Table 8). There was no statistically significant difference ($p>0.05$ based on Student's *t*-test) between measurements results of UV light alone and all types of uncovered supports with the illumination of UV light.

III. Photocatalytic Performance

The catalytic performance was assessed as the function of concentration decrease during the time, which has followed two mechanisms for two model pollutants used in the experiments. The measurements of light absorbance of the reaction solution during the experiment period showed only the destruction of the primary compound. Thus, the decomposition of MB followed an exponential decay function (Eq. (21)):

$$C_i = C_0 \cdot e^{-k \cdot t}; \qquad \textbf{Eq.21}$$

Meanwhile, the TOC measurements used as an indicator of the OA decomposition took into account the formation of decomposition by-products and introduced the delay in the beginning of the decomposition process (162). Therefore, the decomposition of OA was approximated by the sigmoidal decay curve (Eq. (22)):

$$C_i = \frac{C_0}{1+e^{\frac{(t-t_0)}{k}}} \qquad \textbf{Eq.22}$$

where C_0 – initial MB concentration (mg/L), C_i – concentration at the time measured (mg/L), k – a decay constant (min^{-1}), t – time (min).

It is known that the initial step of photo-oxidation of MB is the cleavage of the bonds in $C–S^+=C$ functional group, leading to the formation of sulfoxides, carbon dioxide, nitrate, sulfate and ammonium as reaction products of the complete oxidation. In this work, the mineralization process only of oxalic acid was studied.

Recently, Lin et al. (164) proposed a photocatalytic degradation pathway of MB that is generally driven by attacks of $OH^{\bullet}$ and attaches itself to a model pollutant molecule:

$$\begin{tikzcd}
 & & C_8H_{11}N_2SO_3^- \arrow[r] & C_6H_4NO_2SO_3^- \arrow[r] & C_6H_6SO_3 & \\
C_{16}H_{18}N_3S+ \arrow[r] & C_{16}H_{18}N_3SO \arrow[ur] \arrow[dr] & & & & NO_3^- + SO_4^{2-} + R + H^+ \\
 & & C_8H_{12}N_2 \arrow[r] & C_8H_{11}NO \arrow[r] & C_6H_6O_2 &
\end{tikzcd} \qquad \textbf{Eq.23}$$

where R is ring opened, small organic molecules that eventually are oxidized to CO_2 and H_2O.

Meanwhile, the overall photocatalytic oxidation of OA can be summarized (165):

$$HC_2O_4^- + ½O_2 \xrightarrow{\text{hv, TiO}_2} 2CO_2 + OH^- \qquad \textbf{Eq.24}$$

$$H_2C_2O_4 + ½O_2 \xrightarrow{\text{hv, TiO}_2} 2CO_2 + H_2O \qquad \textbf{Eq.25}$$

$$C_2O_4^{2-} + ½O_2 + H_2O \xrightarrow{\text{hv, TiO}_2} 2CO_2 + 2OH^- \qquad \textbf{Eq.26}$$

➢ *The first set of synthesis experiments with PAN and TTIP*. The results of MB photodecolonization with samples on glass substrate are shown in Figure 20 as well as the obtained decay curves of OA that served for the calculation of below presented degradation periods.

Aeroxide P25 has been well documented and has been established as a benchmark for TiO_2 based catalysts. The decomposition of 50% MB has been achieved during 80 min period with the decay rate of $8.8 \cdot 10^{-3}$ min^{-1}, while the same amount of oxalic acid was completed during the period of around 30 min (with the initial concentration decay rate of $17 \cdot 10^{-3}$ min^{-1}).

The synthesized nanofibrous layer of TiO_2 proved to be a very efficient photocatalyst, although slightly less efficient then the Aeroxide P25 layer. The decomposition of MB and OA of 50% with anatase phase nanofibres has been achieved during 90 min and 70 min period, respectively (with the initial concentration decay rate of $7.3 \cdot 10^{-3}$ min^{-1} for MB and $7 \cdot 10^{-3}$ min^{-1} for OA). Meanwhile, nanofibres of mixture of rutile and anatase phases have shown photocatalytic activity almost a third poorer than commercial TiO_2 powders for decolorization of MB and almost two third for OA. The photocatalytic decolorization efficiencies of the tested catalyst samples were arranged in the following order: Aeroxide P25 > PAN-NFa-G > PAN- NFmix- G.

All samples were able to fully decompose OA, just in different time, and were arranged in the same order.

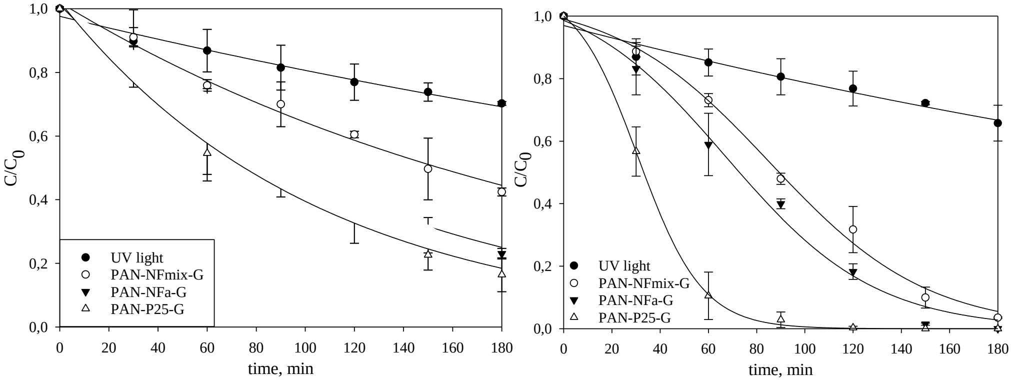

Figure 20. Decomposition kinetics of methylene blue (left) and oxalic acid (right) presented as a ratio of final concertation for the compound (C) vs. the initial concentration (C_0) using UV-activated surface deposited commercial TiO_2 nanopowder (Aeroxide P25), TiO_2 nanofibres consisting of mixture of rutile and anatase phases (PAN-NFmix-G) and purely anatase (PAN-NFa-G) as well as UV radiation without a catalyst; error bars represent standard deviation of three multiples

Although the mixed form of rutile and anatase has been shown to result in an enhanced photocatalytic ability, such as in case of Aeroxide P25 powder, the presence of both crystal phases in nanofibres did not follow this trend in the present research. Similar results were obtained by Choi and colleagues (97) who monitored the degradation of Ranitidine with the mixed phase TiO_2 nanofibres supported on glass. Such observations may be related with the size of crystallites and not only with the phase distribution. The lifetime of photoexcited e^-–h^+ pairs is prolonged in larger crystallites because they migrate a longer distance indicating that such particles have a faster electron transfer rate from the surface to the absorbed intermediates (163). The migration of excited electrons may be also obstructed by the impurities in crystallites, namely the remains of carbon after the calcination step.

➢ *The second set of synthesis experiments with PVP and TiBu.* Kinetic curves of the photocatalytic decolorization of MB are depicted in Figure 21. The color breakdown followed a linear decay pattern in all cases during the tested timeframe (120 min). The photocatalytic decolorization efficiencies of the tested catalyst samples were arranged in the following order:

NF-PA12 > Aeroxide P25 > NF-SS.

Once again, Aeroxide P25 has demonstrated a good photocatalytic performance; 50% of MB decolorization achieved in around 90 min with the decay rate of $6.7 \cdot 10^{-3}$ min^{-1}. Nevertheless, at this point advantages of electrospun polymeric fibres as support for semiconductor nanostructures for photocatalysis have been revealed. As it was discussed in previous chapters, polymer/TiO_2 composites have demonstrated an increase in the photocatalytic activity.

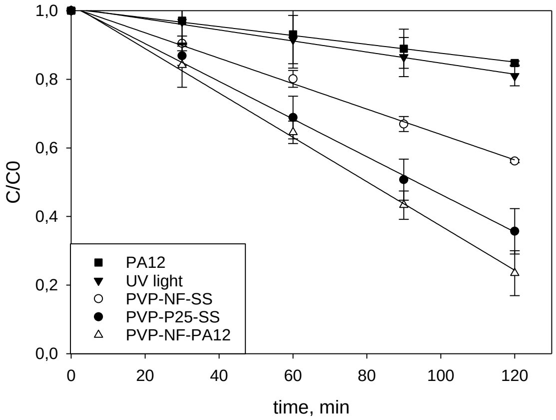

Figure 21. Decolorization kinetics of Methylene Blue solution in water. Results are presented as a ratio of the final concertation for the compound (C) vs. the initial concentration (C_0) using UV-activated TiO_2 nanofibres on a polymeric support (PVP-NF-PA12), commercial TiO_2 powder (PVP-P25-SS) and TiO_2 nanofibres on a stainless steel support (PVP-NF-SS) as well as UV radiation (UV light) and a polymeric support (PA12) without a catalyst; error bars represent standard deviation of three multiples

It has to be emphasized that many authors have been introducing TiO_2 nanoparticles into the polymer nanofibres until now and simultaneously indicated an agglomeration of nanoparticles as the main disadvantage causing nozzle blockage, bead formation during the spinning process. Thus, this novel introduction of TiO_2 nanostructures (not only 0D dimensionality) on fibres has not been reported yet.

Higher photocatalytic activity of the fibre-on-fibre catalyst compared against other catalytic layers indicates advantages of composite fibres (50% of MB decolorization achieved in 80 min with the decay rate of $10.4 \cdot 10^{-3}$ min^{-1}). A higher surface area of the polymer fibre membrane leads to a more efficient light interaction with the TiO_2 nanofibres.

Table 13 and Figure 22 show the main parameters of all synthesized photocatalytic layers and their photoefficiency in aqueous media (presented as reaction rates), respectively. As can be seen from these results and the ones given in Figure 18, the morphology of the synthesized catalytic layer had most of the influence on the kinetics and the final photoefficiency.

The PA12 microfibre support was determined as opaque, i.e. non-transmitting UV/V light (**Appendix A. 4.**). This may indicate that a polymer absorbs some parts of short wavelength radiation and scatters the rest of it, enabling more light to reach deeper layers and activate the dispersed catalyst. Moreover, the exited π orbital of PA12 may act as e^- donor and the charge separation can be enhanced, electrons in TiO_2 (CB) react with water and oxygen to produce reactive species that initiate the chain reaction for degradation as similarly observed by Gu et al. (160).

Table 13. Photocatalytic characterization of synthesized TiO_2 nanofibres and Aeroxide P25 powders, including sorption capacities and photocatalytic efficiencies

Sample	Sorption capacity, mg/mg		Sorption capacity, %	Decomposition time of 50% of pollutant, min		Final photodecomposition efficiency, %	
	MB	OA	Toluene	MB	OA	MB*	Toluene**
PAN-P25-G	0.002±0.001	0.13±0.11	-	80	33	71±6.3	-
PVP-P25-SS	0.005±0.002	-	19±3.8	94	-	64±5.9	85±4.3/82±6.4/78±10.3
PAN-NFa-G	0.03±0.001	1.23±0.32	-	90	70	56±0.2	-
PAN-NFmix-G	0.01±0.001	0.47±0.37	-	155	85	47±7.3	-
PVP-NF-SS	0.002±0.001	-	25±3.3	135	-	44±2.2	74±8.9/60±10.2/48±7.2
PVP-NF-PA12	0.05±0.002	-	32±2.3	80	-	77±6.4	87±0.9/59±4.2/49±5.4

*after 120min;

**efficiencies with increased air velocity 0.1/0.2/0.3 m/s

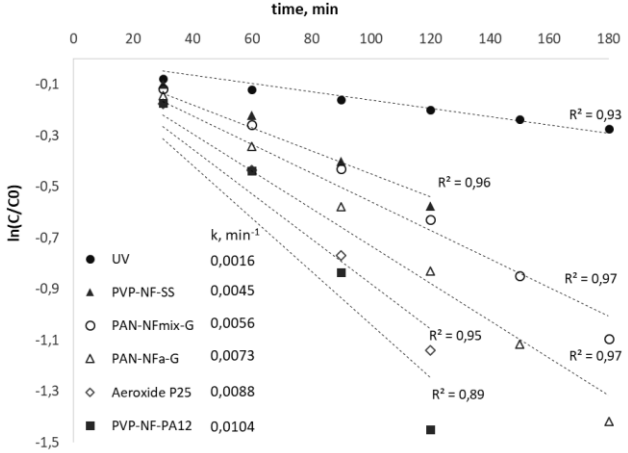

Figure 22. Photoreaction decay constants (min^{-1}) for all fibrous samples of TiO_2 (PVP-NF-SS, PAN-NFmix-G, PAN-NFa-G, PVP-NF-PA12), Aeroxide P25 layer as well as UV light alone

3.1.3.2. Air medium

The French Standardization Association (ANFOR) has recommended toluene as a model pollutant for PCO evaluation (152). Furthermore, toluene has been frequently identified in both indoor and outdoor air. Consequently, it is one of the most investigated model pollutants in the PCO studies and was chosen in this research.

On the contrary to the testing the supported catalyst in the liquid medium where the test was conducted in a batch-type reactor, the airborne pollutant decomposition was tested in the continuous flow annular reactor. Nevertheless, at first the sorption and photolysis processes were carried out and only then the photocatalytic process was initiated.

The photoefficiency of decomposition of toluene was tested just with PVP and TiBu based on a fibrous photocatalyst.

I. Sorption Capacity

Aeroxide P25 powder and nanofibres on the SS support demonstrated similar sorption capability (19±3.8% and 25±3.3% on average of the initial concentration, respectively). Nanofibres on PA12 support showed the highest sorption of toluene of all tested layers, i.e. 32±2.3% on average of initial concentration. Due to the continuous flow, the sorption was a function of the air flow velocity or the residence time.

II. Photolysis

The UV light alone had no effect on the decomposition of toluene vapors. Such effect was registered in the previous studies (22). Evidently, lower air flow rates together with longer residence times of the target pollutant are needed in order to increase the direct photolysis of organic compounds with higher molecular mass.

III. Photocatalytic Performance

The equilibrium efficiencies of the toluene degradation as a function of air flow velocity are presented in Figure 23. Similarly, to the waterborne experiments with fibrous TiO_2 photocatalysts, the efficiency of toluene degradation was arranged in the following order: NF-PA12 (87±0.9%) > P25-SS (85±4.3%) > NF-SS (74±8.9%) in case of liner velocity at 0.1 m/s. Once again, nanofibrous inorganic TiO_2 catalyst on microfibrous polymeric support demonstrated the best results of all tested catalytic layers. This again is related to a high surface and available contact area of the hybrid catalyst. An efficient operation of a photocatalytic oxidation system in the gas phase is not only a function of the amount of UV irradiation. A high probability of contact between the photocatalyst and reactants has been indicated as an important factor earlier and was confirmed in this study. A rough surface results in the formation of wake and eddy flow, thus significantly increasing the probability of the contact between reactants and the photocatalyst. Therefore, the capability of short-nanofibres to form a branchy structure around the surface of a microfibre is advantageous. The porous structure of a microfibre layer allows organic molecules to reach the surface of the catalyst that is evenly distributed around the microfibre (Figure 17 (e), (g)).

As already mentioned above, the catalysts surface density in case of stainless steel and PA12 supports differed in the order of magnitude. This implies that good photocatalytic activity can be achieved with a smaller amount of catalyst mounted on a highly porous support that provides a large active surface. Such design is also favorable in the environmental standpoint as the amounts of materials used for the manufacturing of the catalyst and the waste of spent catalyst are minimized.

However, the photoactivity decrease was observed when a gaseous pollutant was introduced with higher linear velocities for all catalytic layers. This is related with competition between the residence time of a pollutant and probability of contact. The obtained results were in accordance with previously reported trends. It has been observed that the relationship between the photoreaction efficiency and the residence time could be approximated well by an exponential function (33, 166). The highest loss in photoactivity was determined for nanofibrous catalysts. The photocatalytic efficiency reduced by a quarter when a pollutant was introduced with 0.2 m/s linear velocity and almost 40% with 0.3 m/s linear velocity. The efficiency of toluene degradation with higher liner velocities was arranged in the following order: P25-SS > NF-SS; NF-PA12. These results indicate that the photocatalytic decomposition of toluene having fibrous structure of TiO_2 requires longer time than the residence time and that pollutants cannot fully participate in reactions. Obviously, fibrous structure of a catalyst cannot cope with a suddenly increasing load of the pollutant. The same effect was observed by other authors who were using nanofibres for decomposition of gaseous pollutants. Chun et al. (167) and Lee et al. (166) reported 40% to 60% decrease in photocatalytic activity of TiO_2 nanofibres with increased flow rates from 1 to 4 L/min. Authors concluded that the results were influenced by the lack of contact time between the catalyst and pollutant. It is can be concluded that nature of VOCs has no significant effect on the mineralization.

Moreover, according to the Ohtani model (168), high photocatalytic activity of TiO_2 can be achieved with the catalyst having a large specific surface area and a high degree of particle crystallinity in order to have an effective adsorption of a target compound and to slow down the recombination rate of photogenerated charge carriers respectively. These requirements can only be partially satisfied at moderate temperatures (≤500°C) as the calcination at higher temperatures results in better crystallinity but lower specific surface area of photocatalysts.

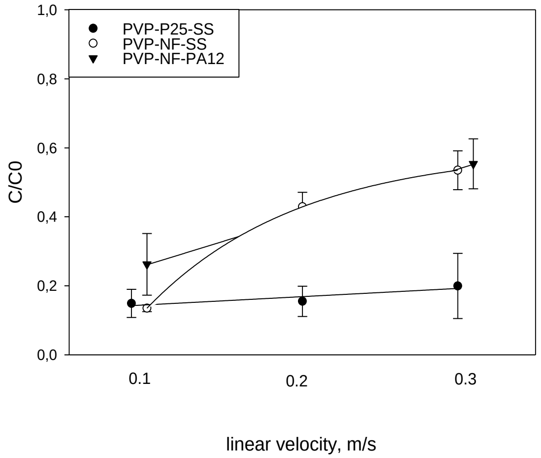

Figure 23. Decomposition of gaseous toluene. Results are presented as a ratio of final concertation for the compound (C) vs. the initial concentration (C_0) using UV-activated TiO_2 nanofibres on a polymeric support (PVP-NF-PA12), commercial TiO_2 powder on a stainless steel support (PVP-P25-SS), TiO_2 nanofibres on a stainless steel support (PVP-NF-SS); error bars represent standard deviation of three multiples

By-products of the mineralization process of toluene were not studied in this research. The formation of benzaldehyde, acetaldehyde, acetone, benzoic acid, small concentrations of benzyl alcohol, and some other intermediates during the gas-phase photocatalytic oxidation of toluene on TiO_2 were evidenced in the previous studies (27, 152, 169, 170). Generally, it is obvious that the generation of by-products, as a result of incomplete photo-oxidation, is related to the nature of the target VOC. For example, according to Zhong et al. (27) the amount of acetaldehyde produced from the PCO of ethanol was 10 times higher than its amount produced from the PCO of other VOCs.

Boyjoo and colleagues (152) reported some summarized essential steps of the proposed mechanisms of the photodegradation processes of gaseous toluene. As the general photoexitation starts with Eq. (3–5) and Eq. (7–9) at the first stage – the generation of oxidants, the following stage – the degradation and mineralization of toluene can be described as follows:

$OH^{\bullet} + C_6H_5CH_{3,ads} \rightarrow H_2O + C_6H_5CH_2^{\bullet}$ **Eq.27**

$C_6H_5CH_2^{\bullet} + O_{2,ads} \rightarrow C_6H_5CH_2OO^{\bullet}$ **Eq.28**

$C_6H_5CH_2OO^{\bullet} + e^{-}_{trap} \rightarrow C_6H_5CH_2O_{ads} + OH^{-}$ **Eq.29**

$C_6H_5CH_2O_{ads} + OH^{\bullet} \rightarrow C_6H_5CO^{\bullet} + H_2O$ **Eq.30**

$C_6H_5CO + OH^{\bullet} \rightarrow C_6H_5CH_2OOO^{\bullet}$ **Eq.31**

$C_6H_5CH_2OOO^{\bullet} + C_6H_5CO_{ads} \rightarrow 2C_6H_5COOH_{ads}$ **Eq.32**

$C_6H_5COOH_{ads} \rightarrow C_6H_6 + CO_2$ **Eq.33**

Eq. (33) can be continued as Eq. (2) and Eq. (1), in short:

$C_6H_5CO_{ads}$ / $C_6H_5COOH_{ads}$ + $OH^{\bullet}/O_{2,ads} \rightarrow CO_2 + H_2O$ **Eq.34**

Three parameters have to be taken into account to completely characterize photocatalytic performances in air media:

(*) the degradation of primary VOCs,

(*) the formation of reaction intermediates,

(*) the mineralization ratio.

Mineralization describes the purification efficiency of the overall process by the ratio between evolved CO_2 concentration during the process and theoretically possible CO_2 concentration that depends on the input of the primary compound (171). The background level of CO_2 in ambient air is 405 ppm (178). This is much higher than the expected formation of CO_2 due to the photocatalytic mineralization of low levels VOCs (for example, the highest total concentration of CO_2 from the experiments described in this work would be 7 ppm). For this reason, mineralization rates of low level VOCs are reported small, which is related with complicated measuring conditions. For example, Debono and colleagues (171) used *Pressure Swing Adsorption* system to remove background CO_2 from the air supplied to the photoreactor. In their experiment the sigmoid profile of evolved CO_2 from toluene photocatalytic oxidation was determined and was related to the evolution of adsorbed and degraded reaction intermediates along the reaction advancement. Primary reaction intermediates formed at the beginning of toluene oxidation are still aromatic compounds (Eq. (23–29)), and the degradation of these compounds is slow due to aromatic ring, whereas secondary reaction intermediates are aliphatic and more easily mineralized later in reactions (Eq. (1)).

3.1.3. Chapter Summary

The synthesis of nanofibres from the organic precursors has proved to be an efficient method for the development of fibrous TiO_2 leading to an equally dispersed TiO_2 crystals. In this respect, it is superior to the direct mixing of TiO_2 nanoparticles in the initial electrospinning solution, which may lead to aggregation of TiO_2 particles. Since PAN is demanding in the matter of working conditions, material consumption and needs more aggressive solvent, the PVP serves as an excellent alternative.

Annealing temperature is being considered as the main parameter to control the crystallization degree of titania. The matrix that contains TiO_2 precursor demonstrated to influence the temperature when crystal phases of TiO_2 are achieved. Having different matrixes, the control of the size of crystallites is also possible. The formation of crystalline phase appears at lower temperatures with PVP and TiBu than with PAN and TTIP (possibly because PAN is a semi-crystalline polymer and its chains are better oriented and more densely packed within an electrospun fibre) both leaving some residual of carbon as the residual of the polymer matrix. Nevertheless, calcined fibres were prevailingly composited of evenly distributed TiO_2 particles. Consequently, the optimum calcination temperatures have been selected allowing to adjust the phases and crystallite sizes of TiO_2, which is a moderate level, i.e. 500°C (Figure 10).

The removal of the polymeric matrix reduced fiber diameters few times with both polymeric matrixes. However, the PVP proved to produce fibres with smaller and more uniformly distributed diameters (Figure 13, Table 12). Consequently, a relatively high specific surface area (83.9 g/m^3) of synthesized TiO_2 fibres was obtained compared with most often reported solid TiO_2 nanofibres (30 g/m^3, Table 8). Moreover, the N_2 adsorption-desorption isotherm indicated that the mesoporous material was achieved (Figure 15).

All formed photocatalytic layers demonstrated good and resembling photochemical properties to commercially available TiO_2 powder.

Until now, two main strategies have been applied for immobilization of TiO_2 nanoforms, i.e. coating TiO_2 on supporting materials by the sol-gel process and fabricating TiO_2 as a film (152). Several coating techniques were applied to mount nanofibrous TiO_2 on different supports for applications in various environmental media in this research, namely on glass, stainless steel and microfibrous polymer. Furthermore, the attempt to synthesize nanofibres on microfibers using polymer as a support for a photocatalyst has not been reported so far. The result showed that TiO_2 nanofibres tended to form a compact but fenestrate layer on glass and SS supports, while PA12 proved to be an excellent choice with an open and accessible surface for photocatalytic applications of nanofibrus TiO_2 in systems of environmental catalysis.

The anatase phase TiO_2 nanofibres showed the best photoefficiency in both tested environmental media. The morphology of synthesized layer proved to be an important parameter in means of the material usage and final efficiency of the photocatalytic layer. The sorption ability is an important feature of a photocatalyst since it might increase the residence time of the target pollutant and contact probability with the surface of the catalyst. The sorption capacities of the synthesized photocatalytic layers of TiO_2 were best represented by the experiments in aqueous media. Sorption capacities depended not only on the structure and geometry of TiO_2, but also strongly on the coating technique and the derived density. The highest sorption abilities had layers with smaller surface density, but higher specific surface area and surface roughness (Figure 18). Therefore, nanofibrous TiO_2 with PA12 support demonstrated the highest sorption abilities. Differences in sorption abilities for different TiO_2 photocatalytic layers in the air medium were not that explicit because of the different level in concentrations of the pollutant, affinity of the catalyst surface for target molecules, residence time of the pollutant that depends on the airflow, etc.

The highest catalytic activity among the tested catalyst morphologies has been achieved with inorganic nanofibrous TiO_2 on a polymeric (PA12) support for pollutant decomposition in simulated aqueous and airborne environment. Improved photocatalytic properties mainly were attributed to a high surface area, light absorption, and branchy distribution of short nanofibres over a microporous support surface.

The microfibrous polymeric support with nanostructured TiO_2 demonstrated good photocatalytic capabilities for gaseous pollutant decomposition with lower linear velocity. Moreover, the low density but high available surface area of the nanofibrous TiO_2 on PA12 support implies that good photocatalytic activity can be achieved with a smaller amount of a catalyst. Such design is also favorable in the environmental standpoint as of materials usage and the waste generation.

3.2. Results of Thin Film Photocatalysts

3.2.1. Structural Characterization of Thin Films Photocatalysts

I. Crystallinity.

Since no additional heating was used during the PVD, deposited layers were amorphous TiO_2 as there were no sharp peaks in XRD spectra as shown in Figure 24.

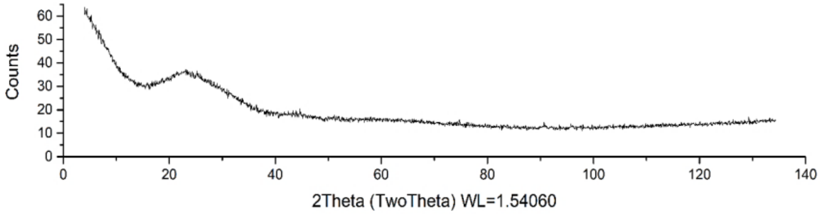

Figure 24. XRD spectra of thin film TiO2 layer synthesized by PVD technique

The amorphous phase was also present in all synthesized nanofibrous TiO_2 samples and commercial TiO_2 powders (up to 10 %, as stated by the producer), but was not assessed quantitatively.

II. Morphology

Five different samples of thin film TiO_2 with different modification of support (different spacing and patterns) were prepared. The description of thin films is given in Table 12 and Table 14.

The surface morphology of all samples was analyzed by SEM, optical microscopy, and AFM. Figure 25 displays SEM pictures of structured samples of synthesized and tested thin films of TiO_2. SEM analysis showed that there is a clear difference between non-structured thin film TiO_2 and structured samples. A regular array for line-patterned structures and uniform pattern of grid-patterned were formed during the interference lithography process. Thicknesses of the photoresist and titania layers were approx. 4.6 μm and 100 nm, respectively.

The size of spacing was confirmed by SEM, AFM, and optical microscopy and is given in Table 12. The results of optical microscopy are given in **Appendix A. 5.**

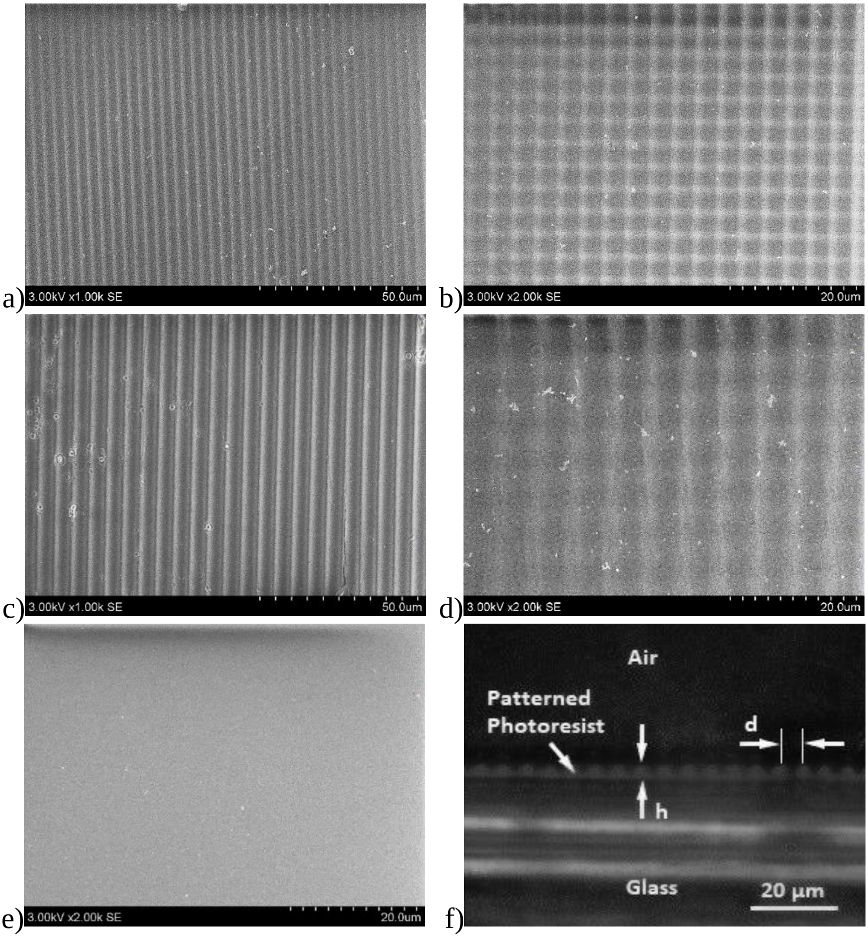

Figure 25. SEM pictures of formed structured thin films TiO_2: (a) line patterned structure with 3.4 μm period, (b) grid patterned structure with 3.6 μm period, (c) line patterned structure with 5.3 μm period, (d) grid patterned structure with 5.9 μm period; (e) SEM picture of non-structured thin film of TiO_2; (f) cross-section of (c) made with the optical microscope, period marked as *d*, *L* represents the thickness of a photoresist layer

III. Surface Roughness

As can be seen in Figure 26, the sinus grating shape can be identified for the line patterned samples, while the grid pattered samples show the shape more of a lattice with regular depth. The roughness of the thin film TiO_2 samples were also identified with AFM and were relatively small, i.e. 0.2–0.4 µm (Table 14). This surface layer parameter is similar to the one measured for tape-casted and surface deposited layers of Aeroxide P25 (Figure 18).

The relatively small surface roughness also indicates that lithography and PVD processes were felicitous and synthesized layers were smooth and identical with minimum spoilage.

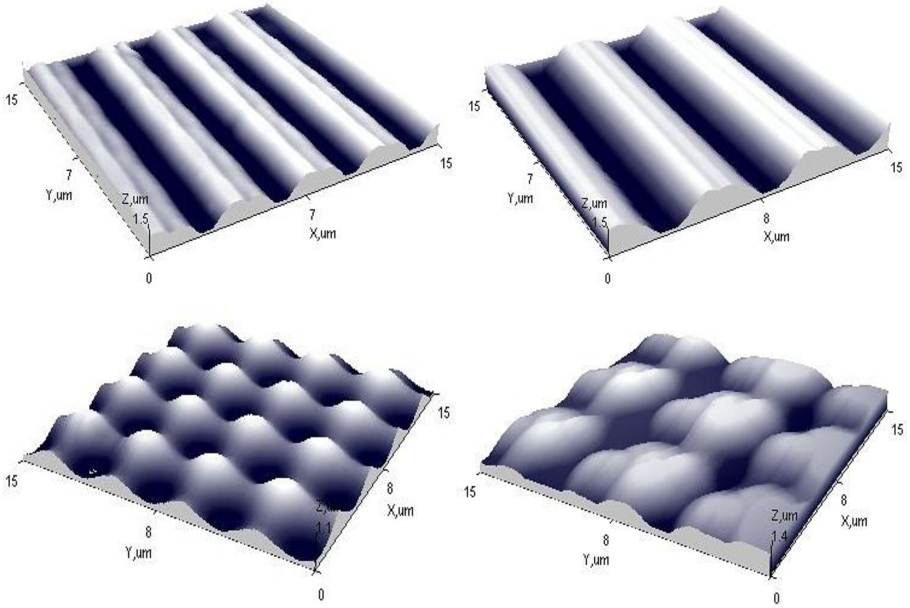

Figure 26. AFM pictures of line (top) and grid (bottom) patterned thin films TiO_2 samples

3.2.2. Photocatalytic Activity of Thin Film TiO_2

3.2.2.1. Aqueous Medium

The obtained decay curves period with line-patterned thin films TiO_2 and grid-patterned thin films TiO_2 are displayed in Figure 27. All layers indicated higher decomposition efficiency compared to photolysis alone. In this case, direct photolysis had a more noticeable effect which could be explained by a small reaction volume used in that series of experiments.

As already mentioned above, photoreactions are based on chemical reactions on the surface of the catalyst, thus the accessible surface area is an important factor for photocatalytic performance (36). The results of experiments distinctly indicate that with the decreasing size of period the photocatalytic efficiency noticeably increased. Which means that with smaller spacing during the patterning process, the higher surface available for photoreaction is obtained. The sample with grid-patterned structures was able to decolorize MB to a transparent solution during the tested timeframe.

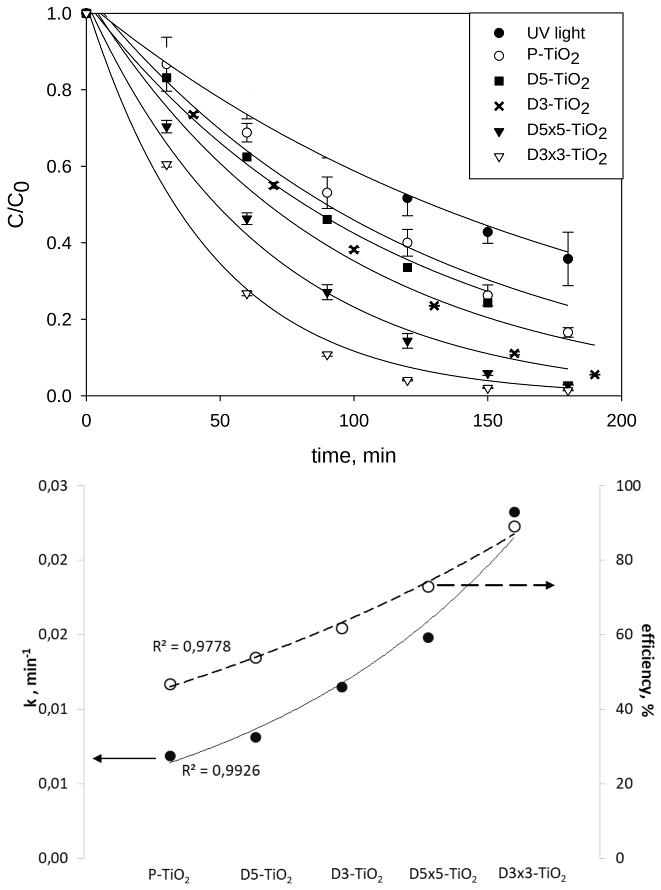

Figure 27. Decomposition kinetics (top) of Methylene Blue presented as a ratio of final concertation for the compound (C) vs. the initial concentration (C_0) obtained by different thin films TiO_2: line (D3-TiO_2 and D5-TiO_2), and grid patterned (D3x3-TiO_2 and D5x5-TiO_2) as well as UV-C light alone and non-structured thin film TiO_2 (P-TiO_2). And relation of decay constants (min^{-1}) and photoefficiencies of structured thin film TiO_2 as well as non-structured thin film TiO_2 (bottom)

The final efficiencies of thin film TiO_2 were arranged in the following order D3x3-TiO_2 > D5x5-TiO_2 > D3-TiO_2 > D5-TiO_2 > P-TiO_2. Moreover, there was an exponential relation between both decay rate and efficiency and the surface area of the structured thin films of TiO_2 (Figure 27).

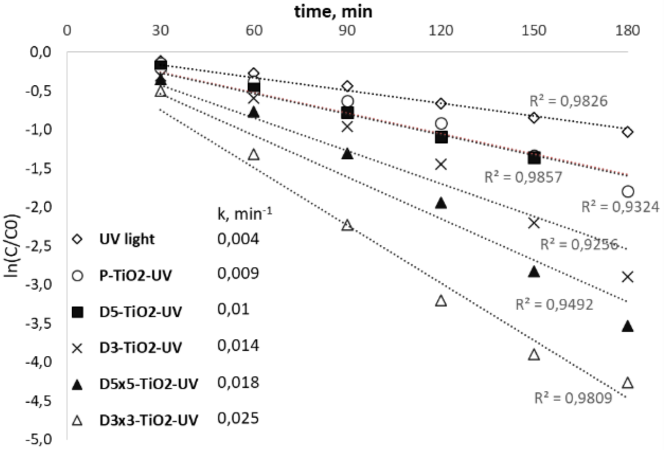

Figure 28. Photoreaction decay constants (min^{-1}) for line patterned thin films TiO_2 (D5-TiO_2-UV, D3-TiO_2-UV), grid patterned thin films TiO_2 (D5x5-TiO^2-UV, D3x3-TiO_2-UV) as well as non-structured (P-TiO_2) thin film TiO_2

Even though TiO_2 thin film samples were mainly in the amorphous phase, they still demonstrated impressive efficiency in the experiments of decolorization of MB. The 50% decolorization of MB in less than half an hour for grid patterned samples (Table 14), while other researchers used to conduct experiments with TiO_2 thin film for much longer period of time (Table 8). The results of calculated relative 50% decolorization time indicates that the photocatalytic degradation of samples with a grid pattern increases significantly and is 4–5 times better comparing to the plain (P-TiO_2, Table 14) sample. The results could be influenced not only by the surface area available for the contact of pollutant molecules and catalyst but also the type of the reactor employed in this experiment used all of its advantages, i.e. high illumination zone to the surface per unit volume of the reactor, thin film of liquid above the sample and as a consequence the photoactivation of the TiO_2 were higher.

Table 14. Characterization of TiO_2 thin film samples, surface roughness, relative decomposition time of 50 % of initial MB concentration and final photodecolorization of MB efficiencies

Sample	R_a, µm	s, a.u	Measured decomposition time of 50% of MB		Relative decomposition time of 50% of MB, t_r min	Final decolorization efficiency, %
			t_D, min	t_P, min		
P-TiO_2	-	-	90	-	90	83.4
D3-TiO_2	0.33±0.03	0.44	-	68	41	94
D3x3-TiO_2	0.21±0.03	0.79	-	33	18	98.6
D5-TiO_2	0.43±0.03	0.57	-	82	76	74.4*
D5x5-TiO_2	0.22±0.03	0.62	-	49	24	97.1

*after 150min of experiment

Another reason for the registered results of the structured TiO_2thin film could be a “waveguide” phenomenon, i.e. light is trapped inside the layer of the solution between air/solution interface and the TiO_2 film surface (Figure 29). The UV light illuminating the sample is diffracted on the patterned TiO_2 surface and is rearranged in some number of diffraction maxima and travels towards solution/air interface.

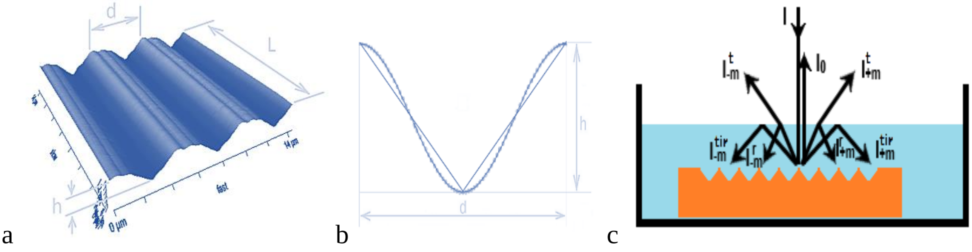

Figure 29. Arrangement of illuminating (I), specular reflected (I_0) and diffracted UV light ($I_{+/-m}$): diffraction maxima transmitted backwards into the air (I^t), diffraction maxima reflected at solution-air interface (I^r), diffraction maxima reflected due to total internal reflection (I^{tir}). Index +/-m describes the order of diffraction maxima. The solution is shown in blue color and the patterned TiO_2 film is in orange; dimensions of objects in this image are not proportional

This phenomenon occurs because of the present of the pattern on the surface of TiO_2 film. In the case of plain TiO_2 film, most of specular reflected (at the film surface) UV light is directed backwards from the solution to air. While in the case of the patterned surface significant amount of diffuse and specular reflected UV light, according to Lambert’s cosine law for a diffuse reflector, would undergo total internal reflection and will return to the TiO_2 surface, thus increasing photocatalytic effect. For line patterned samples, UV light is diffracted in direction perpendicular to the grooves of the pattern. In case of grid patterned samples, UV light is diffracted in two directions – both perpendicular to each direction of the grooves.

3.2.2. Chapter Summary

The versatile lithographic technique was successfully applied to form line and grid patterns for the structured increase in the surface prior synthesizing thin films TiO_2. Even though the samples of thin film TiO_2 were mainly amorphous phase, they still demonstrated impressive efficiency in the experiments of decolorization of MB. With decreasing size of the period, the photocatalytic efficiency noticeably increased. The sample with grid-patterned structures were able to decolorize MB to a transparent solution during the tested timeframe (180 min).

The patterning of the support for TiO_2 film allowed enhancing the photocatalytic efficiency by two mechanisms, i.e. due to the enlargement of the catalyst surface area as well as due to multiple UV light reflections in the solution.

4. GENERAL DISCUSSION AND RECOMMENDATIONS

4.1. Insights on the Key Properties of the Surface-mounted Photocatalyst

Various TiO_2 surface modification strategies have received a great interest, such as dimensional design, band structure design including doping with transitional metals or nonmetals, coupling with another SC, surface sensitization, etc. (74) in order to overcome the existing issues of this semiconductor, such as the low photo-quantum efficiency that arises from the fast recombination of photogenerated electrons and holes and photoresponse into visible light regions. This work focuses on TiO_2 surfaces modification related with structural dimensionalities. As the interest in 1D structural dimensionality of SCs is increasing because of numerous advantages it possesses, synthesized TiO_2 nanofibres displayed comparable physicochemical properties to commercially available TiO_2 powder. Moreover, the physical increase in the surface of the support for a photocatalytic thin film (2D) by interference lithography prior the deposition of TiO_2 was applied to enhance the photocatalysis efficiency.

Although the superior performance of the biphasic TiO_2 is widely known, especially in the case of benchmark photocatalyst P25, the mixture of both phases in this study did not have a significant positive effect on the performance of the nanofibrous photocatalyst. Nevertheless, anatase demonstrated to the most photoactive phase of TiO_2 in this research as in agreement with a number of other studies (Table 8). The degree of crystallinity is very important for the photoactivity of TiO_2, because structural defects can act as recombination centers of photogenerated carriers. This could be achieved by a right temperature range, incensement speed, calcination atmosphere, and the ratio between components of the spinning solution. For example, Mehrpouya et al. (95) found out that lower precursor/solvent ratio leads to a higher crystallinity index of the final material. This research demonstrated that primary materials can also determine not only the size of crystallites, but the calcination temperature range. As in the case of a TiO_2thin film, there was no additional calcination step after the PVD process. Therefore, all samples were amorphous. Nevertheless, the increase in photoactivity with the increased surface area of the support was monitored. In the recent literature, the amorphous TiO_2 is considered as a very good, cheap alternative to crystalline TiO_2. This is mostly because of more easy preparation methods and ability to be doped with more elements for the improvement of its performance.

There is still a high demand for effective, economical, and environmentally friendly water treatment technologies because of the growing world population and the more restrictive legislation. As it was discussed in previous sections, AOP is an obvious candidate to improve the current technological options. The main drawback for practical application of fibrous TiO_2 photocatalysis is the fact that most research works in water treatment are performed with dispersed TiO_2 materials (Table 8). Therefore, the immobilization of titania on different kinds of supports and the design of reactors that maintain good efficiency despite the reduction in the catalyst surface area and the mass transfer limitations in immobilized systems are an important issue (10).

TiO_2 particles are often immobilized on a solid support in order to prevent the transfer of the catalyst material to the treated medium. Two main strategies have been applied for immobilization of TiO_2 powders so far, namely coating on supporting materials via dipping or similar process and fabricating TiO_2 as a film (152). However, most reported solid supports have a low specific surface area that may lead to the decrease in the TiO_2 activity. Moreover, there is still a lack of information and research on the surface mounted fibrous TiO_2 photocatalyst. Several different immobilization methods were tested in this work, i.e. deposition from solution, tape-casting, and spray-coating. Since PCO could be named as a superficial process as photons must reach the surface of SC, the thickness of a photocatalyst layer is not an active factor in the case of more than 500 nm, the penetration depth of UV and visible light in semiconductors (172). In this work, photocatalytic layers on traditional supports, i.e. glass and SS, were relatively dense and demonstrated lower sorption abilities and photocatalytic activity than the fibre-on-fibre structure with PA12 as support. Good photocatalytic efficiency of the fibre-on-fibre structure implies that good photocatalytic activity can be achieved with a smaller amount of catalyst mounted on a highly porous support that provides a large active surface. Such design is also favorable in the environmental standpoint as the amounts of materials used for the manufacturing of the catalyst and the waste of spent catalyst are minimized. Mass that fully covers microfibre is enough as more does not have positive influence on efficiency and becomes difficult to handle, i.e. it is not stable on the surface.

Stability tests are very important for possible practical application of synthesized materials. As mentioned above, no loss of TiO_2 nanofibrous structures was observed, thus no further experiments on catalyst stability were conducted at this point, recognizing that such tests need well designed experiments on their own, especially considering a different medium that catalysts were tested against. Further research for stability of this novel composite structure is required. Nevertheless, there are applicable techniques to improve stability of organic/inorganic composites, such as chemical bonding (173), electrostatic layer-by-layer assembly (174), solvent-cast processes (175).

The polymeric supports for TiO_2 immobilization are getting more attention because of their properties, such as high durability, availability, and hydrophobic nature. PA12 has been chosen as a support for titania nanostructures because it is readily available, inert, inexpensive, and non-toxic. Moreover, being a hydrophobic material, it has an advantage to pre-concentrate organic pollutants on its surface, thereby increasing the availability of the target pollutant and following photodegradation. Similarly, Singh et al. (175) emphasized the advantages of polystyrene and TiO_2 composite photocatalyst for environmental remediation. Zou et al. (169) investigated the hydrophobic SiC and the hydrophilic TiO_2 synergetic effect to drive photogenerated electrons and holes participate in the degradation in more efficient ways and concluded that the interaction between water molecules and catalyst might be another interest in the gas-phase photocatalytic degradation.

4.2. Photoreactor Reactor Design

The comparison of the results is an important part while reporting and discussing research. When it comes down to comparing photocatalytic properties, many factors affect outcomes, such as model pollutant and its concentration, reaction volume, light source, reactors, etc. These factors usually are unique to every experiment reported, because of the absence of agreed standard conditions and quantitative procedures that would enable predictions of photocatalytic results on the basis of fundamental aspects such as the reaction rate constants and adsorption. Quantum efficiency may seem as a good dimension for the comparison, since it describes molecules undergoing reaction to the number of photons absorbed by the catalyst. Yet, it is not common data to be reported. On the other hand, quantum yields cannot serve as a general measure for the quality of the photocatalyst, mainly because it depends on the same specific working conditions, i.e. a model compound, its concentration, layer thickness, light intensity and wavelength, etc. Another for non-volatile final products, mineralization ratio, value between the evolved CO_2 during the photodegradation and theoretically possible CO_2 depending on the input of the primary compound, is difficult to measure in the research with low levels concentrations of model pollutants.

The main operational parameters of the PCO reactor design for an aqueous medium include an optimal catalyst loading, pH, radiation intensity and wavelength distribution which may be influenced by turbidity and dissolved oxygen. The application of photocatalysis in an air medium is affected mostly by the RH, inlet concentrations and residence time or, in the other words, the catalyst and pollutant contact probability. As already mentioned, the synergy between photocatalysis and adsorption might be of interest. The coupling of both technologies can be performed either installing an adsorption unit as pre-concentration step or using the adsorption as a backup system, where the adsorbent retains unreacted compounds or by-products. Alternatively, the coupling may be obtained in one single step by the utilization of hybrid materials, where the adsorption capacity enhances the photocatalytic activity and, simultaneously, photocatalytic regeneration of the adsorbent may take place (10, 176). It was found out that the removal of air pollutants can improve the indoor air quality even with a decreased ventilation rate. Therefore, PCO reactors may be integrated into new and existing HVAC systems due to their modular design and advantageous operation, such as negligible pressure drop, low power consumption and low maintenance requirements (31). Table 15 summarizes some important parameters of the photocatalyst itself and the system for nanofibrous catalysts in the use for environmental remediation purposes and Figure 9 presents detailed schematics of photoreactor used in this study for gaseous toluene decomposition.

The multi-pass method may be an alternative to relatively extend the residence time of VOCs for the PCO technology applied in a HVAC system (27). On the other hand, the increment of traveling distance of air stream in the reactor could increase the contact probability between target molecules and the photocatalyst. For example, Lee and colleagues (32) used a single-tangent flow inlet (example shown in Figure 30) and reported that the travel distance increased six times compared with basis design of the cylindrical procreator. Moreover, both conversion and quantum yield have increased. The other research group (177) has chosen a different way and proposed a spiral photoreactor for efficient degradation of pollutants. The particularity of this photoreactor was that a glass tube coated on the inside with TiO_2 was spiraled around a UV lamp.

Furthermore, the PA12 may serve as a universal support; can be fixed on SS grid or used loose as a packed-bed reactor. Further expansion of the application of such catalyst in gaseous environment may be addressed towards the design of a reactor in order to take advantage from wake and eddy flow or multi-pass air flow. Packed bed reactors are of a simple construction and can have high conversion per unit mass of a catalyst, low operating cost, and continuous operation.

Another important aspect for the photocatalysis and reactor design is the need of an appropriate radiation source. Artificial sources can be arc lamps, incandescent lamps, fluorescent lamps, lasers or light-emitting diodes (LEDs) (10). As it was mentioned, TiO_2 may be excited by light shorter than 400 nm and one of the drawbacks of this semiconductor is the ability to use less than 5% of solar irradiation. Nevertheless, there was a successful modification of the surface of TiO_2 with other metal or non-metal with the intense to decrease the bad-gap and UV-LEDs is getting attention for the usage in photocatalysis.

Table 15. Summary of some most important operational parameters for utility of nanofibrous photocatalyst in the environmental medium

Operational parameter	***Value range***	***Based on***
Aqueous medium		
Surface roughness of catalyst, µm	>0.3	This research
Surface loading, mg/cm^2	0.06–0.1	This research
Light source	UV (λ<400 nm)	(138, 143, 145)
Distance/thin layer of solution, cm	≤10/1	This research, (145)
Air medium		
Air velocity in reactor, m/s	≤0.1 (4 L/min)	This research
Inlet concentration, ppm	≤1	This research, (155)
Surface roughness of catalyst, µm	>0.3	This research
Surface loading, mg/cm^2	0.06–0.1	This research
Light source	UV (λ<400 nm)	(144)
RH, %	30–50	(140, 155)

Promising alternatives are not only hybrid photocatalysts but recoverable magnetic photocatalytic particles as well. Here, the electrospinning may be a handy technique with the following sol-gel process, or even having amorphous TiO_2 with its high possibilities for doping.

Knowing that PCO is a collection of chain reactions and production of intermediates, the contamination of the surface of the photocatalyst is possible. Phenomena of deactivation of the photocatalyst is more predominant in the gas phase than in the aqueous phase. This is mainly because water molecules in an aqueous phase restore the surface hydroxylation and may assist in the removal of some adsorbed species. Meanwhile, in the gas phase, these species with slower photokinetics and possibly high adsorption affinity towards the surface of the photocatalyst than the target pollutant may cause a deactivation by blocking active sites. The regeneration of a photocatalyst is the decision. The continuous treatment by proper illumination in humid atmosphere could ensure easier removal of any strongly adsorbed species. It seems that water vapor stabilizes the catalyst surface by regenerating adsorbed hydroxyl groups, as these species play a key role in the photoreactive process. However, other methods are necessary to remove non-volatile by-products, such as washing with water or alkaline solutions or even the thermal treatment (29, 31).

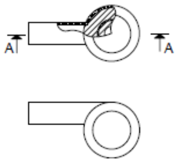

Figure 30. A detailed scheme of a photoreactor used in this study (top) and an example of the top view of the reactor with a single-tangent flow inlet (bottom)

Finally, the efficiency of the final photocatalytic system depends on the nature and the concentration of pollutants, the inlet flow rates and contact probability and time between target molecules and the photocatalyst, the catalyst properties itself, such as crystallinity, available surface area, porosity, loading, etc., the characteristics of the treated medium, the wavelength distribution and radiation intensity of the light source, and the reactor design. Therefore, each application must be studied at first at laboratory scale, as comparison and scaling-up are difficult tasks.

5. CONCLUSIONS

1. A pathway for fabricating nanofibrous TiO_2 has been presented, considering the morphology, crystalline phase, and catalytic performance. The synthesis of nanofibres from the organic precursor of TiO_2 in the polymeric matrix has proved to be an efficient method for the development of fibrous TiO_2 leading to an equally dispersed TiO_2 crystals in the nanofibres. The optimum calcination temperatures (500–750°C) have been selected allowing to adjust the phases and crystallite sizes of TiO_2. Decomposition efficiency was the highest in the anatase phase nanofibrous TiO_2. Photodecolorization of the Methylene Blue solution reached 56% during 180 min treatment duration while oxalic acid was decomposed 100% for all tested catalyst morphologies.

2. The nanofibrous TiO_2 catalyst was immobilized on the surface by the solvent deposition, tape casting, and fibre-on fibre methods. The obtained layers featured a relatively high sorptive capacity (0.01–0.03 mg/mg) in an aqueous medium as a result of the high specific surface area (58.2–83.9 m^2/g) and the presence of mesopores. The surface roughness of layers (0.88–1.31 µm) and its sorption ability was determined to be related, while the density did not have a positive effect neither to sorption ability nor photo-activity. The polymeric support proved to be a good alternative to other supports because of a high surface area for short fibres and specific morphology that those two structures could form. Photodecolorization of Methylene Blue followed a linear decay function for the tested period and reached efficiency of 77% during 120 min treatment duration. Meanwhile, the decomposition of toluene in an air medium reached 87% destruction of the primary compound. A novel structure of composite inorganic nanofibres on an organic microfibers photocatalyst has been proven as technologically and practically favorable because of lower (>10 times) amounts of catalyst material producing good performance.

3. Microstructuring of the catalyst support proved to be an effective approach for providing a more available surface area of a photocatalyst for efficient process of the photocatalyst. There was an exponential relation between photodecolorization efficiency and microstructuring of thin films TiO_2, when the decreased period size of 3 µm in grid pattern demonstrated the highest photodecolorization efficiency of Methylene Blue in an aqueous medium up to 94% and >97% for line and grid patterns, respectively, during 180 min treatment duration. At the same time, several technological challenges are yet to be solved for increasing the technology readiness level of such systems.

REFERENCES

1. BYRNE, Ciara, SUBRAMANIAN, Gokulakrishnan and PILLAI, Suresh C. Recent advances in photocatalysis for environmental applications. *Journal of Environmental Chemical Engineering* [online]. 2018. Vol. 6, no. 3, p. 3531–3555. Available from: https://doi.org/10.1016/j.jece.2017.07.080
2. SRIKANTH, B., GOUTHAM, R., BADRI NARAYAN, R., RAMPRASATH, A., GOPINATH, K. P. and SANKARANARAYANAN, A. R. Recent advancements in supporting materials for immobilised photocatalytic applications in waste water treatment. *Journal of Environmental Management* [online]. 2017. Vol. 200, p. 60–78. Available from: http://dx.doi.org/10.1016/j.jenvman.2017.05.063.
3. DENG, Yang and ZHAO, Renzun. Advanced Oxidation Processes (AOPs) in Wastewater Treatment. *Current Pollution Reports*. 2015. Vol. 1, no. 3, p. 167–176. DOI 10.1007/s40726-015-0015-z.
4. SOLARCHEM ENVIRONMENTAL SYSTEMS. The UV/Oxidation Handbook. *Solarchem Environmental Systems*. 1994. No. 713, p. 68.
5. US ENVIRONMENTAL PROTECTION AGENCY. *Advanced Photochemical Oxidation Processes: Handbook*. 2015. ISBN 1298044073, 9781298044075.
6. ANTONOPOULOU, M., EVGENIDOU, E., LAMBROPOULOU, D. and KONSTANTINOU, I. A review on advanced oxidation processes for the removal of taste and odor compounds from aqueous media. *Water Research* [online]. 2014. Vol. 53, p. 215–234. Available from: http://dx.doi.org/10.1016/j.watres.2014.01.028
7. OXFORD UNIVERSITY PRESS. Oxford Reference. A Dictionary of Chemistry (6 ed.). [online]. 2008. [Accessed 12 September 2018]. Available from: http://www.oxfordreference.com/abstract/10.1093/acref/9780199204632.001.0001/acref-9780199204632-e-793?rskey=49h9xn&result=865
8. CARP, O., HUISMAN, C. L. and RELLER, A. Photoinduced reactivity of titanium dioxide. *Progress in Solid State Chemistry*. 2004. Vol. 32, no. 1–2, p. 33–177. DOI 10.1016/j.progsolidstchem.2004.08.001.
9. GAYA, Umar Ibrahim and ABDULLAH, Abdul Halim. Heterogeneous photocatalytic degradation of organic contaminants over titanium dioxide: A review of fundamentals, progress and problems. *Journal of Photochemistry and Photobiology C: Photochemistry Reviews*. 2008. Vol. 9, no. 1, p. 1–12. DOI 10.1016/j.jphotochemrev.2007.12.003.
10. CORONADO, Juan M, FRESNO, Fernando and PORTELA, Raquel. *Design of Advanced Photocatalytic Materials for Energy and Environmental Applications* [online]. London, 2013. ISBN 978-1-4471-5060-2. Available from: http://link.springer.com/10.1007/978-1-4471-5061-9
11. LU, Ming-Chun, ROAM, Gwo-Dong, CHEN, Jong-Nan and HUNG, Chin-Pao. Adsorption characteristics of dichlorvos onto hydrous titanium dioxide surface. *Water Research*. 1996. Vol. 30, no. 7, p. 1670–1676.
12. MALATO, S., FERNÁNDEZ-IBÁÑEZ, P., MALDONADO, M. I., BLANCO, J. and GERNJAK, W. Decontamination and disinfection of water by solar photocatalysis: Recent overview and trends. *Catalysis Today*. 2009. Vol. 147, no. 1, p. 1–59. DOI 10.1016/j.cattod.2009.06.018.
13. ZHONG, Lexuan, HAGHIGHAT, Fariborz, BLONDEAU, Partice and KOZINSKI, Janusz. Modeling and physical interpretation of photocatalytic oxidation efficiency in indoor air applications. *Building and Environment*. 2010. Vol. 45, no. 12, p. 2689–2697. DOI 10.1016/j.buildenv.2010.05.029.
14. SILVA, Cláudia Gomes and FARIA, Joaquim Luís. Effect of key operational parameters on the photocatalytic oxidation of phenol by nanocrystalline sol-gel TiO2 under UV

irradiation. *Journal of Molecular Catalysis A: Chemical*. 2009. Vol. 305, no. 1–2, p. 147–154. DOI 10.1016/j.molcata.2008.12.015.

15. OBEE, T. N. Photooxidation of sub-parts-per-million toluene and formaldehyde levels on titania using a glass-plate reactor. *Environmental Science & Technology*. 1996. Vol. 30, p. 3578–3584.
16. NASR, Maryline, EID, Cynthia, HABCHI, Ronald and MIELE, Phillippe. Recent Progress on Titanium Dioxide Nanomaterials for Photocatalytic Applications. *Chemistry and Sustainability Energy and Materials* [online]. 2018. P. 1–26. Available from: https://onlinelibrary.wiley.com/doi/pdf/10.1002/cssc.201800874
17. KERKEZ, Özge and BOZ, Ismail. Photo(electro)catalytic activity of Cu2+-modified TiO2nanorod array thin films under visible light irradiation. *Journal of Physics and Chemistry of Solids*. 2014. Vol. 75, no. 5, p. 611–618. DOI 10.1016/j.jpcs.2013.12.019.
18. ZARUBICA, A., VASIĆ, M., ANTONIJEVIC, M. D., RANCROSSED D SIGNELOVIĆ, M., MOMČILOVIĆ, M., KRSTIĆ, J. and NEDELJKOVIĆ, J. Design and photocatalytic ability of ordered mesoporous TiO2 thin films. *Materials Research Bulletin*. 2014. Vol. 57, p. 146–151. DOI 10.1016/j.materresbull.2014.03.015.
19. NASR, Maryline, BALME, Sébastien, EID, Cynthia, HABCHI, Roland, MIELE, Philippe and BECHELANY, Mikhael. Enhanced Visible-Light Photocatalytic Performance of Electrospun rGO/TiO2 Composite Nanofibers. *The Journal of Physical Chemistry C* [online]. 2017. Vol. 121, no. 1, p. 261–269. Available from: http://pubs.acs.org/doi/abs/10.1021/acs.jpcc.6b08840
20. ZHOU, Feng, YAN, Chunjie, LIANG, Tian, SUN, Qi and WANG, Hongquan. Photocatalytic degradation of Orange G using sepiolite-TiO2 nanocomposites: Optimization of physicochemical parameters and kinetics studies. *Chemical Engineering Science* [online]. 2018. Vol. 183, p. 231–239. Available from: https://doi.org/10.1016/j.ces.2018.03.016
21. BUM, Sang and CHANG, Sung. Kinetic study for photocatalytic degradation of volatile organic compounds in air using thin film TiO2 photocatalyst. *Applied Catalysis B: Environmental*. 2002. Vol. 35, no. 4, p. 305–315.
22. BOUZAZA, Abdelkrim, VALLET, C. and LAPLANCHE, A. Photocatalytic degradation of some VOCs in the gas phase using an annular flow reactor: Determination of the contribution of mass transfer and chemical reaction steps in the photodegradation process. *Journal of Photochemistry and Photobiology A: Chemistry*. 2006. Vol. 177, no. 2–3, p. 212–217. DOI 10.1016/j.jphotochem.2005.05.027.
23. ZHANG, Yin Ping, YANG, Rui, XU, Qiu Jian and MO, Jin Han. Characteristics of photocatalytic oxidation of toluene, benzene, and their mixture. *Journal of the Air and Waste Management Association*. 2007. Vol. 57, no. 1, p. 94–101. DOI 10.1080/10473289.2007.10465302.
24. ROEGIERS, Jelle, VAN WALSEM, Jeroen and DENYS, Siegfried. CFD- and radiation field modeling of a gas phase photocatalytic multi-tube reactor. *Chemical Engineering Journal* [online]. 2018. Vol. 338, no. November 2017, p. 287–299. Available from: https://doi.org/10.1016/j.cej.2018.01.047
25. AO, C. H., LEE, S. C., YU, J. Z. and XU, J. H. Photodegradation of formaldehyde by photocatalyst TiO2: Effects on the presences of NO, SO2 and VOCs. *Applied Catalysis B: Environmental*. 2004. Vol. 54, no. 1, p. 41–50. DOI 10.1016/j.apcatb.2004.06.004.
26. HENDERSON, Michael A. A surface science perspective on TiO2 photocatalysis. *Surface Science Reports*. 2011. Vol. 66, no. 6–7, p. 185–297. DOI 10.1016/j.surfrep.2011.01.001.
27. ZHONG, Lexuan, HAGHIGHAT, Fariborz, LEE, Chang Seo and LAKDAWALA, Ness.

Performance of ultraviolet photocatalytic oxidation for indoor air applications: Systematic experimental evaluation. *Journal of Hazardous Materials*. 2013. Vol. 261, p. 130–138. DOI 10.1016/j.jhazmat.2013.07.014.

28. AGHIGHI, Alireza and HAGHIGHAT, Fariborz. Using physical-chemical properties of reactants to estimate the performance of photocatalytic oxidation air cleaners. *Building and Environment* [online]. 2015. Vol. 85, p. 114–122. Available from: http://dx.doi.org/10.1016/j.buildenv.2014.11.020
29. KOROLOGOS, Christos A., PHILIPPOPOULOS, Constantine J. and POULOPOULOS, Stavros G. The effect of water presence on the photocatalytic oxidation of benzene, toluene, ethylbenzene and m-xylene in the gas-phase. *Atmospheric Environment* [online]. 2011. Vol. 45, no. 39, p. 7089–7095. DOI 10.1016/j.atmosenv.2011.09.038. Available from: http://dx.doi.org/10.1016/j.atmosenv.2011.09.038
30. ZHU, Xiaobing, CHANG, Da Lei, LI, Xiao Song, SUN, Zhi Guang, DENG, Xiao Qing and ZHU, Ai Min. Inherent rate constants and humidity impact factors of anatase TiO2 film in photocatalytic removal of formaldehyde from air. *Chemical Engineering Journal* [online]. 2015. Vol. 279, p. 897–903. Available from: http://dx.doi.org/10.1016/j.cej.2015.05.095
31. MO, Jinhan, ZHANG, Yinping, XU, Qiujian, LAMSON, Jennifer Joaquin and ZHAO, Rongyi. Photocatalytic purification of volatile organic compounds in indoor air: A literature review. *Atmospheric Environment* [online]. 2009. Vol. 43, no. 14, p. 2229–2246. Available from: http://dx.doi.org/10.1016/j.atmosenv.2009.01.034
32. LEE, David Minzae, YUN, Hyeong Jin, YU, Sungju, YUN, Seong Jin, LEE, Sun Young, KANG, Sang Hyeon and YI, Jongheop. Design of an efficient photocatalytic reactor for the decomposition of gaseous organic contaminants in air. *Chemical Engineering Journal* [online]. 2012. Vol. 187, p. 203–209. Available from: http://dx.doi.org/10.1016/j.cej.2012.01.121
33. HODGSON, A. T., DESTAILLATS, H., SULLIVAN, D. P. and FISK, W. J. Performance of ultraviolet photocatalytic oxidation for indoor air cleaning applications. *Indoor Air*. 2007. Vol. 17, no. 4, p. 305–316. DOI 10.1111/j.1600-0668.2007.00479.x.
34. LV, Jinze and ZHU, Lizhong. Highly efficient indoor air purification using adsorption-enhanced-photocatalysis-based microporous TiO2 at short residence time. *Environmental Technology (United Kingdom)*. 2013. Vol. 34, no. 11, p. 1447–1454. DOI 10.1080/09593330.2012.752875.
35. GIOLLI, Carlo, BORGIOLI, Francesca, CREDI, Alberto, FABIO, Alberto Di, FOSSATI, Alessio, MIRANDA, Maurizio Muniz, PARMEGGIANI, Silvia, RIZZI, Gabriele, SCRIVANI, Andrea, TROGLIO, Sergio, TOLSTOGUZOV, Alexander, ZOPPI, Angela and BARDI, Ugo. Characterization of TiO2 coatings prepared by a modified electric arc-physical vapour deposition system. *Surface and Coatings Technology*. 2007. Vol. 202, no. 1, p. 13–22. DOI 10.1016/j.surfcoat.2007.04.043.
36. NAKATA, Kazuya and FUJISHIMA, Akira. TiO2 photocatalysis: Design and applications. *Journal of Photochemistry and Photobiology C: Photochemistry Reviews*. 2012. Vol. 13, no. 3, p. 169–189. DOI 10.1016/j.jphotochemrev.2012.06.001.
37. SARAVANAN, R., GRACIA, F. and STEPHEN, A. Basic Principles, Mechanism, and Challenges of Photocatalysis. In : KHAN, Mohammad Mansoob, PRADHAN, Debabrata and SOHN, Youngku (eds.), *Nanocomposites for Visible Light-induced Photocatalysis*. 1st. Springer, Cham, 2017. p. 19–40. ISBN 978-3-319-62446-4.
38. OHTANI, B. Photocatalysis A to Z-What we know and what we do not know in a scientific sense. *Journal of Photochemistry and Photobiology C: Photochemistry Reviews* [online]. 2010. Vol. 11, no. 4, p. 157–178. Available from: http://dx.doi.org/10.1016/j.jphotochemrev.2011.02.001

39. LI, Xin, YU, Jiaguo and JARONIEC, Mietek. Hierarchical photocatalysts. *Chemical Society Reviews* [online]. 2016. Vol. 45, no. 9, p. 2603–2636. Available from: http://dx.doi.org/10.1039/C5CS00838G
40. WANG, Songcan, YUN, Jung Ho, LUO, Bin, BUTBUREE, Teera, PEERAKIATKHAJOHN, Piangjai, THAWEESAK, Supphasin, XIAO, Mu and WANG, Lianzhou. Recent Progress on Visible Light Responsive Heterojunctions for Photocatalytic Applications. *Journal of Materials Science and Technology* [online]. 2017. Vol. 33, no. 1, p. 1–22. Available from: http://dx.doi.org/10.1016/j.jmst.2016.11.017
41. BIANCHI, Claudia L., PIROLA, Carlo, GALLI, Federico, CERRATO, Giuseppina, MORANDI, Sara and CAPUCCI, Valentino. Pigmentary TiO2: A challenge for its use as photocatalyst in NOx air purification. *Chemical Engineering Journal*. 2015. Vol. 261, p. 76–82. DOI 10.1016/j.cej.2014.03.078. T
42. PRAHSARN, Chureerat, KLINSUKHON, Wattana and ROUNGPAISAN, Nanjaporn. Electrospinning of PAN/DMF/H2O containing TiO2 and photocatalytic activity of their webs. *Materials Letters*. 2011. Vol. 65, no. 15–16, p. 2498–2501. DOI 10.1016/j.matlet.2011.05.018.
43. DOH, Seok Joo, KIM, Cham, LEE, Se Geun, LEE, Sung Jun and KIM, Hoyoung. Development of photocatalytic TiO2 nanofibers by electrospinning and its application to degradation of dye pollutants. *Journal of Hazardous Materials*. 2008. Vol. 154, no. 1–3, p. 118–127. DOI 10.1016/j.jhazmat.2007.09.118.
44. HU, Meiling, FANG, Minghao, TANG, Chao, YANG, Tao, HUANG, Zhaohui, LIU, Yangai, WU, Xiaowen and MIN, Xin. The effects of atmosphere and calcined temperature on photocatalytic activity of TiO2 nanofibers prepared by electrospinning. *Nanoscale research letters*. 2013. Vol. 8, no. 1, p. 548. DOI 10.1186/1556-276X-8-548.
45. FUJISHIMA, Akira, ZHANG, Xintong and TRYK, Donald A. TiO2 photocatalysis and related surface phenomena. *Surface Science Reports*. 2008. Vol. 63, no. 12, p. 515–582. DOI 10.1016/j.surfrep.2008.10.001.
46. HERNÁNDEZ-ALONSO, María D., TEJEDOR-TEJEDOR, Isabel, CORONADO, Juan M. and ANDERSON, Marc A. Operando FTIR study of the photocatalytic oxidation of methylcyclohexane and toluene in air over TiO2-ZrO2thin films: Influence of the aromaticity of the target molecule on deactivation. *Applied Catalysis B: Environmental*. 2011. Vol. 101, no. 3–4, p. 283–293. DOI 10.1016/j.apcatb.2010.09.029.
47. WEN, Jiuqing, LI, Xin, LIU, Wei, FANG, Yueping, XIE, Jun and XU, Yuehua. Photocatalysis fundamentals and surface modification of TiO2 nanomaterials. *Cuihua Xuebao/Chinese Journal of Catalysis* [online]. 2015. Vol. 36, no. 12, p. 2049–2070. Available from: http://dx.doi.org/10.1016/S1872-2067(15)60999-8
48. KAUR, Kulbir and SINGH, Chandra Veer. Amorphous TiO2 as a photocatalyst for hydrogen production: A DFT study of structural and electronic properties. *Energy Procedia* [online]. 2012. Vol. 29, p. 291–299. Available from: http://dx.doi.org/10.1016/j.egypro.2012.09.035
49. MAO, Shuai, BAO, Rui, FANG, Dong and YI, Jianhong. Influence of electron acceptor and carrier in amorphous TiO2 upon the photocatalytic degradation of methylene orange. *Materials Research Express*. 2018. Vol. 5, no. 4.
50. GHUMAN, Kulbir Kaur. Mechanistic insights into water adsorption and dissociation on amorphous -based catalysts. *Science and Technology of Advanced Materials* [online]. 2018. Vol. 19, no. 1, p. 44–52. Available from: https://doi.org/10.1080/14686996.2017.1410055
51. GUO, Si Yao, HAN, Song, CHI, Bo, PU, Jian and LI, Jian. A facile low-temperature

approach to designing controlled amorphous-based titania composite photocatalysts with excellent noble-metal-free photocatalytic hydrogen production. *ACS Applied Materials and Interfaces*. 2014. Vol. 6, no. 7, p. 4743–4751. DOI 10.1021/am4054095.

52. RAMAKRISHNA, Seeram, FUJIHARA, Kazutoshi, TEO, Wee-Eong, LIM, Teik-Cheng and MA, Zuwei. *An Introduction to Electrospinning and Nanofibers* [online]. Singapore : WORLD SCIENTIFIC, 2005. ISBN 978-981-256-415-3. Available from: https://www.worldscientific.com/worldscibooks/10.1142/5894
53. ZENG, XG, ZHUANG, J, GONG, M, ZHENG, XW and LI, MT. Study on nano-TiO2 film prepared by hydrothermal method in toluene-hydrochloric acid-water system. In : *PROGRESS IN ENVIRONMENTAL SCIENCE AND ENGINEERING*. 2013. p. 3247–3251.
54. HABRAN, Margarita, KRAMBROCK, Klaus, MAIA DA COSTA, M. E.H., MORGADO, Edisson and MARINKOVIC, Bojan A. TiO2 anatase nanorods with non-equilibrium crystallographic {001} facets and their coatings exhibiting high photo-oxidation of NO gas. *Environmental Technology (United Kingdom)*. 2018. Vol. 39, no. 2, p. 231–239. DOI 10.1080/09593330.2017.1297852.
55. WU, Xiaofeng, FANG, Shun, ZHENG, Yang, SUN, Jie and LV, Kangle. Thiourea-Modified TiO2 Nanorods with Enhanced Photocatalytic Activity. *Molecules* [online]. 2016. Vol. 21, no. 2, p. 181. Available from: http://www.mdpi.com/1420-3049/21/2/181
56. FEI, Linfeng, LU, Wei, HU, Yongming, GAO, Guanyin, YONG, Zehui, SUN, Tieyu, ZHOU, Naigen, GU, Haoshuang and WANG, Yu. Evidencing the structural conversion of hydrothermally synthesized titanate nanorods by in situ electron microscopy. *Journal of Materials Chemistry A*. 2017. Vol. 5, no. 8, p. 3786–3791. DOI 10.1039/C6TA09883E.
57. WONGAREE, Mathana, CHIARAKORN, Siriluk, CHUANGCHOTE, Surawut and SAGAWA, Takashi. Photocatalytic performance of electrospun CNT/TiO2 nanofibers in a simulated air purifier under visible light irradiation. *Environmental Science and Pollution Research*. 2016. DOI 10.1007/s11356-016-7348-z.
58. WANG, Jianan, YANG, Guorui, LYU, Wei and YAN, Wei. Thorny TiO2 nanofibers: Synthesis, enhanced photocatalytic activity and supercapacitance. *Journal of Alloys and Compounds*. 2016. Vol. 659, p. 138–145. DOI 10.1016/j.jallcom.2015.10.233.
59. SINGH, Narendra, MONDAL, Kunal, MISRA, Mrinmoy, SHARMA, Ashutosh and GUPTA, Raju Kumar. Quantum dot sensitized electrospun mesoporous titanium dioxide hollow nanofibers for photocatalytic applications. *RSC Advances*. 2016. Vol. 6, no. 53, p. 48109–48119. DOI 10.1039/c6ra04305d.
60. SONG, Jun, WANG, Xueqin, YAN, Jianhua, YU, Jianyong, SUN, Gang and DING, Bin. Soft Zr-doped TiO2 Nanofibrous Membranes with Enhanced Photocatalytic Activity for Water Purification. *Scientific Reports* [online]. 2017. Vol. 7, no. 1, p. 1636. Available from: http://www.nature.com/articles/s41598-017-01969-w
61. MONDAL, Kunal, BHATTACHARYYA, Souryadeep and SHARMA, Ashutosh. Photocatalytic degradation of naphthalene by electrospun mesoporous carbon-doped anatase TiO2 nanofiber mats. *Industrial and Engineering Chemistry Research*. 2014. Vol. 53, no. 49, p. 18900–18909. DOI 10.1021/ie5025744..
62. LIU, Shanhu, LIU, Baoshun, NAKATA, Kazuya, OCHIAI, Tsuyoshi, MURAKAMI, Taketoshi and FUJISHIMA, Akira. Electrospinning preparation and photocatalytic activity of porous TiO2 Nanofibers. *Journal of Nanomaterials*. 2012. Vol. 2012. DOI 10.1155/2012/491927.
63. GUNJI, Shunsuke, SHIMOTSUMA, Yasuhiko and MIURA, Kiyotaka. Synthesis and photocatalytic properties of SiO2/TiO2 nanofibers using templates of TEMPO-oxidized

cellulose nanofibers. *Journal of Sol-Gel Science and Technology* [online]. 2016. Vol. 79, no. 1, p. 151–159. Available from: http://link.springer.com/10.1007/s10971-016-4033-0

64. LIAO, Yulong, YUAN, Botao, ZHANG, Dainan, ZHANG, Jin, WANG, Xiaoyi, DENG, Peng, ZHANG, Kaibin, ZHANG, Huaiwu, XIANG, Quanjun and ZHONG, Zhiyong. Fabrication of Heterostructured Metal Oxide/TiO2 Nanotube Arrays Prepared via Thermal Decomposition and Crystallization. *Inorganic Chemistry* [online]. 2018. Vol. 57, no. 16, p. 10249–10256. Available from: http://pubs.acs.org/doi/10.1021/acs.inorgchem.8b01483
65. WANG, Gang, CHEN, Qinghua, LIU, Yongping, MA, Dong, XIN, Yanjun, MA, Xiaohan and ZHANG, Xinwang. In situ synthesis of graphene/WO3 co-decorated TiO2nanotube array photoelectrodes with enhanced photocatalytic activity and degradation mechanism for dimethyl phthalate. *Chemical Engineering Journal* [online]. 2018. Vol. 337, no. November 2017, p. 322–332. Available from: https://doi.org/10.1016/j.cej.2017.12.058ic treatment of environmental pollutants and further application in water purification.
66. SU, Jingyang, ZHU, Lin, GENG, Ping and CHEN, Guohua. Self-assembly graphitic carbon nitride quantum dots anchored on TiO2 nanotube arrays: An efficient heterojunction for pollutants degradation under solar light. *Journal of Hazardous Materials* [online]. 2016. Vol. 316, p. 159–168. Available from: http://dx.doi.org/10.1016/j.jhazmat.2016.05.004
67. MEI, Fei, YANG, Zhijie, WU, Linzhang, ZHOU, Yuanming and ZHANG, Danming. Influence of annealing temperature on structure and photocatalytic activity of TiO2 thin films prepared by DC reactive magnetron sputtering method. *Wuhan University Journal of Natural Sciences* [online]. 2012. Vol. 17, no. 4, p. 309–314. Available from: http://link.springer.com/10.1007/s11859-012-0847-y
68. ZHANG, Yanrong and LI, Qian. Synthesis and characterization of Fe-doped TiO2 films by electrophoretic method and its photocatalytic activity toward methyl orange. Available from: http://dx.doi.org/10.1016/j.solidstatesciences.2012.11.012
69. ZHANG, Yanrong, WAN, Jing and KE, Youqing. A novel approach of preparing TiO2 films at low temperature and its application in photocatalytic degradation of methyl orange. *Journal of Hazardous Materials* [online]. 2010. Vol. 177, no. 1–3, p. 750–754. Available from: http://dx.doi.org/10.1016/j.jhazmat.2009.12.095
70. GU, Yuanqing and HUANG, Jianguo. Precise size control over ultrafine rutile titania nanocrystallites in hierarchical nanotubular silica/titania hybrids with efficient photocatalytic activity. *Chemistry - A European Journal*. 2013. Vol. 19, no. 33, p. 10971–10981. DOI 10.1002/chem.201300649.
71. JO, Min Su, PARK, Gi Dae, KANG, Yun Chan and CHO, Jung Sang. Design and synthesis of interconnected hierarchically porous anatase titanium dioxide nanofibers as high-rate and long-cycle-life anodes for lithium-ion batteries. *Nanoscale*. 2018. Vol. 10, no. 28, p. 13539–13547. DOI 10.1039/c8nr01666f.
72. MARTÍNEZ-PÉREZ, Carlos A., OLIVAS-ARMENDARIZ, Imelda, CASTRO-CARMONA, Javier S and GARCÍA-CASILLAS, Perla E. Scaffolds for Tissue Engineering Via Thermally Induced Phase Separation. *Advances in Regenerative Medicine* [online]. 2011. P. 275–294. DOI 10.5772/25476. Available from: http://www.intechopen.com/books/advances-in-regenerative-medicine/scaffolds-for-tissue-engineering-via-thermally-induced-phase-separation
73. FRIEDMANN, Donia, MENDIVE, Cecilia and BAHNEMANN, Detlef. TiO2 for water treatment: Parameters affecting the kinetics and mechanisms of photocatalysis. *Applied Catalysis B: Environmental* [online]. 2010. Vol. 99, no. 3–4, p. 398–406. Available

from: http://dx.doi.org/10.1016/j.apcatb.2010.05.014

74. VERBRUGGEN, Sammy W. TiO2 photocatalysis for the degradation of pollutants in gas phase: From morphological design to plasmonic enhancement. *Journal of Photochemistry and Photobiology C : Photochemistry Reviews* [online]. 2015. Vol. 24, p. 64–82. Available from: http://dx.doi.org/10.1016/j.jphotochemrev.2015.07.001
75. GAO, Minmin, ZHU, Liangliang, ONG, Wei Li, WANG, Jing and HO, Ghim Wei. Structural design of TiO2-based photocatalyst for H2 production and degradation applications. *Catalysis Science and Technology* [online]. 2015. Vol. 5, no. 10, p. 4703–4726. Available from: http://dx.doi.org/10.1039/C5CY00879D
76. HUANG, Jiarui, REN, Haibo, LIU, Xiaosi, LI, Xuexue and SHIM, Jae Jin. Facile synthesis of porous TiO2 nanospheres and their photocatalytic properties. *Superlattices and Microstructures* [online]. 2015. Vol. 81, p. 16–25. Available from: http://dx.doi.org/10.1016/j.spmi.2015.01.012
77. TANG, Hua, ZHANG, Du, TANG, Guogang, JI, Xiaorui, LI, Changsheng, YAN, Xuehua and WU, Qiong. Low temperature synthesis and photocatalytic properties of mesoporous TiO2 nanospheres. *Journal of Alloys and Compounds* [online]. 2014. Vol. 591, p. 52–57. Available from: http://dx.doi.org/10.1016/j.jallcom.2013.12.176
78. ARCHANA, J., HARISH, S., KAVIRAJAN, S., NAVANEETHAN, M., PONNUSAMY, S., SHIMOMURA, M., MUTHAMIZHCHELVAN, C., IKEDA, H. and HAYAKAWA, Y. Ultra-fast photocatalytic and dye-sensitized solar cell performances of mesoporous TiO2 nanospheres. *Applied Surface Science* [online]. 2018. Vol. 449, p. 729–735. Available from: http://dx.doi.org/10.1016/j.apsusc.2018.01.105
79. WANG, Shuan, DING, Yong, XU, Sichao, ZHANG, Yunxia, LI, Guanghai, HU, Linhua and DAI, Songyuan. TiO2 nanospheres: A facile size-tunable synthesis and effective light-harvesting layer for dye-sensitized solar cells. *Chemistry - A European Journal*. 2014. Vol. 20, no. 17, p. 4916–4920. DOI 10.1002/chem.201304963.
80. AGOOL, Ibrahim R., KADHIM, Kadhim J. and HASHIM, Ahmed. Preparation of (polyvinyl alcohol–polyethylene glycol–polyvinyl pyrrolidinone–titanium oxide nanoparticles) nanocomposites: electrical properties for energy storage and release. *International Journal of Plastics Technology* [online]. 2016. Vol. 20, no. 1, p. 121–127. Available from: http://link.springer.com/10.1007/s12588-016-9144-5
81. ZHU, Hongwei, SHANG, Yesheng, JING, Yunke, LIU, Yang, LIU, Yupu, EL-TONI, Ahmed Mohamed, ZHANG, Fan and ZHAO, Dongyuan. Synthesis of Monodisperse Mesoporous TiO2 Nanospheres from a Simple Double-Surfactant Assembly-Directed Method for Lithium Storage. *ACS Applied Materials and Interfaces*. 2016. Vol. 8, no. 38, p. 25586–25594. DOI 10.1021/acsami.6b06534.
82. SUN, Lin, WANG, Fei, SU, Tingting and DU, Hong Bin. Step-by-step assembly preparation of core-shell Si-mesoporous TiO2 composite nanospheres with enhanced lithium-storage properties. *Dalton Transactions*. 2017. Vol. 46, no. 35, p. 11542–11546. DOI 10.1039/c7dt02132a.
83. XUN, Haitao, ZHANG, Zuobin, YU, Aihua and YI, Jianxin. Remarkably enhanced hydrogen sensing of highly-ordered SnO2-decorated TiO2 nanotubes. *Sensors and Actuators, B: Chemical*. 2018. Vol. 273, no. June, p. 983–990. DOI 10.1016/j.snb.2018.06.120.
84. PANG, Z., YU, J., LI, D., NIE, Q., ZHANG, J. and WEI, Q. Free-standing TiO2–SiO2/PANI composite nanofibers for ammonia sensors. *Journal of Materials Science: Materials in Electronics*. 2018. Vol. 29, no. 5, p. 3576–3583. DOI 10.1007/s10854-017-8287-2. © 2017, Springer Science+Business Media, LLC, part of Springer Nature.
85. VINOTH, S., KANIMOZHI, G., KUMAR, Harish, SRINADHU, E. S. and SATYANARAYANA, N. Symbiotic organism search algorithm for simulation of J-V

characteristics and optimizing internal parameters of DSSC developed using electrospun TiO2nanofibers. *Journal of Nanoparticle Research*. 2017. Vol. 19, no. 12. DOI 10.1007/s11051-017-4071-8. © 2017, Springer Science+Business Media B.V., part of Springer Nature..

86. LI, Jing, LIU, Hongdong, HU, Zhongli, CHEN, Yuan, RUAN, Haibo, ZHANG, Lei and HU, Rong. Facile approach to prepare TiO2 nanofibers via electrospinning as anode materials for lithium ion batteries. *Journal of Materials Science: Materials in Electronics* [online]. 2016. Vol. 27, no. 8, p. 8682–8687. Available from: http://link.springer.com/10.1007/s10854-016-4889-3
87. EDY, Riyanto, ZHAO, Yuting, HUANG, Gaoshan S., SHI, Jianjun J., ZHANG, Jing, SOLOVEV, Alexander A. and MEI, Yongfeng. TiO2 nanosheets synthesized by atomic layer deposition for photocatalysis. *Progress in Natural Science: Materials International* [online]. 2016. Vol. 26, no. 5, p. 493–497. Available from: http://dx.doi.org/10.1016/j.pnsc.2016.08.010
88. LIU, Baoshun, ZHAO, Xiujian, ZHAO, Qingnan, LI, Chunling and HE, Xin. The effect of O2 partial pressure on the structure and photocatalytic property of TiO2 films prepared by sputtering. *Materials Chemistry and Physics*. 2005. Vol. 90, no. 1, p. 207–212. DOI 10.1016/j.matchemphys.2004.10.038.
89. EUFINGER, K., POELMAN, D., POELMAN, H., DE GRYSE, R. and MARIN, G. B. Photocatalytic activity of dc magnetron sputter deposited amorphous TiO2 thin films. *Applied Surface Science*. 2007. Vol. 254, no. 1 SPEC. ISS., p. 148–152. DOI 10.1016/j.apsusc.2007.07.009.
90. WANG, Furong, ZHANG, Guoqiang, ZHAO, Zhao, TAN, Huaqiao, YU, Weixing, ZHANG, Xuming and SUN, Zaicheng. TiO2 nanosheet array thin film for self-cleaning coating. *RSC Advances*. 2015. Vol. 5, no. 13, p. 9861–9864. DOI 10.1039/c4ra13705a..
91. ADACHI, Takahiro, LATTHE, Sanjay S., GOSAVI, Suresh W., ROY, Nitish, SUZUKI, Norihiro, IKARI, Hiroshi, KATO, Kazuki, KATSUMATA, Ken ichi, NAKATA, Kazuya, FURUDATE, Manabu, INOUE, Tomohiro, KONDO, Takeshi, YUASA, Makoto, FUJISHIMA, Akira and TERASHIMA, Chiaki. Photocatalytic, superhydrophilic, self-cleaning TiO2 coating on cheap, light-weight, flexible polycarbonate substrates. *Applied Surface Science* [online]. 2018. Vol. 458, no. March, p. 917–923. Available from: https://doi.org/10.1016/j.apsusc.2018.07.172
92. LI, Yuanyang, XIA, Bibo and JIANG, Bo. Thermal-induced durable superhydrophilicity of TiO2 films with ultra-smooth surfaces. *Journal of Sol-Gel Science and Technology*. 2018. Vol. 87, no. 1, p. 50–58. DOI 10.1007/s10971-018-4684-0.
93. SELLONI, A, VITTADINI, A and GRÄTZEL, M. The adsorption of small molecules on the TiO2 anatase (101) surface by first-principles molecular dynamics. *Surface Science* [online]. 1998. Vol. 402–404, p. 219–222. Available from: http://linkinghub.elsevier.com/retrieve/pii/S0039602897010662
94. HONG, Youliang, LI, Domgmei, ZHENG, Jian and ZOU, Guangtian. Sol–gel growth of titania from electrospun polyacrylonitrile nanofibres. *Nanotechnology*. 2006. Vol. 17, no. 8, p. 1986–1993. DOI 10.1088/0957-4484/17/8/032.
95. MEHRPOUYA, Fahimeh, TAVANAI, Hossein, MORSHED, Mohammad and GHIACI, Mehran. The formation of titanium dioxide crystallite nanoparticles during activation of PAN nanofibers containing titanium isopropoxide. *Journal of Nanoparticle Research*. 2012. Vol. 14, no. 8. DOI 10.1007/s11051-012-1074-3.
96. PANT, Hem Raj, BAJGAI, Madhab Prasad, NAM, Ki Taek, SEO, Yun A., PANDEYA, Dipendra Raj, HONG, Seong Tshool and KIM, Hak Yong. Electrospun nylon-6 spider-net like nanofiber mat containing TiO2 nanoparticles: A multifunctional nanocomposite

textile material. *Journal of Hazardous Materials*. 2011. Vol. 185, no. 1, p. 124–130. DOI 10.1016/j.jhazmat.2010.09.006..

97. CHOI, Kyoung Jin and HONG, Seok Won. Preparation of TiO2 nanofibers immobilized on quartz substrate by electrospinning for photocatalytic degradation of ranitidine. *Research on Chemical Intermediates*. 2012. Vol. 38, no. 6, p. 1161–1169. DOI 10.1007/s11164-011-0455-z.
98. GAO, Dawei, WANG, Qingqing, QIAO, Hui, CAI, Yibing, HUANG, Fenglin and WEI, Qufu. Preparation and Characterization of Porous TiO2 Fibers and Their Photocatalytic Activity. *Journal of Engineered Fibers and Fabrics*. 2012. Vol. 94, no. 7, p. 94–98.
99. DING, Yanhuai, ZHANG, Ping, LONG, Zhilin, JIANG, Yong, XU, Fu and LEI, Jianguang. Fabrication and photocatalytic property of TiO2 nanofibers. *Journal of Sol-Gel Science and Technology*. 2008. Vol. 46, no. 2, p. 176–179. DOI 10.1007/s10971-008-1683-6.
100. ZHANG, Jin Z. Ultrafast Studies of Electron Dynamics in Semiconductor and Metal Colloidal Nanoparticles: Effects of Size and Surface. *Accounts of Chemical Research*. 1997. Vol. 30, no. 10, p. 423–429. DOI 10.1021/ar960178j.
101. SMITH, Andrew and NIE, Shuming. Semiconductor Nanocrystals: Structure, Properties, and Band Gap Engineering. *Accounts of Chemical Research*. 2010. Vol. 43, no. 2, p. 190–200.
102. VARSHNEY, Gaiven, KANEL, Sushil R., KEMPISTY, David M., VARSHNEY, Vikas, AGRAWAL, Abinash, SAHLE-DEMESSIE, Endalkachew, VARMA, Rajender S. and NADAGOUDA, Mallikarjuna N. Nanoscale TiO2 films and their application in remediation of organic pollutants. *Coordination Chemistry Reviews* [online]. 2016. Vol. 306, p. 43–64. Available from: http://dx.doi.org/10.1016/j.ccr.2015.06.011.
103. HOMAEIGOHAR, Shahin and ELBAHRI, Mady. Nanocomposite electrospun nanofiber membranes for environmental remediation. *Materials*. 2014. Vol. 7, no. 2, p. 1017–1045. DOI 10.3390/ma7021017.
104. LU, Xiaofeng, WANG, Ce and WEI, Yen. One-dimensional composite nanomaterials: Synthesis by electrospinning and their applications. *Small*. 2009. Vol. 5, no. 21, p. 2349–2370. DOI 10.1002/smll.200900445.
105. SHAO, Changlu, KIM, Hakyong, GONG, Jian and LEE, Doukrae. A novel method for making silica nanofibres by using electrospun fibres of polyvinylalcohol/silica composite as precursor. *Nanotechnology*. 2002. Vol. 13, p. 635–637.
106. LOCKWOOD, David J., DING, Bin and JIANYONG, Yu. *Electrospun Nanofibers for Energy and Environmental Applications*. 2015. ISBN 9783642541599.
107. MATULEVICIUS, Jonas. *Formation and investigation of filtration properties of the electrospun nanofiber materials*. Kaunas Universityof Technology, 2016.
108. DAHLIN, Rebecca L., KASPER, F. Kurtis and MIKOS, Antonios G. Polymeric Nanofibers in Tissue Engineering. *Tissue Engineering Part B: Reviews* [online]. 2011. Vol. 17, no. 5, p. 349–364. Available from: http://www.liebertonline.com/doi/abs/10.1089/ten.teb.2011.0238
109. YOU, Yang, ZHANG, Shiying, WAN, Long and XU, Difa. Preparation of continuous TiO2 fibers by sol-gel method and its photocatalytic degradation on formaldehyde. *Applied Surface Science* [online]. 2012. Vol. 258, no. 8, p. 3469–3474. Available from: http://dx.doi.org/10.1016/j.apsusc.2011.11.099
110. T. ONDARÇUHU AND C. JOACHIM. Drawing a Single Nanofibre over Hundreds of Microns. *Europhysics Letters*. 1998. Vol. 42, no. 2, p. 215–220. DOI 10.1209/epl/i1998-00233-9.
111. LI, Hua, ZHANG, Tianxi, PAN, Chao, PU, Chenchen, HU, Yang, HU, Xiaoyun, LIU, Enzhou and FAN, Jun. Self-assembled Bi2MoO6/TiO2 nanofiber heterojunction film

with enhanced photocatalytic activities. *Applied Surface Science* [online]. 2017. Vol. 391, p. 303–310. Available from: http://dx.doi.org/10.1016/j.apsusc.2016.06.167.

112. LIU, Yurong, ZHANG, Zongqiang and HU, Rong. Synthesis of three-dimensional hierarchically porous reduced graphene oxide–TiO2 nanocomposite for enhanced hydrogen storage. *Ceramics International* [online]. 2018. Vol. 44, no. 11, p. 12458–12465. Available from: https://doi.org/10.1016/j.ceramint.2018.04.036
113. WANG, Xianfeng, DING, Bin, SUN, Gang, WANG, Moran and YU, Jianyong. Electro-spinning/netting: A strategy for the fabrication of three-dimensional polymer nano-fiber/nets. *Progress in Materials Science* [online]. 2013. Vol. 58, no. 8, p. 1173–1243. Available from: http://dx.doi.org/10.1016/j.pmatsci.2013.05.001
114. LUO, C. J., STOYANOV, Simeon D., STRIDE, E., PELAN, E. and EDIRISINGHE, M. Electrospinning versus fibre production methods: From specifics to technological convergence. *Chemical Society Reviews*. 2012. Vol. 41, no. 13, p. 4708–4735. DOI 10.1039/c2cs35083a.
115. RENEKER, Darrell H. and YARIN, Alexander L. Electrospinning jets and polymer nanofibers. *Polymer* [online]. 2008. Vol. 49, no. 10, p. 2387–2425. Available from: http://dx.doi.org/10.1016/j.polymer.2008.02.002
116. CERNUTO, Giuseppe, MASCIOCCHI, Norberto, CERVELLINO, Antonio, COLONNA, Gian Maria and GUAGLIARDI, Antonietta. Size and Shape Dependence of the Photocatalytic Activity of TiO2 Nanocrystals: A Total Scattering Debye Function Study. *Journal of the American Chemical Society* [online]. 2011. Vol. 133, no. 9, p. 3114–3119. Available from: http://pubs.acs.org/doi/abs/10.1021/ja110225n
117. SHAPOVALOV, V. I. Nanopowders and films of titanium oxide for photocatalysis: A review. *Glass Physics and Chemistry* [online]. 2010. Vol. 36, no. 2, p. 121–157. Available from: http://link.springer.com/10.1134/S108765961002001X
118. LU, Cheng and LIPSON, R. H. Interference lithography: A powerful tool for fabricating periodic structures. *Laser and Photonics Reviews*. 2010. Vol. 4, no. 4, p. 568–580. DOI 10.1002/lpor.200810061.
119. PATIL, Meghshyam, SHAIKH, Sharekh and GANESH, Ibram. Recent Advances on TiO_2 Thin Film Based Photocatalytic Applications (A Review). *Current Nanoscience* [online]. 2015. Vol. 11, no. 3, p. 271–285. DOI 10.2174/1573413711666150212235054. Available from: http://www.eurekaselect.com/openurl/content.php?genre=article&issn=1573-4137&volume=11&issue=3&spage=271
120. CHEN, Zih Yu, HU, Yi, LIU, Tung Cheng, HUANG, Chien Lung and JENG, Tian Syuan. Mesoporous TiO2 thin films embedded with Au nanoparticles for the enhancement of the photocatalytic properties. *Thin Solid Films* [online]. 2009. Vol. 517, no. 17, p. 4998–5000. Available from: http://dx.doi.org/10.1016/j.tsf.2009.03.189
121. YEN, Yin Cheng, CHEN, Jing Zhi, LU, Yu Jung, GWO, Shangjr and LIN, Kuan Jiuh. Chain-network anatase/TiO2 (B) thin film with improved photocatalytic efficiency. *Nanotechnology*. 2014. Vol. 25, no. 23. DOI 10.1088/0957-4484/25/23/235602.
122. GU, De E., YANG, Bang Chao and HU, Yong D. A novel method for preparing V-doped titanium dioxide thin film photocatalysts with high photocatalytic activity under visible light irradiation. *Catalysis Letters*. 2007. Vol. 118, no. 3–4, p. 254–259. DOI 10.1007/s10562-007-9179-5.
123. MURUGAN, Karuppiah, RAO, Tata N., GANDHI, Ashutosh S. and MURTY, B. S. Effect of aggregation of methylene blue dye on TiO2 surface in self-cleaning studies. *Catalysis Communications* [online]. 2010. Vol. 11, no. 6, p. 518–521. Available from: http://dx.doi.org/10.1016/j.catcom.2009.12.007

124. WANG, Xiao-Ping, YU, Yun, HU, Xing-Fang and GAO, Lian. Hydrophilicity of TiO2 films prepared by liquid phase deposition. *Thin Solid Films*. 2000. Vol. 371, no. 1–2, p. 148–152. DOI 10.1016/S0040-6090(00)00995-0.
125. TAVARES, C. J., MARQUES, S. M., VISEU, T., TEIXEIRA, V., CARNEIRO, J. O., ALVES, E., BARRADAS, N. P., MUNNIK, F., GIRARDEAU, T. and RIVÌRE, J. P. Enhancement in the photocatalytic nature of nitrogen-doped PVD-grown titanium dioxide thin films. *Journal of Applied Physics*. 2009. Vol. 106, no. 11. DOI 10.1063/1.3269702.
126. HECK, R. M., FARRAUTO, R. K. and GULATI, S. T. Catalyst Characterization. In : *Catalytic Air Pollution Control: Commercial Technology* [online]. 3rd. John Wiley & Sons, Inc., 2009. p. 41–62. ISBN 978-0-470-27503-0. Available from: http://doi.wiley.com/10.1002/3527602658.
127. SU, Shao, WU, Wenhe, GAO, Jimin, LU, Jianxin and FAN, Chunhai. Nanomaterials-based sensors for applications in environmental monitoring. *Journal of Materials Chemistry*. 2012. Vol. 22, no. 35, p. 18101–18110. DOI 10.1039/c2jm33284a.
128. SAPOUNTZI, Eleni, BRAIEK, Mohamed, CHATEAUX, Jean François, JAFFREZIC-RENAULT, Nicole and LAGARDE, Florence. Recent advances in electrospun nanofiber interfaces for biosensing devices. *Sensors (Switzerland)*. 2017. Vol. 17, no. 8. DOI 10.3390/s17081887.
129. DING, Bin, WANG, Moran, YU, Jianyong and SUN, Gang. Gas sensors based on electrospun nanofibers. *Sensors*. 2009. Vol. 9, no. 3, p. 1609–1624. DOI 10.3390/s90301609.
130. LANDAU, Osnat and ROTHSCHILD, Avner. Fibrous TiO2 gas sensors produced by electrospinning. *Journal of Electroceramics*. 2015. Vol. 35, no. 1–4, p. 148–159. DOI 10.1007/s10832-015-0007-9.
131. PASCALI, Chiara De, SIGNORE, Maria Assunta, TAURINO, Antonietta, FRANCIOSO, Luca, MACAGNANO, Antonella, AVOSSA, Joshua, SICILIANO, Pietro and CAPONE, Simonetta. Investigation of the Gas-Sensing Performance of Electrospun TiO2 Nanofiber-Based Sensors for Ethanol Sensing. *IEEE Sensors Journal*. 2018. Vol. 18, no. 18, p. 7365–7374. DOI 10.1109/JSEN.2018.2857851.
132. DAI, Yunqian, LIU, Wenying, FORMO, Eric, SUN, Yueming and XIA, Younan. Ceramic nanofibers fabricated by electrospinning and their applications in catalysis, environmental science, and energy technology. *Polymers for Advanced Technologies*. 2011. Vol. 22, no. 3, p. 326–338. DOI 10.1002/pat.1839.
133. MATULEVICIUS, Jonas, KLIUCININKAS, Linas, PRASAUSKAS, Tadas, BUIVYDIENE, Dalia and MARTUZEVICIUS, Dainius. The comparative study of aerosol filtration by electrospun polyamide, polyvinyl acetate, polyacrylonitrile and cellulose acetate nanofiber media. *Journal of Aerosol Science* [online]. 2016. Vol. 92, p. 27–37. Available from: http://dx.doi.org/10.1016/j.jaerosci.2015.10.006
134. WANG, Lei, ZHANG, Changbo, GAO, Feng and PAN, Gang. Needleless electrospinning for scaled-up production of ultrafine chitosan hybrid nanofibers used for air filtration. *RSC Advances*. 2016. Vol. 6, no. 107, p. 105988–105995. DOI 10.1039/c6ra24557a.
135. WANG, Zhe, PAN, Zhijuan, WANG, Jigen and ZHAO, Ruizhi. A Novel Hierarchical Structured Poly(lactic acid)/Titania Fibrous Membrane with Excellent Antibacterial Activity and Air Filtration Performance. *Journal of Nanomaterials*. 2016. Vol. 2016. DOI 10.1155/2016/6272983.
136. FAN, Yaofang, CHEN, Shuo, ZHAO, Huimin and LIU, Yanming. Distillation membrane constructed by TiO2 nanofiber followed by fluorination for excellent water desalination performance. *Desalination*. 2017. Vol. 405, p. 51–58. DOI 10.1016/j.desal.2016.11.028.

137. DAI, Yunqian, FORMO, Eric, LI, Haoxuan, XUE, Jiajia and XIA, Younan. Surface-Functionalized Electrospun Titania Nanofibers for the Scavenging and Recycling of Precious Metal Ions. *ChemSusChem*. 2016. Vol. 9, no. 20, p. 2912–2916. DOI 10.1002/cssc.201600787.
138. ALVES, A. K., BERUTTI, F. A., CLEMENS, F. J., GRAULE, T. and BERGMANN, C. P. Photocatalytic activity of titania fibers obtained by electrospinning. *Materials Research Bulletin*. 2009. Vol. 44, no. 2, p. 312–317. DOI 10.1016/j.materresbull.2008.06.001.
139. OCHANDA, Fredrick O, RAJUKADA, Sitarama and BARNETT, Matthew R. Controlled Synthesis of TiO2 Hierarchical Nanofibre Structures via Electrospinning and Solvothermal Processes: Photocatalytic Activity for Degradation of Methylene Blue. *Nanomaterials and Nanotechnology*. 2012. Vol. 2, p. 1–10.
140. KANG, Hyun Jung, SHIN, Seung H, JO, Wan K and CHUN, Ho Hwan. Visible Light- or UV-Activated Carbon Nanotube-TiO2 Composite Nanofibers for Indoor BTEX Purification. *ASIAN JOURNAL OF CHEMISTRY*. 2014. Vol. 26, no. 6, p. 1803–1807. DOI http://dx.doi.org/10.14233/ajchem.2014.17361.
141. KANG, Hyun Jung, SHIN, Seung H, JO, Wan K and CHUN, Ho Hwan. Combined Nanofibers of Carbon Nanotube, Titania and Polymer Substrate for Oxidation of Toluene and Isopropyl Alcohol†. *ASIAN JOURNAL OF CHEMISTRY*. 2014. Vol. 26, no. 6, p. 1607–1610. DOI http://dx.doi.org/10.14233/ajchem.2014.17299.
142. BARGHI, AHMED EL RUBY SHAHZAD, Mohamed and ROHANI, Sohrab. N- and C-Modified TiO2 Nanotube Arrays: Enhanced Photoelectrochemical Properties and Effect of Nanotubes Length on Photoconversion Efficiency. *Nanomaterials*. 2018. Vol. 8, p. 198 (1-16). DOI 10.3390/nano8040198.
143. ZHANG, Yifan, PARK, Mira, KIM, Hak Yong, EL-NEWEHY, Mohamed, RHEE, Kyong Yop and PARK, Soo Jin. Effect of TiO2 on photocatalytic activity of polyvinylpyrrolidone fabricated via electrospinning. *Composites Part B: Engineering*. 2015. Vol. 80, p. 355–360. DOI 10.1016/j.compositesb.2015.05.040.
144. JO, Wan Kuen and KANG, Hyun Jung. Polyacrylonitrile-TiO2 fibers for control of gaseous aromatic compounds. *Industrial and Engineering Chemistry Research*. 2013. Vol. 52, no. 12, p. 4475–4483. DOI 10.1021/ie303178u.
145. IM, Ji Sun, KIM, Min Il and LEE, Young Seak. Preparation of PAN-based electrospun nanofiber webs containing TiO2 for photocatalytic degradation. *Materials Letters*. 2008. Vol. 62, no. 21–22, p. 3652–3655. DOI 10.1016/j.matlet.2008.04.019.
146. COSSICH, E., BERGAMASCO, R., PESSOA DE AMORIM, M. T., MARTINS, P. M., MARQUES, J., TAVARES, C. J., LANCEROS-MÉNDEZ, S. and SENCADAS, V. Development of electrospun photocatalytic TiO2-polyamide-12 nanocomposites. *Materials Chemistry and Physics*. 2015. Vol. 164, p. 91–97. DOI 10.1016/j.matchemphys.2015.08.029.
147. PANT, Hem Raj, PANT, Bishweshwar, POKHAREL, Pashupati, KIM, Han Joo, TIJING, Leonard D., PARK, Chan Hee, LEE, Dai Soo, KIM, Hak Yong and KIM, Cheol Sang. Photocatalytic TiO2-RGO/nylon-6 spider-wave-like nano-nets via electrospinning and hydrothermal treatment. *Journal of Membrane Science*. 2013. Vol. 429, p. 225–234. DOI 10.1016/j.memsci.2012.11.025.
148. PONGSORRARITH, Voraluck, SRISITTHIRATKUL, Chutima, LAOHHASURAYOTIN, Kritapas and INTASANTA, Narupol. Solution- and air-recoverable photocatalytic nanofibers by facile and cost-effective electrospinning and co-precipitation processes. *Materials Letters* [online]. 2012. Vol. 67, no. 1, p. 1–4. Available from: http://dx.doi.org/10.1016/j.matlet.2011.09.018

149. BAIYILA, Dahu, WANG, Xiaohui, LI, Xin, SHARILEAODU, Bao, LI, Xiaotian, XU, Liang, LIU, Zongrui, DUAN, Limei and LIU, Jinghai. Electrospun TiO 2 nanofibers integrating space-separated magnetic nanoparticles and heterostructures for recoverable and efficient photocatalyst. *Journal of Materials Chemistry A* [online]. 2014. Vol. 2, no. 31, p. 12304–12310. Available from: http://xlink.rsc.org/?DOI=C4TA02224F
150. AL-MEER, Saeed, GHOURI, Zafar Khan, ELSAID, Khaled, EASA, Ahmed, AL-QAHTANI, Muneera Th and SHAHEER AKHTAR, M. Engineering of magnetically separable ZnFe2O4@TiO2 nanofibers for dye-sensitized solar cells and removal of pollutant from water. *Journal of Alloys and Compounds* [online]. 2017. Vol. 723, p. 477–483. Available from: http://dx.doi.org/10.1016/j.jallcom.2017.06.211
151. OCHIAI, Tsuyoshi and FUJISHIMA, Akira. Photoelectrochemical properties of TiO2 photocatalyst and its applications for environmental purification. *Journal of Photochemistry and Photobiology C: Photochemistry Reviews*. 2012. Vol. 13, no. 4, p. 247–262. DOI 10.1016/j.jphotochemrev.2012.07.001.
152. BOYJOO, Yash, SUN, Hongqi, LIU, Jian, PAREEK, Vishnu K. and WANG, Shaobin. A review on photocatalysis for air treatment: From catalyst development to reactor design. *Chemical Engineering Journal* [online]. 2017. Vol. 310, p. 537–559. Available from: http://dx.doi.org/10.1016/j.cej.2016.06.090
153. ZHANG, Xiwen, XU, Shiyou and HAN, Gaorong. Fabrication and photocatalytic activity of TiO2 nanofiber membrane. *Materials Letters* [online]. 2009. Vol. 63, no. 21, p. 1761–1763. Available from: http://dx.doi.org/10.1016/j.matlet.2009.05.038
154. SZATMÁRY, Lórant, ŠUBRT, Jan, KALOUSEK, Vít, MOSINGER, Jiří and LANG, Kamil. Low-temperature deposition of anatase on nanofiber materials for photocatalytic NOx removal. *Catalysis Today*. 2014. Vol. 230, p. 74–78. DOI 10.1016/j.cattod.2013.09.023.
155. CHUN, Ho-hwan and JO, Wan-kuen. Polymer material-supported titania nanofibers with different polyvinylpyrrolidone to TiO2 ratios for degradation of vaporous trichloroethylene. *Journal of Industrial and Engineering Chemistry* [online]. 2014. Vol. 20, no. 3, p. 1010–1015. Available from: http://dx.doi.org/10.1016/j.jiec.2013.06.036
156. MOZIA, Sylwia, HECIAK, Aleksandra and MORAWSKI, Antoni W. Preparation of Fe-modified photocatalysts and their application for generation of useful hydrocarbons during photocatalytic decomposition of acetic acid. *Journal of Photochemistry and Photobiology A: Chemistry*. 2010. Vol. 216, no. 2–3, p. 275–282. DOI 10.1016/j.jphotochem.2010.09.016.
157. NIOSH. *Hydrocarbons , Aromatic (NIOSH-1501)* [online]. 2003. Available from: https://www.cdc.gov/niosh/docs/2003-154/pdfs/1501.pdf.
158. MADHUGIRI, Sudha, SUN, Bo, SMIRNIOTIS, Panagiotis G., FERRARIS, John P. and BALKUS, Kenneth J. Electrospun mesoporous titanium dioxide fibers. *Microporous and Mesoporous Materials*. 2004. Vol. 69, no. 1–2, p. 77–83. DOI 10.1016/j.micromeso.2003.12.023.
159. CHATTOPADHYAY, Shreyasi, SAHA, Jony and DE, Goutam. Electrospun anatase TiO2 nanofibers with ordered mesoporosity. *J. Mater. Chem. A*. 2014. Vol. 2, no. 44, p. 19029–19035. DOI 10.1039/C4TA04481A.
160. GU, Liuan, WANG, Jingyu, QI, Rong, WANG, Xiaoyu, XU, Ping and HAN, Xijiang. A novel incorporating style of polyaniline/TiO2 composites as effective visible photocatalysts. *Journal of Molecular Catalysis A: Chemical* [online]. 2012. Vol. 357, p. 19–25. Available from: http://dx.doi.org/10.1016/j.molcata.2012.01.012
161. LACHHEB, Hinda, PUZENAT, Eric, HOUAS, Ammar, KSIBI, Mohamed, ELALOUI, Elimame, GUILLARD, Chantal and HERRMANN, Jean Marie. Photocatalytic

degradation of various types of dyes (Alizarin S, Crocein Orange G, Methyl Red, Congo Red, Methylene Blue) in water by UV-irradiated titania. *Applied Catalysis B: Environmental*. 2002. Vol. 39, no. 1, p. 75–90. DOI 10.1016/S0926-3373(02)00078-4.

162. MANO, Takayuki, NISHIMOTO, Shunsuke, KAMESHIMA, Yoshikazu and MIYAKE, Michihiro. Water treatment efficacy of various metal oxide semiconductors for photocatalytic ozonation under UV and visible light irradiation. *Chemical Engineering Journal*. 2015. Vol. 264, p. 221–229. DOI 10.1016/j.cej.2014.11.088.
163. WANG, Xueqin, SØ, Lasse, SU, Ren, WENDT, Stefan, HALD, Peter, MAMAKHEL, Aref, YANG, Chuanxu, HUANG, Yudong, IVERSEN, Bo B. and BESENBACHER, Flemming. The influence of crystallite size and crystallinity of anatase nanoparticles on the photo-degradation of phenol. *Journal of Catalysis*. 2014. Vol. 310, p. 100–108. DOI 10.1016/j.jcat.2013.04.022.
164. LIN, Jiaojiao, LUO, Zhanzhou, LIU, Jiaojiao and LI, Ping. Photocatalytic degradation of methylene blue in aqueous solution by using ZnO-SnO2 nanocomposites. *Materials Science in Semiconductor Processing* [online]. 2018. Vol. 87, no. 20, p. 24–31. Available from: https://doi.org/10.1016/j.mssp.2018.07.003
165. ALSALKA, Yamen, HAKKI, Amer, FLEISCH, Manuel and BAHNEMANN, Detlef W. Understanding the degradation pathways of oxalic acid in different photocatalytic systems: Towards simultaneous photocatalytic hydrogen evolution. *Journal of Photochemistry and Photobiology A: Chemistry* [online]. 2018. Vol. 366, p. 81–90. Available from: https://doi.org/10.1016/j.jphotochem.2018.04.008
166. LEE, Joon Y, SHIN, Seung H, CHUN, Ho H and JO, Wan K. Control of Airborne Aromatic Hydrocarbons over TiO2-Carbon Nanotube Composites. *International Journal of Chemical, Molecular, Nuclear, Materials and Metallurgical Engineering.* 2015. Vol. 9, no. 2, p. 347–352.
167. CHUN, Ho Hwan, LEE, Joon Yeob and JO, Wan Kuen. Photocatalysis of low-concentration gaseous organic pollutants over electrospun iron-doped titanium dioxide nanofibers. *Solid State Sciences* [online]. 2013. Vol. 25, p. 103–109. Available from: http://dx.doi.org/10.1016/j.solidstatesciences.2013.08.012.
168. OHTANI, Bunsho, OGAWA, Yoshimasa and NISHIMOTO, Sei-ichi. Photocatalytic Activity of Amorphous−Anatase Mixture of Titanium(IV) Oxide Particles Suspended in Aqueous Solutions. *The Journal of Physical Chemistry B* [online]. 1997. Vol. 101, no. 19, p. 3746–3752. DOI 10.1021/jp962702+. Available from: http://pubs.acs.org/doi/abs/10.1021/jp962702%2Bs.
169. ZOU, Tao, XIE, Changsheng, LIU, Yuan, ZHANG, Shasha, ZOU, Zhijun and ZHANG, Shunping. Full mineralization of toluene by photocatalytic degradation with porous TiO2/SiC nanocomposite film. *Journal of Alloys and Compounds* [online]. 2013. Vol. 552, p. 504–510. DOI 10.1016/j.jallcom.2012.11.061. Available from: http://dx.doi.org/10.1016/j.jallcom.2012.11.061
170. WEI, Zaishan, SUN, Jianliang, XIE, Zhirong, LIANG, Mingyan and CHEN, Shangzhi. Removal of gaseous toluene by the combination of photocatalytic oxidation under complex light irradiation of UV and visible light and biological process. *Journal of Hazardous Materials* [online]. 2010. Vol. 177, no. 1–3, p. 814–821. Available from: http://dx.doi.org/10.1016/j.jhazmat.2009.12.106
171. DEBONO, O., HEQUET, V., LE COQ, L., LOCOGE, N. and THEVENET, F. VOC ternary mixture effect on ppb level photocatalytic oxidation: Removal kinetic, reaction intermediates and mineralization. *Applied Catalysis B: Environmental* [online]. 2017. Vol. 218, no. September, p. 359–369. Available from: http://dx.doi.org/10.1016/j.apcatb.2017.06.070T

172. CHA, Gihoon, LEE, Kiyoung, YOO, Jeong Eun, KILLIAN, Manuela S. and SCHMUKI, Patrik. Topographical study of TiO2 nanostructure surface for photocatalytic hydrogen production. *Electrochimica Acta* [online]. 2015. Vol. 179, p. 423–430. Available from: http://dx.doi.org/10.1016/j.electacta.2015.02.127

173. LEI, Ping, WANG, Feng, GAO, Xiaowei, DING, Yanfen, ZHANG, Shimin, ZHAO, Jincai, LIU, Shaoren and YANG, Mingshu. Immobilization of TiO2 nanoparticles in polymeric substrates by chemical bonding for multi-cycle photodegradation of organic pollutants. *Journal of Hazardous Materials* [online]. 2012. Vol. 227–228, p. 185–194. Available from: http://dx.doi.org/10.1016/j.jhazmat.2012.05.029

174. DEB, Hridam, XIAO, Shili, MORSHED, Mohammad Neaz and AL AZAD, Shamim. Immobilization of Cationic Titanium Dioxide (TiO2+) on Electrospun Nanofibrous Mat: Synthesis, Characterization, and Potential Environmental Application. *Fibers and Polymers* [online]. 2018. Vol. 19, no. 8, p. 1715–1725. Available from: http://link.springer.com/10.1007/s12221-018-8158-3

175. SINGH, S., SINGH, P. K. and MAHALINGAM, Hari. A novel and effective strewn polymer-supported titanium dioxide photocatalyst for environmental remediation. *Journal of Materials and Environmental Science*. 2015. Vol. 6, no. 2, p. 349–358.

176. PORTELA, R., TESSINARI, R. F., SUÁREZ, S., RASMUSSEN, S. B., HERNÁNDEZ-ALONSO, M. D., CANELA, M. C., ÁVILA, P. and SÁNCHEZ, B. Photocatalysis for continuous air purification in wastewater treatment plants: From lab to reality. *Environmental Science and Technology*. 2012. Vol. 46, no. 9, p. 5040–5048. DOI 10.1021/es2042355.

177. BLOMMAERTS, Natan, ASAPU, Ramesh, CLAES, Nathalie, BALS, Sara, LENAERTS, Silvia and VERBRUGGEN, Sammy W. Gas phase photocatalytic spiral reactor for fast and efficient pollutant degradation. *Chemical Engineering Journal* [online]. 2017. Vol. 316, p. 850–856. Available from: http://dx.doi.org/10.1016/j.cej.2017.02.038

178. National Oceanic and Atmospheric Administration, Earth System Research Laboratory, Global Monitoring Division. Trends in Atmospheric Carbon Dioxide [online]. [Accesses 12 2018, September]. Available from https://www.esrl.noaa.gov/gmd/ccgg/trends/global.html

APPENDICES

A. 1. Characterization techniques for determination of the most important properties for environmental photocatalysts

XRD	Structural analysis provides information on a crystal structure, phase, average grain size, crystallinity, strain, and crystal defects; therefore, XRD can be used for both qualitative and quantitative analyses. XRD peaks are produced by constructive interference of a monochromatic beam of X-rays diffracted at specific angles from each set of lattice planes in a sample. Crystal structures are basically repetitive arrangements of atoms that form planes. In the periodic crystal structure with a space d between diffracting planes, the scattered radiation will interfere in directions where the difference in path length $2\cdot d\cdot sin(\theta)$ is equal to an integer n times the wavelength of the beam (λ). These specific directions appear as spots at an angle of 2θ on the diffraction pattern called reflections. This relation is determined by Bragg's law: $2\cdot d\cdot sin(\theta) = n\cdot\lambda$.
Imaging and spectroscopy	Techniques that make the usage of electron beams to image nano-scale features of the sample that cannot be imaged using the conventional optical microscopy due to diffraction limits of the visible-light wavelength. Compared with conventional optical microscopes, electron microscopes use an electron gun to produce electrons instead of a light source. The basic components include an electron gun to produce electrons, electromagnetic lenses that are used to focus electrons, and the detector. The generated beam of electrons is accelerated by voltage, focused and scanned through the sample. The way the electrons interact with the sample determines information that can be obtained from it. Electrons that will be scattered around the sample and will make the way back out will become back-scattered electrons, based on the information obtained from these electrons scanning electron microscopy images are produced. Some of initiated electrons will strike an electron that is already present in the sample and displace them this way forming secondary electrons. During this process, the X-rays are produced as a side effect of the relaxation process. This energy can be measured and used in a technique called Energy dispersive spectroscopy. EDS provides information on the elemental and chemical composition of all elements with an atomic number greater than boron. Analyzing these rays, it is possible to identify the element that came from it. If the sample is small enough, some electrons will be able to pass through the sample and will maintain the same direction as well as energy as in the incident electron beam. These electrons are used in TEM.
Nitrogen gas physisorption	This method is most commonly used to determine a surface area, pore size, and volume of the material of interest. This is usually carried out at a temperatures close to the boiling point of the N_2 gas (77 K). The N_2 molecules are attached to the surface of the material through Van-der-Waals interactions. Each adsorbed molecule occupies an area of the surface, therefore by measuring the number of N_2 molecules adsorbed at monolayer coverage, the internal surface area can be calculated. For that, Brunauer-Emmett-Teller (BET) is often used: $\frac{1}{V\cdot(\frac{P}{P_0}-1)} = \frac{C-1}{V_m\cdot C}\cdot\frac{P}{P_0}+\frac{1}{V_m\cdot C}$, where: P is partial pressure of N_2, P_0 is saturation pressure at the experimental temperature, V is volume adsorbed at P, V_m is volume adsorbed at monolayer coverage, and C is a constant. Physisorption data are often presented as adsorption/desorption isotherm, which shows the amount of gas adsorbed over the pressure interval at constant temperature. The shape of it

	depends on both the adsorbate and adsorbent. According to IUPAC, there are six types of adsorption/desorption isotherms. Examining the N_2 physisorbtion it is often possible to see the difference between adsorption and desorption curves. This gab is called a hysteresis loop which indicates that there is mesopores in the material. There are six characteristic types of hysteresis loops that are closely related to particular features of the pores structure and adsorption mechanism.
TGA	It is a technique in which the mass of a substance is monitored as a function of temperature or time as the sample specimen is subjected to a controlled temperature program in a controlled atmosphere, which allows the quantitative composition analysis. In TGA, mass loss is observed if a thermal event involves loss of a volatile component other loosely bound molecules. Chemical reactions, such as combustion or evaporation, involve mass losses, whereas physical changes, such as melting, do not. TGA consists of a sample pan that is supported by a precision balance.
FTIR spectroscopy	It is used to perform qualitative and quantitative analysis of organic compounds and to determine the chemical structure of many compounds because chemical bonds absorb IR energy at specific wavelength. The basic structure of compounds can be determined by the spectral locations of their IR absorptions. The plot of a compound's IR transmission versus wavelength is its "fingerprint," which when compared to reference spectra identifies the material.
Interferometry	It is an investigative optical technique that uses the phenomenon of interference of waves. The basis of this measurement method involves splitting a beam of light into two equal parts using a beam-splitter. The reference beam reflects from the first mirror and reaches the detector, while the second beam goes through the sample on the second mirror and from there back through the beam splitter to the same detector. The latest beam gets out of the phase by traveling extra distance compared to the reference one, and this phase difference creates a pattern of light and dark areas, a set of interference fringes, when those two beams overlap and interfere on the detector. The exact pattern depends on the different way that the second beams has to travel. White light is used rather than monochromatic light, because it has a shorter coherence length that will give greater accuracy.
AFM	It provides information by feeling the surface of the material with a sharp tip. When the tip is brought into the surface of the sample, forces between the tip and the sample lead to deflection of the cantilever according to the Hooke's law. In the contact mode the force between the tip and the surface is kept constant during the scanning by manipulating a constant deflection to measure the contours of the surface.

A. 2. UV-C lamp photometric data provided by the manufacturer (Koninklijke Philips N.V., Netherlands)

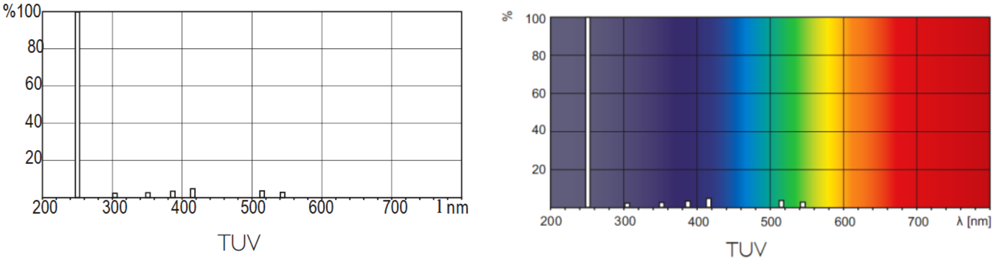

more details available at http://www.lighting.philips.com/main/prof/conventional-lamps-and-tubes/special-lamps/purificationwater-and-air/commercial-and-professional-air/tuv-pl-l/927903004007_EU/product

A. 3. FTIR spectra of the TiO_2 nanofibres synthesized with PAN and TTIP ((a) before and (b) after calcination), and PVP and TiBu ((c) before and (d) after calcination) and Aeroxide P25 (e))

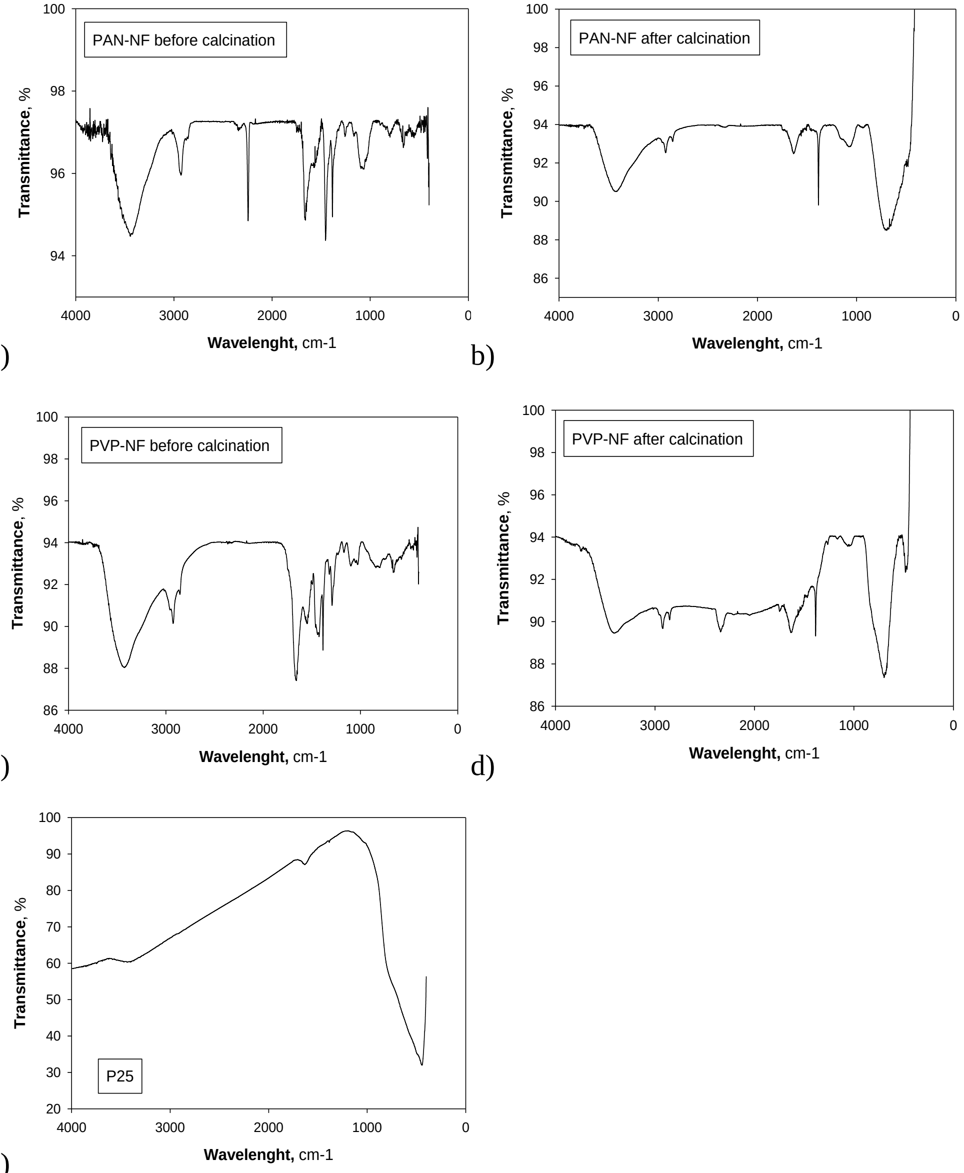

a) b) c) d) e)

A. 4. UV light transmittance spectra of the polyamide (PA12) microfibrous layer

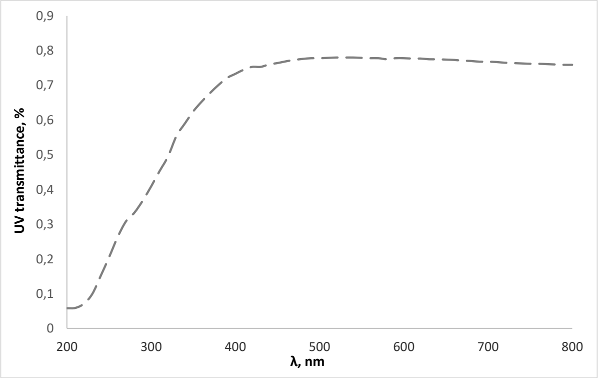

A. 5. Pictures of formed periodic structures made with the optical microscope OPTIKA B 600 MET (using 100x object glass); (a) line patterned 3.3 µm period; (b) grid patterned 3.6 µm period structures; (c) line patterned 5.3 µm period; (d) grid patterned 5.9 µm period structures

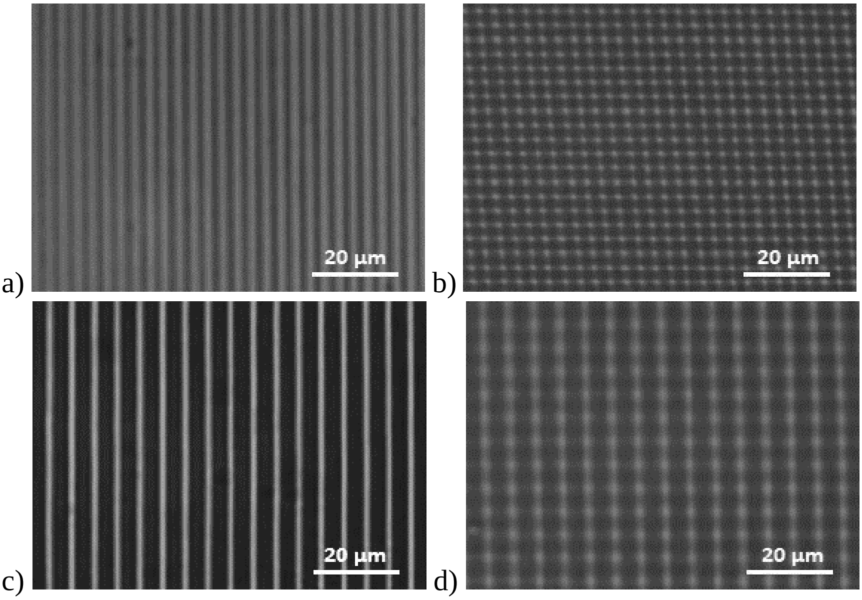

A. 6. SEM of PA12+NF with different NF-TiO_2 densities, 0.04 mg/cm^2 top (a and b) and 0.08 mg/cm^2 bottom (c and d). SEM of the layer with density of 0.06 mg/cm^2 are given in Fig. 11 (e), (g)

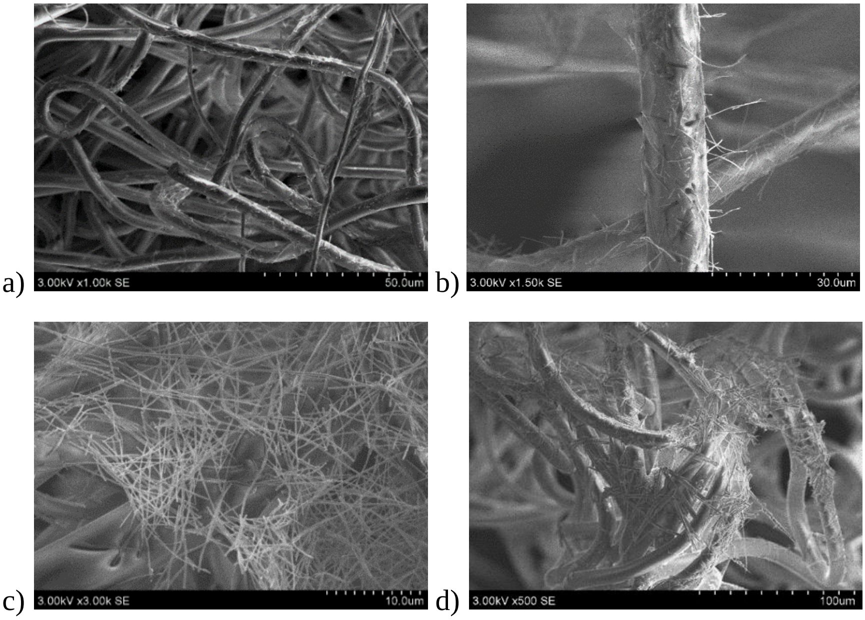

A 7. LIST OF SCIENTIFIC PUBLICATIONS

Publications at the list of *Web of Science* journals

1. Sidaraviciute, Ruta; Buivydiene, Dalia; Krugly, Edvinas; Valatka, Eugenijus; Martuzevicius, Dainius. A composite microfibre-supported short-nanofibre photocatalyst for environmental pollutant decomposition // Journal of photochemistry and photobiology A: Chemistry. Amsterdam: Elsevier. ISSN 1010-6030. 2019, vol. 368, p. 7-14. DOI: 10.1016/j.jphotochem.2018.09.017. [IF: 2,891; AIF: 5,401 (2017);
2. Sidaravičiūtė, Rūta; Krugly, Edvinas; Dabašinskaitė, Lauryna; Valatka, Eugenijus; Martuzevičius, Dainius. Surface-deposited nanofibrous TiO_2 for photocatalytic degradation of organic pollutants // Journal of sol-gel science and technology. New York, NY: Springer Science+Business Media. ISSN 0928-0707. eISSN 1573-4846. 2017, Vol. 84, iss. 2, p. 306-315. DOI: 10.1007/s10971-017-4505-x. [IF: 1,745; AIF: 2,301; (2017)].

Conference Material

Poster presentations

1. Sidaravičiūtė, Rūta; Krugly, Edvinas; Martuzevičius, Dainius. PAN nanofibres as a matrix for catalyst synthesis // Baltic polymer symposium 2016: Klaipeda, September 21-24, 2016: programme and abstracts / Kaunas University of Technology, Vilnius University, Klaipeda University. Kaunas: Kaunas University of Technology, 2016. ISBN 9786090212356. p. 60.
2. Sidaravičiūtė, Rūta; Krugly, Edvinas; Martuzevičius, Dainius. PAN/TiO_2 catalyst formation by electrospinning and its structural characterization // Chemistry and chemical technology: international conference of Lithuanian Society of Chemistry: Lithuanian Academy of Science, Vilnius, Lithuania, April 28-29, 2016: book of abstracts / Fizinių ir technologijos mokslų centras, Vilniaus universitetas, Lietuvos mokslų akademija, Kauno technologijos universitetas. [S.l.]: [s.n.], 2016. ISBN 9786099551135. p. 145.
3. Sidaravičiūtė, Rūta; Krugly, Edvinas; Martuzevičius, Dainius. Fabrication of TiO_2 nanocatalyst for air purification // Electrospin2016: Otranto, Italy, June 28-July 1, 2016
4. Sidaraviciute, Ruta; Darius Ciuzas, Krugly, Edvinas; Martuzevicius, Dainius. TiO2 nanofibers for environmental photocatalytic degradation of organic compounds // 10th World Congress of Chemical Engineering 2017: Barcelona, Spain, October 1-5, 2017

Oral presentations

1. Sidaravičiūtė, Rūta; Krugly, Edvinas; Martuzevičius, Dainius. Modification of TiO_2 nanofibers for environmental photocatalytic applications // Chemistry and chemical technology 2017: proceedings of the international conference, April 28th, 2017, Kaunas. Kaunas: Kauno technologijos universitetas. ISSN 2538-7359. 2017, p. 101.

OTHER PUBLICATIONS

1. Sidaravičiūtė, Rūta; Krugly, Edvinas; Martuzevičius, Dainius. Oro tarša ir sveikata mokyklose // Vaikų sveikatą stiprinanti aplinka. Kurkime ją drauge: respublikinė mokslinė praktinė konferencija, Vilnius, 2016 m. kovo 31 d.: straipsnių rinkinys. Vilnius: Vilniaus universiteto leidykla, 2016. ISBN 9786094596735. p. 25-30.

2. Skorupskaitė, Simona; Sidaravičiūtė, Rūta; Martuzevičius, Dainius; Ruzgas, Tomas. Data analysis models of indoor pollution // International journal of science, environment and technology. Barpeta: MC College. ISSN 2277-663X. eISSN 2278-3687. 2015, Vol. 4, No. 2, p. 318-325.

3. Prasauskas, Tadas; Martuzevičius, Dainius; Sidaravičiūtė, Rūta; Krugly, Edvinas; Du, Liuliu; Haverinen-Shaughnessy, Ulla. Effects of energy retrofits on indoor gaseous pollutant concentrations in Kaunas, Lithuania // Indoor Air 2016: the 14th international conference on indoor air quality and climate, 3-8 July 2016, Ghent, Belgium. Ghent: ISIAQ. 2016, p. 1-6.

4. Prasauskas, Tadas; Krugly, Edvinas; Čiužas, Darius; Sidaravičiūtė, Rūta; Kliučininkas, Linas; Martuzevičius, Dainius. Characterization of mineral fibre emissions from processes of building refurbishment and operation // WSB 2014: World Sustainable Building Conference, Management of Indoor Air Quality by In-Room Air Cleaners and Ventilation, 28-30 October 2014, Barcelona, Spain. Barcelona: Green Building Council Espana, 2014. ISBN 9788469718155. p. [1-8].

SL344. 2019-06-17, 15,5 leidyb. apsk. l., tiražas 14, užsakymas 134.
Išleido Kauno technologijos universitetas, K. Donelaičio g. 73, 44249 Kaunas
Spausdino leidyklos „Technologija“ spaustuvė, Studentų g. 54, 51424 Kaunas